Low-energy electron beams through ultra-thin foils, applications for electron microscopy

Proefschrift

ter verkrijging van de graad van doctor
aan de Technische Universiteit Delft,
op gezag van de Rector Magnificus prof. dr. ir. J. T. Fokkema,
voorzitter van het College voor Promoties,
in het openbaar te verdedigen op dinsdag 22 februari 2005 om 10:30 uur

door

Rogier Herman VAN AKEN

natuurkundig ingenieur
geboren te Amsterdam.

Dit proefschrift is goedgekeurd door de promotor:

Prof. dr. ir. P. Kruit

Samenstelling Promotiecommissie:

Rector Magnificus	voorzitter
Prof. dr. ir. P. Kruit	Technische Universiteit Delft, promotor
Prof. dr. M. Lenc	Masaryk University, Brno, Tsjechië
Prof. dr. ir. J. J. M. Braat	Technische Universiteit Delft
Prof. dr. G. J. Kearley	Technische Universiteit Delft
Prof. dr. ir. P. M. van den Berg	Technische Universiteit Delft
Dr. ir. D. J. Maas	Philips Research Eindhoven
Dr. C. W. Hagen	Technische Universiteit Delft

Het onderzoek beschreven in dit proefschrift is financieel ondersteund door de Stichting voor Fundamenteel Onderzoek der Materie (FOM).

Contents

Chapter 1

Introduction

1.1 Developments in electron microscopy

When Ruska and Knoll invented the electron microscope in the early 1930's [30, 51], the driving force was to develop a microscope that could surpass the resolution limit of the conventional light microscope. Due to the wavelength of visible light, the resolution of the light microscope is limited to around 0.1 μm. Already in the very early days of electron microscopy, Ruska recognised that a resolution of about 0.2 nm would theoretically be possible, owing to the much shorter wavelength of electrons. Since Ruska's prediction, it took about forty years of development before this resolution was practically obtained in a Transmission Electron Microscope (TEM). Modern high resolution TEMs can reach a resolution of 0.1 nm. 0.1 nm is comparable to the distance between neighbouring atoms in a crystal, hence this may be called atomic resolution. The best obtained resolution with Scanning Electron Microscopy (SEM) is nowadays around 1 nm.

Improving the resolution was and still is a very important development in the field of electron microscopy. However, the resolution of a microscope must be viewed in the context of its applicability. For example atomic resolution in a TEM can only be obtained on thin crystalline samples. In a high resolution transmission image of such a sample, the columns of atoms that are arranged according to the crystal lattice may be discriminated. Alternatively, the SEM is able to image the surface of almost any sample. However for a very high resolution, the sample must be put close to the objective lens to facilitate a large demagnification of the spot that is made on the sample without introducing spherical aberration and a high acceleration voltage is preferred to reduce the effects of chromatic aberration and diffraction. Naturally, these constraints set restrictions to the types of samples that can be examined. Hence enhancing the applicability of the electron microscope to a wider range of samples is an important development as well. As progress is made, it is possible to relax the above noted constraints and still have a high resolution. For example it is now possible to obtain a sub 10 nm resolution in a SEM with an acceleration voltage of only 1 kV. The advantage of lower energy electrons is that they cause less damage to the sample and cause less charging of poorly conducting samples. This is of great importance for imaging samples from the semiconductor industry and for biological samples as well. Since feature sizes in the semiconductor industry are continuously decreasing, analytical tools with a resolution below 10 nm will be required. The resolution of low-voltage SEM is mainly limited by the spherical and chromatic aberration of the objective lens. Hence aberration correctors are developed that cancel the spherical and chromatic aberration.

A very attractive feature of electron microscopy is that by the add-on of techniques like Energy Dispersive X-ray analysis (EDX), Auger electron spectroscopy or Electron Energy Loss Spectroscopy (EELS), also the chemical composition of the sample can be determined. These techniques will be explained briefly.

When the sample atoms are hit by the electron beam, they may be brought into an excited state, meaning that a core electron goes to a high energy state. When the inner shell state is filled again by an electron from a high energy state, the released energy can be used to emit either an X-ray or an electron. The latter is called an Auger electron. Both EDX and Auger electron spectroscopy make use of the fact that the energy spectrum of these emissions yields element specific information. Because the incoming electrons may scatter and spread out through the sample before exciting an X-ray and because these X-rays can travel a large distance through the sample, the spatial resolution of EDX is not very high. Auger electrons have an energy ranging from a few tens of eV up to 2 keV. Electrons with such energies can travel a distance of typically only 1 nm before being adsorbed. For this reason Auger electron spectroscopy is a very surface sensitive technique. However, the collection of Auger electrons is not easy because they are emitted in all directions and because the design of an Auger electron detector is limited by the requirement that it should not disturb the optics of the microscope. Therefore, the signal level is low. As a consequence, Auger electron spectroscopy with a high spatial resolution is difficult because a small probe size involves a small probe current and thus a lower Auger signal as well.

EELS can only be used in (Scanning) Transmission Electron Microscopy (STEM). In this technique, the energy of the electrons that have transmitted through the sample is analysed. Part of the electrons have lost some of their energy. This energy loss reveals information about the chemical composition of the sample. The energy loss is typically 0 to 3 keV. For a 100 keV beam, such a loss is so small that these electrons will still go straight through the sample and can easily be collected. Therefore EELS in STEM is a suitable technique to obtain a local analysis of the chemical composition. Modern analysers allow an accurate measurement of the energy spectrum. However, the measured spectrum is a convolution of the energy spread of the beam with the energy loss in the sample. Hence the accuracy of this analysis is limited by the energy spread of the electron beam.

Combining the chemical analysis with a high spatial resolution is an important development as well nowadays. In principle it is possible to do so with Auger electron spectroscopy. However the resolution is still limited to about 10 nm because the current in the probe and as a consequence the Auger signal become too low for smaller probes. For a small probe with a high current, the microscope must be equipped with a high brightness electron source. The Auger electron detector collects the electrons between the objective lens and the sample. The collection efficiency could be improved by increasing the distance between the objective lens and the sample. The downside is that this will also increase the aberrations of the objective lens. This effect can be cancelled by use of an aberration corrector. A reduction of the aberrations can help as well to get a larger current in the probe.

Nowadays, the highest spatial resolution in analytical microscopy can be obtained with EELS in STEM. The main challenge for this technique is to obtain a high energy resolution as well. A good example of what already can be achieved with high resolution EELS was published by Muller in Nature [44]. A sample consisting of a very thin SiO_2 layer sandwiched between crystalline silicon and amorphous silicon was studied with EELS in a Scanning Transmission Electron Microscope. The spatial resolution was 0.26 nm and the energy resolution 1 eV. The high spatial resolution allowed an atomic scale analysis of the sample. The 1 eV energy resolution allowed to detect the presence or absence of the oxygen K edge, which indicates whether the material is an oxide or not. In the transition layer between silicon and silicon-oxide, there is a weak presence of the oxygen K-edge. It would be interesting to analyse the electronic structure in full detail in order to get a more accurate notion of the electrical properties. This is of importance to the IC industry because it tells how thin an oxide layer may be, while still preserving its insulating properties. For such an analysis, an energy resolution of the order of 0.1 eV is required.

A higher energy resolution can be obtained with the aid of a monochromator; an energy filter that only transmits electrons within a specified energy band. Most energy filters are based on the Wien filter design: an electrostatic deflector in combination with a magnetic field which deflects the electrons in the opposite direction. In an electrostatic field, the slower electrons get a larger deflection, where in a magnetic field the deflection is independent of the electron energy. This effect causes an energy dispersion of the beam. With a narrow slit placed after the combined electrostatic and magnetic field, only electrons within a small energy band are passed. A recent example of EELS measurements in a 200 kV TEM with such an energy filter is presented by Lazar et alii [32]. With this system, a 0.1 eV energy resolution with a 2 nm probe or 0.5 eV with a 0.2 nm probe are possible. As a demonstration, the authors have studied a polycrystalline GaN film, containing crystallites in the cubic and in the hexagonal crystal structure. GaN is a wide bandgap semiconductor that can be used for blue LEDs or lasers. For these applications, a defect-free layer in the hexagonal crystal structure is preferred. Figure 1.1 shows the energy loss spectra in the bandgap region for the cubic and the hexagonal structure. The bandgap can be estimated from the steep loss increase between 3 and 4 eV. The difference between the hexagonal and the cubic structure can clearly be seen. The graphs in figure 1.1 are the result of the addition of ten different spectra. Every spectrum was measured with an energy resolution of 0.25 eV.

1.2 Scope of this thesis

In this thesis, two technologies are proposed that can improve the resolution and the analytical capabilities of electron microscopy: the tunnel junction emitter and the low-energy foil corrector. The tunnel junction emitter is a novel high-brightness electron emitter that contains an intrinsic energy filter. With this emitter, a small

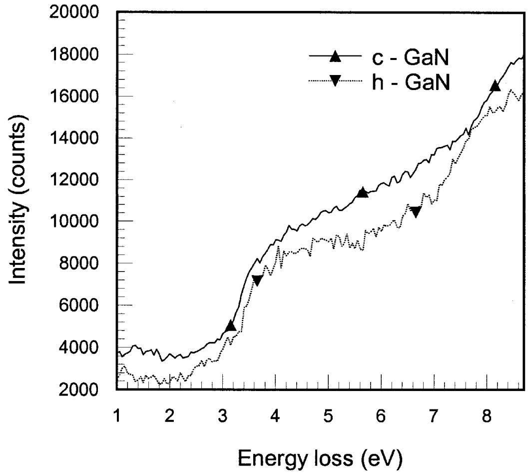

Figure 1.1: *Energy loss spectra in the bandgap region of cubic and hexagonal GaN, measured by Lazar et alii [32].*

energy spread can be obtained without the need to equip the microscope with a monochromator. The low-energy foil corrector is an aberration corrector that is simple in design and in operation and that can correct the spherical and the chromatic aberration simultaneously. Furthermore it may be used as an energy filter as well. Both applications have in common that they make use of an ultra-thin foil and that the electron beam is sent through the thin foil at low energy.

Below, an overview is given of the chapters and their relation with the articles published for this project (see section 1.3).

Chapter 2 discusses the theory of the transmission of low energy electrons through thin foils.

Chapter 3 discusses a fabrication process for ultra-thin free-standing foils. The contents correspond to article 2.

Chapter 4 discusses the concept of the tunnel junction emitter. This is an extension of article 1.

Chapter 5 discusses a pilot experiment to demonstrate the principle of operation of the tunnel junction emitter and a simple fabrication process for tunnel junction emitters as well as experimental results of emitters produced with this method. The second part, section 5.2, corresponds to article 3.

Chapter 6 discusses the concept of the low-energy foil corrector. The contents correspond to article 4.

In Chapter 7 aberration integrals are derived that are required for designing a microscope system with the low-voltage foil corrector. The contents correspond to article 5.

Chapter 8 discusses a system design for a low-voltage SEM equipped with the low-voltage foil corrector. The contents correspond to article 6.

1.3 Project publications

Articles

1. *Calculation of the electron-optical characteristics of electron beams transmitted into vacuum from a sharp tip-thin foil junction*; G.P.E.M. van Bakel, E.G. Borgonjen, C.W. Hagen, and P. Kruit; Journal of Applied Physics 83 (1998) 4279.
2. *Fabrication of Ultra-thin Free-standing Chromium Foils Supported by a Si_3N_4 Membrane-structure with Search Pattern*; I.S. Stepanov, R.H. van Aken, M.R. Zuiddam and C.W. Hagen; Microelectronic Engineering 46 (1999) 435.
3. *A simple fabrication method for tunnel junction emitters*; R.H. van Aken, M.A.P.M. Janssen, C.W. Hagen and P. Kruit; Solid State Electronics 45 (2001) 1033.
4. *Low-energy foil aberration corrector*; R.H. van Aken, C.W. Hagen, J.E. Barth and P. Kruit; Ultramicroscopy 93 (2002) 321.
5. *Aberration integrals for the low-voltage foil corrector*; R.H. van Aken, M.Lenc and J.E.Barth; Nuclear Instruments and Methods in Physics Research A 519 (2004) 205 and 527 (2004) 660.
6. Subject: *Design of a low-voltage SEM equipped with the low-energy foil corrector*; R.H. van Aken, C.W. Hagen, J.E. Barth and P. Kruit; Submitted to Ultramicroscopy.

Patent

Device with foil corrector for electron optical aberrations at low energy; inventors P. Kruit and R.H. van Aken; Delft University of Technology and Stichting Fundamenteel Onderzoek der Materie; International Publication No. WO2004/021391 A1; Publication date 11-3-2004; International Application No. PCT/NL2003/000612.

Chapter 2

Theory of low energy electron transmission

2.1 Introduction

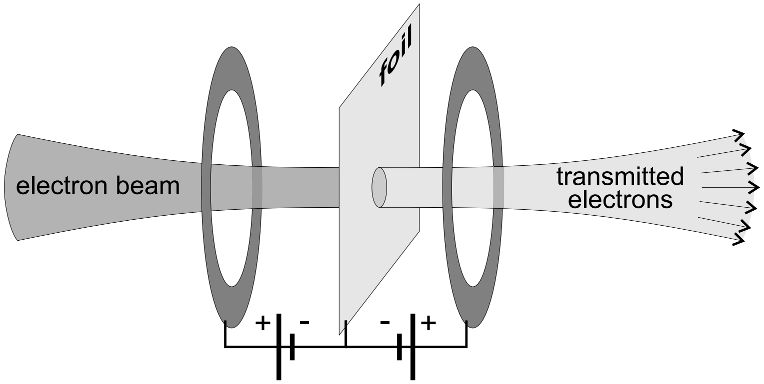

Figure 2.1: *Transmission of a free electron beam through a thin foil on a retarding potential.*

The continuous thread through this thesis is the transmission of low energy electrons through thin foils. This chapter will deal with the theory of the various phenomena involved. Figure 2.1 shows a sketch of the situation that is considered: a free electron beam impinging on and travelling through a thin foil at low energy. The beams kinetic energy in the vacuum is reduced to less than a few eV, approaching 0 eV, which implies that the electrons must be retarded towards the foil and accelerated after transmission through the foil. The transport of electrons through the foil into the vacuum comprises three important physical effects which will be discussed in this chapter:

- reflection at the foil of electrons with insufficient forward energy
- scattering of electrons in the foil
- quantum mechanical reflection of electrons at both foil - vacuum interfaces and the subsequent formation of a standing wave in the foil.

Also a specific case in which the electron beam originates from a tip that is within tunnelling distance from the foil is considered in this thesis, this will be treated in detail in chapter 4.

2.2 High pass energy filtering

Figure 2.2 shows the energy scheme for electrons impinging on the foil. The electrons are retarded to almost 0 eV kinetic energy at the foil. When an electron is retarded so much that its forward velocity becomes less than 0, it is in fact reflected at the foil. Consider an electron beam having a certain energy spread, whose central energy is reduced to around 0 eV at the foil. Its faster electrons still have sufficient energy to pass, its slower electrons are reflected at the foil. Thus the foil can be used as a high pass energy filter. Because the foil filters on the electrons forward energy, the angle must be taken into account as well. Let at some reference plane the electron have an energy E and an angle α with respect to the foils surface normal. Then the criterion for passing this high pass filter can be written as:

$$E \cdot \cos^2 \alpha > \Delta U, \tag{2.1}$$

where ΔU is the potential difference between the reference plane and the foil. Note that for E and ΔU the values with respect to the vacuum level should be taken.

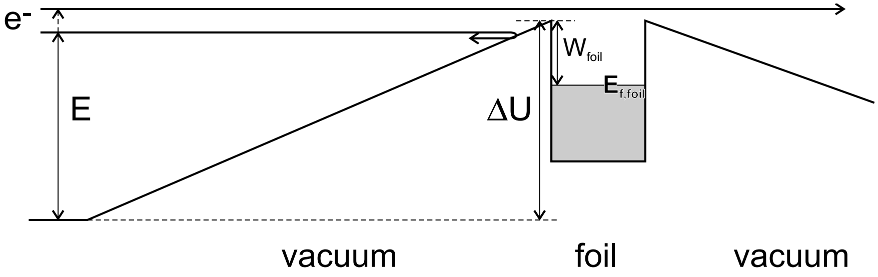

Figure 2.2: *Energy scheme, demonstrating the high pass filtering effect of the foil.*

For each energy E larger than ΔU, the high pass filter will act as an angle limitation. The electrons can only pass when the angle satisfies

$$|\sin \alpha| < \sqrt{1 - \frac{\Delta U}{E}}. \tag{2.2}$$

The reduction of the energy spread and the angular spread involves a reduction of the beam current, as this is achieved by blocking a part of the incoming electrons. The angle limitation effect by the foil is equivalent to that of an aperture. This does not affect the reduced brightness of the beam, the decrease of the current is proportional to the reduction of the solid opening angle. Reducing the energy spread does lead to a reduction of the reduced brightness.

From the classical point of view, all the electrons that satisfy the criterion in equation 2.1 will be transmitted, as they do not meet a potential barrier that is higher than their own forward kinetic energy. However, this does not take into account the wave character of the electrons. When the electrons enter the foil, their kinetic energy is increased with an amount equal to the workfunction and the height of the Fermi level of the foil (see figure 2.3). As a consequence, the wavelength is decreased and quantum mechanical reflections at the interfaces may occur. This will be discussed in section 2.4.

2.3 Scattering

The electrons that can enter the foil have at least an energy of W_{foil} above the Fermi level of the foil. In bulk material these electrons will eventually thermalise to the Fermi level via scattering. For the applications discussed in this thesis, the scattering must be minimised, because the objective is that a significant part of the electrons can traverse the foil ballistically.

2.3.1 Scattering mechanisms

Scattering of electrons in bulk material is a statistical process. Therefore the current $I_{ballistic}$ of ballistic - that is unscattered - electrons decays exponentially with the distance Δx being travelled through the material:

$$I_{ballistic} = I_{injected} e^{-\Delta x / L_{mfp}}. \tag{2.3}$$

$I_{injected}$ is the injected current and L_{mfp} is the mean free path: the average distance, measured along the trajectory, that an electron with a given energy can travel between two scatter events. Except for the energy, this mean free path also depends on the type of material.

Scattering can be either inelastic or elastic. In an inelastic collision, the electron loses kinetic energy, opposed to elastic collisions in which the electron energy is conserved and only a momentum change occurs. Depending on the geometry and the application, elastically scattered electrons may still have a high probability to escape the material and contribute to the collected current. This contribution of elastically scattered electrons will give rise to a non-exponential decay of the collected current on the film thickness. However when the electron energy is just above the workfunction, a small momentum change will already leave the electron with insufficient forward energy to escape. So in this situation also the elastically scattered electrons have a small escape probability and the collected current will be equal to the ballistic current.

In the applications discussed in this thesis, the electrons typically have an energy of W_{foil} above the Fermi level, which is approximately 4 - 5 eV for most conducting materials. At this energy, the scatter mechanisms that should be considered are electron-electron scattering and electron-phonon scattering. For plasmon excitations, in which the electrons are brought into a collective oscillation, the onset energy is 10 eV or above, so these may be disregarded.

A qualitative description of the scattering mechanisms at low energy was first given by Wolff [65]. His objective was to give a description of the transport mechanisms of secondary electrons which have energies below 50 eV. The main way the electron loses its energy is by collisions with conduction electrons: electron-electron scattering. The average energy loss in such a collision is about half of its energy above the Fermi level. That means that after the first collision, the electrons remaining energy is already insufficient to escape the material. At zero temperature, the incoming electron can not thermalise to a state below the Fermi level and the excited electron must be excited to an energy above the Fermi level. Thus an electron with an energy E_δ above the Fermi level can only interact with conduction electrons with an energy between $E_f - E_\delta$ and E_f. This gives rise to a decreasing scattering probability with decreasing energy. Quinn [49] has derived a quantitative theory for free-electron-gas-like metals. Based on this theory, Kanter [29] gives an expression for the electron-electron interaction mean free path, showing that it is proportional to $(E_\delta + E_f)/E_\delta^2$. Though several simplifications were necessary to obtain this result, there is a reasonable agreement between this theory and measured mean free paths. The point here is that the scattering is strongly dependent on the energy and that a lower energy is favourable to minimise the scattering.

Kanter [29] has determined the influence of electron-phonon interactions by studying the variation of the scattering with temperature. The mean free path due to electron-phonon scattering is inversely proportional with temperature and depends only weakly on the electron energy, whereas the electron-electron scattering is almost independent of temperature. Thus the contributions of both to the total scattering can be separated. Kanters measurements on aluminium, silver and gold show that at room temperature and at an energy of 6 eV above the Fermi level, the electron-phonon mean free path is about an order of magnitude larger than the electron-electron mean free path. From this observation, it is evident that electron-phonon interactions are of minor importance to the total scattering. The energy loss in an electron-phonon collision is small (<0.03 eV), but due to the momentum change, most electrons will retain insufficient forward energy to escape after such a collision. Thus the effect of electron-phonon scattering is a small additional loss of current.

2.3.2 Mean free path measurements

Because the mean free path is a very important parameter for the determination of the transmitted current, it will be evaluated here in more detail. In literature, different terms which are associated with the mean free path are used. Definitions of these terms can be found in a review article by Jablonski and Powell [24]. For convenience, the most relevant terms in relation to this work are listed here:

- Effective Attenuation Length (EAL): the average emission function decay length when the emission depth distribution function is sufficiently close to exponential for a given application.

- Inelastic Mean Free Path (IMFP): the average of distances, measured along the trajectories, that particles with a given energy travel between inelastic collisions in a substance.

When elastic collisions may be neglected, the effective attenuation length becomes equal to the inelastic mean free path.

Pioneering work in measuring the mean free path near 5 eV above the Fermi level has been done by Kanter [29]. He measured the transmission of a free electron beam through free-standing polycrystalline films of aluminium, silver and gold. With an in situ evaporation source, the thickness of the films could be increased. Under the assumption that the current has an exponential decay on the overlayer thickness, values for the effective attenuation length are obtained. This is referred to as the overlayer method. As noted above, Kanter has done the measurements at different temperatures, to separate the inelastic mean free path and the electron-phonon mean free path contributions. Inelastic mean free path values were obtained of 4 nm for gold and silver at 6 eV and 5 nm for aluminium at 5 eV above the Fermi level. The thickness of the foils was varied between 15 and 40 nm and the measured transmission ratios ranged from 10^{-4} to 10^{-6}. Because the transmission ratios are so small for foils exceeding around 20 nm thickness, mean free path measurements are difficult to perform.

In 1979, Seah and Dench have made an extensive compilation of measurements of the inelastic mean free path at different energies in solids [55]. They have grouped the materials under four headings: elements, inorganic compounds, organic compounds and adsorbed gases. The inelastic mean free paths as function of energy seem to be quite similar for all materials within a group. In general, the mean free path increases with increasing energy for energies above circa 200 eV. At these energies, plasmon excitations are the dominant scattering mechanism. Since the interaction time and the electron effective cross section decrease with increasing energy, the scattering decreases as well. Therefore experiments in which large transmissions are required, for example TEM imaging, are usually performed at high energy, typically 100 keV or above. For lower energy, the mean free path decreases until it reaches a minimum of a few tenths of a nanometer at around 50 to 200 eV. For even lower energies it increases again, in agreement with the theoretical evaluation in the previous section.

At an energy of 4 - 5 eV above the Fermi level, the compilation by Seah and Dench indicates a mean free path of about 5 nm for elements. Although this number may serve as a rough guide, several remarks are to be made about the interpretation of this result. First there is only few data at the energy of interest and these data have a relative large spread. Historically, the interest in the low energy region was mainly focussed on Auger Electron Spectroscopy (AES) and X-ray Photoelectron Spectroscopy (XPS). In order to determine the surface sensitivity of these techniques, the mean free path had to be known. Therefore, most of the data in the low energy region is at approximately 30 eV and above. Secondly the experimental techniques used to obtain these results must be discussed, which will be done below.

Most of the measurements at energies around or just above the Fermi level are performed with photoelectrons or tunnel emitted electrons and most of these experiments date from before 1979. References can be found in the article by Seah and Dench [55] and also in an article by Heiblum on tunnelling emitter devices [19] (the latter presents a table with data for the range 0.7 to 10 eV, which is more convenient for finding specific measurements). Usually, the overlayer method is used to determine the electron attenuation. Since the attenuation is determined solely as function of the overlayer thickness, it is not necessary to know where the electrons had started and interface effects are excluded. In tunnel emission experiments and in experiments with a free electron beam, similar to that by Kanter[29], the injected current is known and thus the transmission ratio can be determined. By extrapolation, a value for the transmission at zero thickness can be obtained. This will normally result in a value lower than unity, giving an indication of the effect of scattering and reflection at the interfaces for the specific experiment. For example Kanter found that extrapolation of his measurements resulted in a transmission of approximately 0.02 at zero thickness. In various papers, Powell and Jablonski have given a review of the overlayer method and its shortcomings (see for example [25, 26, 47]). In short, several implicit assumptions are made: the overlayer thickness must be uniform and well known, its composition must be known and surface roughness must be negligible. Whether all these conditions were met is at least arguable. Also an intrinsic angular spread in the beam and elastic scattering (which causes an angular spread as well) are simply ignored. Electrons travelling under an angle with the surface normal will be more attenuated because they effectively traverse a larger distance. Thus a smaller mean free path may be measured when this is not taken into account. When the measurement is performed at an energy just above the threshold for emission, electrons travelling non perpendicular to the surface will be reflected due to the highpass forward energy filtering effect, so in this specific case it is allowed to ignore them. However, due to the energy filtering, only a very small current remains. Therefore measurements are often performed at a slightly higher energy, resulting in a larger emission current but also in a larger angular spread. Summarizing, one should realize that it is the effective attenuation length that is measured in these experiments and that this parameter depends on the specific experimental setup that has been used for the measurement.

Very few mean free path measurements are reported after 1980. One of them is by Yokoo et alii [66]. The emission properties were measured of metal-oxide-semiconductor cathodes with silicon and aluminium gates with different thicknesses. These measurements indicated a mean free path for hot electrons of 2.8 nm for aluminium and 4.4 nm for silicon. The authors note themselves that the value for aluminium is considerably lower than that in previous reports. They give as possible explanations differences in the energy distribution and in the film fabrication. Additionally, the exact electron energy for the measurement was not specified, making comparisons difficult.

Recently, Marx et alii have determined the probing depth of ultra violet photoelectron emission microscopy for silver overlayers [39]. They use this technique to image the magnetization in a polycrystalline iron film that is buried under a silver overlayer. Their samples were illuminated with light containing photon energies up to 5 eV. Thus the photoemitted electrons are in the range of the workfunction, 4.2 eV for silver, to 5 eV. By measuring the decreasing contrast as function of increasing overlayer thickness, they determined that the effective attenuation length for these photoelectrons is 16.2 nm. The authors note that this large value should not come as a surprise because it is in good agreement with the expectation, based on calculations and experiments, that the mean free path increases strongly for the energy decreasing towards the Fermi level. Their explanation that this steep increase is not observed for other materials is that scattering into empty states close to the Fermi level plays an important role. The expected increase of the mean free path for decreasing energy is based on the assumption that the remaining energy of the incoming electron must be above the Fermi level. But when empty states below the Fermi level are available, the electron has additional scattering possibilities. For noble metals as silver and gold, this effect is almost absent because the number of holes in the d-band is small.

2.4 Quantum mechanical reflection

When the electrons enter the foil, their kinetic energy is increased with an amount equal to the workfunction and the height of the Fermi level of the foil (see figure 2.3). As a consequence, the wavelength is decreased. When the electron energy is of the order of the potential step at the interface or lower, this effect may not be neglected and quantum mechanical reflections at the interfaces will occur.

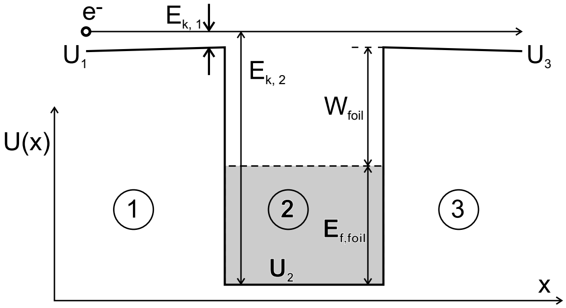

Figure 2.3: *Energy scheme for an electron wave entering the foil.*

In approximation, the foil can be considered as a rectangular well, see figure 2.3. First, the situation in which the electron wave is assumed unscattered in the foil is described concisely. A comprehensive treatment of this problem can be found in many quantum mechanics textbooks. In section 2.5 the model will be extended with an electron wave that is attenuated in the foil, due to the scattering of electrons.

For a one-dimensional system, the wave function $\Psi(x,t)$ can be represented as:

$$\Psi(x,t) = \psi(x)e^{-iE_k t/\hbar}. \tag{2.4}$$

x denotes position, t time, E_k is the electron kinetic energy and $\hbar$ is the reduced Planck's constant ($h/2\pi$). $\psi(x)$, the eigenfunction of the electron wave, is found by solving the time independent Schrödinger equation. For the three regions in figure 2.3 the solution is:

$$\begin{aligned} &1. \quad \psi(x) = e^{ik_1x} + Re^{-ik_1x} \\ &2. \quad \psi(x) = Pe^{ik_2x} + Qe^{-ik_2x} \\ &3. \quad \psi(x) = Se^{ik_3x}. \end{aligned} \tag{2.5}$$

P, Q, R, S are (complex) constants. Their values are determined by the boundary conditions that the eigenfunction and its first derivative are continuous. k_i is the wave vector of the electron in region i:

$$k_i = \frac{\sqrt{2mE_{k,i}}}{\hbar} = 5.123\sqrt{E_{k,i}}. \tag{2.6}$$

$E_{k,i}$ is the kinetic energy in region i and m is the electron mass. The right hand side holds for k_i in nm^{-1} and $E_{k,i}$ in eV. The kinetic energy of the electron in the foil is:

$$E_{k,2} = E_{k,1} + W_{foil} + E_{f,foil}. \tag{2.7}$$

The ratio of transmitted electrons is:

$$T = \frac{k_3}{k_1}|S|^2. \tag{2.8}$$

Solving S with the boundary conditions mentioned above and substituting it in equation 2.8 results in:

$$T = \frac{4k_1k_3}{2k_1k_3 + k_1^2 + k_3^2 + \left(k_2^2 + \frac{k_1^2k_3^2}{k_2^2} - k_1^2 - k_3^2\right)\sin^2(k_2L)}. \tag{2.9}$$

When the workfunctions at both foil surfaces are the same, U_3 and U_1 are equal and also k_3 and k_1 are equal. Then the equation simplifies to:

$$T = \frac{4k_1^2}{4k_1^2 + \left(k_2^2 + \frac{k_1^4}{k_2^2} - 2k_1^2\right)\sin^2(k_2L)}. \tag{2.10}$$

The transmission coefficient now depends on three parameters: The thickness of the foil (L), the kinetic energy of the incoming electron ($E_{k,1}$) and the potential step at the foils surface ($W_{foil} + E_{f,foil}$). In figure 2.4, the oscillating behaviour of the transmission as function of the energy is shown.

2.5 Quantum mechanical reflection for an attenuated wave

Due to scattering, the intensity of the electron wave in the foil is reduced by a factor $e^{-\Delta x/L_{mfp}}$. Since the intensity is the square of the amplitude of the wavefunction, the amplitude is reduced by a factor $e^{-\Delta x/2L_{mfp}}$. Let the foils entrance plane be positioned at $x = 0$. Then for the incoming wave, the travelled distance Δx is simply equal to x and for the first reflected wave it is $2L - x$. After every reflection in the foils entrance plane, Δx is increased with $2L$, causing an extra attenuation of $e^{-2nL/2L_{mfp}}$ for these reflected waves, with n the number of reflections in the entrance plane. The wavefunction in the foil is the summation over the incoming and all reflected waves:

$$\Psi(x,t) = \sum_{n=0}^{\infty}\left(Ae^{ik_2x}e^{-x/2L_{mfp}} + Be^{-ik_2x}e^{-(2L-x)/2L_{mfp}}\right)e^{-nL/L_{mfp}}e^{-iE_{k,2}t/\hbar}. \tag{2.11}$$

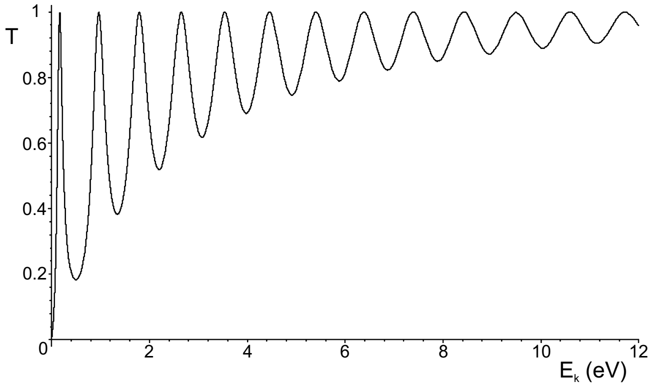

Figure 2.4: *Transmission vs. energy incoming electron for $L = 5$ nm and $W_{foil} + E_{f,foil} = 10$ eV*

Only the term $e^{-nL/L_{mfp}}$ is affected by the sum operator. The result of the summation over this term is just a constant multiplication factor. Thus, the eigenfunction in the foil can be written as:

$$\psi(x) = Ce^{ik_2x}e^{-x/2L_{mfp}} + De^{-ik_2x}e^{-(2L-x)/2L_{mfp}}. \tag{2.12}$$

The eigenfunction in the region before and after the foil has the same form as in 2.5. The values of the constants C, D, R and S again follow from the boundary condition that the eigenfunction and its first derivative must be continuous. Substituting S in formula 2.8 results in the transmission ratio. This procedure can easily be executed with a mathematical program, for example Maple [23], however the resulting formulas are rather complicated. Only the result for $k_1 = k_3$ will be listed here in formula:

$$\begin{aligned} T \;=\; & 16k_1^2\left(\frac{1}{4L_{mfp}^2} + k_2^2\right) \Bigg/ \left[\left(\frac{1}{4L_{mfp}^2} + (k_2+k_1)^2\right)^2 e^{\frac{L}{L_{mfp}}}\right. \\ & + \left(\frac{1}{4L_{mfp}^2} + (k_2-k_1)^2\right)^2 e^{-\frac{L}{L_{mfp}}} \\ & + 2\left(\frac{k_1^2}{L_{mfp}^2} - \left(k_2^2 - k_1^2 + \frac{1}{4L_{mfp}^2}\right)^2\right)\cos(2k_2L) \\ & \left. + 4\,\frac{k_1\left(k_2^2 - k_1^2 + \frac{1}{4L_{mfp}^2}\right)\sin(2k_2L)}{L_{mfp}}\right] \end{aligned} \tag{2.13}$$

A better impression of the transmission behaviour can be obtained from graphical plots (figures 2.5 to 2.8). In order to give a realistic graph of the energy dependence of the transmission, the energy dependence of the mean free path should be included.

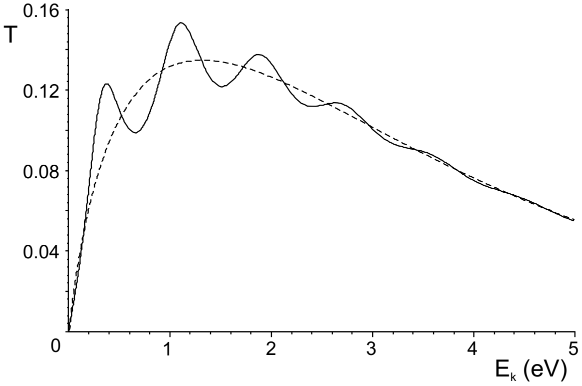

Figure 2.5: *Transmission vs. energy incoming electron for $W_{foil} = 5$ eV, $E_{f,foil} = 5$ eV, a foil thickness of 5.15 nm and the mean free path according to formula 2.14 with $K = 12.5$ nm/eV (corresponding to $L_{mfp} = 5$ nm at $E = 5$ eV). Dashed line: Transmission in the limit of negligible interference, calculated with formula 2.16.*

In line with the expression given by Kanter [29] (see section 2.3.1), the mean free path is formulated as:

$$L_{mfp} = K\frac{E_\delta + E_f}{E_\delta^2}. \tag{2.14}$$

K is a constant and E_δ is the energy of the electron with respect to the Fermi level of the foil, thus:

$$E_\delta = E_{k,1} + W_{foil,l} = E_{k,2} - E_{f,foil} = E_{k,3} + W_{foil,r}, \tag{2.15}$$

where $W_{foil,l}$ and $W_{foil,r}$ are the workfunctions at the left and right side of the foil. If not stated otherwise, these will be set equal. Figure 2.5 shows the transmission versus the kinetic energy of the incoming electron for a typical metal foil. When comparing with the graph for an unscattered wave (figure 2.4), it is evident that the scattering causes a considerable loss of current and a decrease of the oscillations. For higher energies, the transmission decreases due to the increasing mean free path. Nevertheless, the first peak in the graph is lower than the second peak. This is due to the larger quantum mechanical reflection at the foils exit plane for lower energies. This effect does not show up in the transmission graph for an unscattered wave, because in the absence of scattering, the reflected waves can eventually add up to unity transmission.

When the reflected wave is attenuated very strongly, the interference of the reflected wave with the incoming wave becomes negligible. Then, the transmission is simply the remainder after the effects of twice a quantum mechanical reflection at a potential step (the entrance and the exit plane of the foil) and scattering of electrons in the foil:

$$T = \frac{4k_1k_2}{(k_1+k_2)^2}\frac{4k_2k_3}{(k_2+k_3)^2}e^{-\frac{L}{L_{mfp}}} \tag{2.16}$$

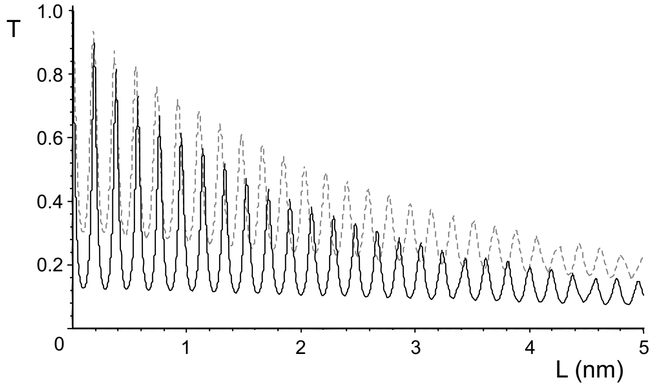

Figure 2.6: *Transmission vs. foil thickness for $W_{foil} = 5$ eV, $E_{f,foil} = 5$ eV and a mean free path of 5 nm. Black line: kinetic energy in the vacuum of 0.35 eV, dashed grey line: 1.0 eV.*

This is indicated by the dashed line in figure 2.5.

Figures 2.6 to 2.8 show the dependence of the transmission on the foil thickness, the mean free path and the potential step at the foil-vacuum interface. The transmission versus the foil thickness (figure 2.6) oscillates with a period of half the size of the wave vector in the foil (see the $cos(2k_2L)$ and the $sin(2k_2L)$ terms in formula 2.13) which is approximately 0.2 nm. This means that if the transmission should be in one of the maxima for the whole beam, the foil must be atomically flat within the diameter of the electron beam. Although not impossible, this is a severe demand. For increasing energy, the amplitude of the oscillation and thus the relative difference between minima and maxima in the graph decreases rapidly.

The oscillations shown in figure 2.5 have not yet been observed in experiments. The model uses a straight rectangular well. In reality, the potential step at the interfaces will have a smoother shape, hence the oscillations may be less pronounced. But more important is that a high resolution is required to observe the oscillations in a measurement. The thickness requirement mentioned above should be met and additionally the energy resolution should be better than 0.5 eV. These requirements have not been met in transmission measurements reported so far.

For the settings in figure 2.5, a transmission of only 10 - 15 % can be reached. As mentioned in section 2.3.2, Marx et alii had measured an effective attenuation length for silver of 16.2 nm in an energy range of 4.6 ± 0.4 eV [39]. An increase of the mean free path from 5 nm to approximately 16 nm will significantly improve the transmission (see figure 2.7). A decrease of the foil thickness with the same factor will have an identical effect, but this is not a practical possibility at the moment. Figure 2.9 shows the transmission for a 5 nm thick silver foil with a mean free path of 16.2 nm at 4.6 eV. With such a foil, a transmission of 50 to 55 % can be obtained. In order to optimise the transmission and the energy filtering, the electron beam energy can be centred to the second peak in figure 2.9 at 1.3 eV. The left and right flank of the peak serve as respectively a high and low pass filter.

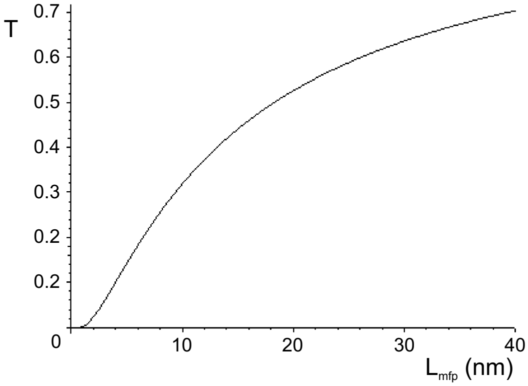

Figure 2.7: *Transmission vs. mean free path for* $W_{foil} = 5$ *eV,* $E_{f,foil} = 5$ *eV, a foil thickness of 5.15 nm and a kinetic energy in the vacuum of 0.35 eV.*

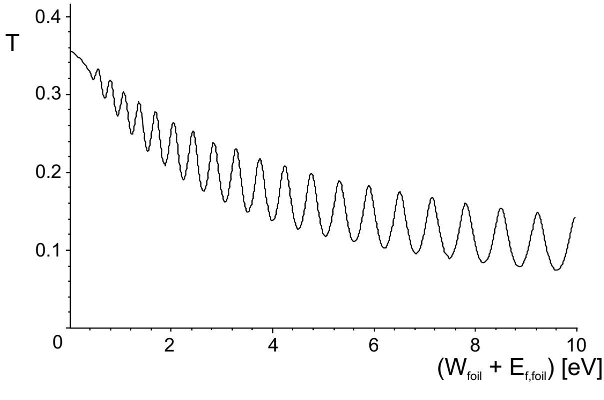

Figure 2.8: *Transmission vs. potential step* ($W_{foil} + E_{f,foil}$) *for a foil thickness of 5.15 nm, a mean free path of 5 nm and a kinetic energy in the vacuum of 0.35 eV.*

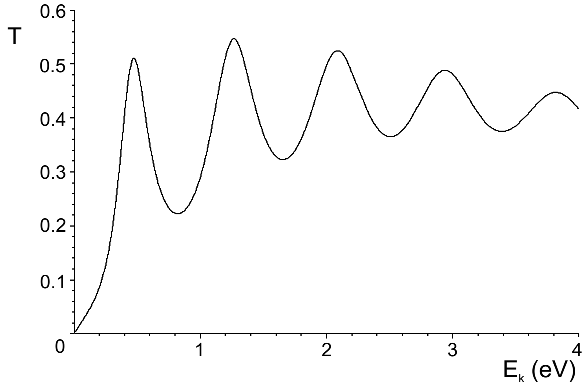

Figure 2.9: *Transmission vs. energy of the incoming electron for a 5 nm thick silver foil,* $W_{foil} = 4.2$ *eV,* $E_{f,foil} = 5.5$ *eV and the mean free path according to formula 2.14 with* $K = 33.9$ *nm/eV (corresponding to* $L_{mfp} = 16.2$ *nm at* $E = 4.6$ *eV).*

The demand that the foil must be atomically flat is quite severe. The oscillations in the transmission versus the foil thickness are due to the wave vector change at the foil-vacuum interface. By going to a somewhat higher energy, this effect will be reduced. However, this may involve increased electron scattering and the energy selectivity decreases as well for increasing energy, so in this case the energy filtering will be given up. Alternatively, if somehow the potential step at the foil vacuum interface can be reduced, the change in wave vector at the foil-vacuum interface will decrease as well. The analysis here was aggravated at a simple free-electron-gas like metal, for which the potential step is typically 10 eV. But for materials with a more complicated electronic structure, complete different values for the potential step may be found. Furthermore, one could look for anisotropic crystals which have a very short k-vector in a specific crystal orientation. The wave vector scales with the square root of the energy, so a considerable reduction of the potential step is necessary to obtain a noticeable effect.

2.6 Conclusion

Until now, the use of thin foils for electron microscopy applications has been limited to transmission of the electron beam at high voltage, because this was considered the only manner to achieve a sufficient transmission ratio. This chapter has discussed the transmission at very low energy and it can be concluded that a sufficient transmission at very low energy is a realistic prospect.

Measurements for a number of metals indicate a mean free path of about 5 nm at 5 eV above the Fermi level. Based on the combined effects of scattering and quantum mechanical reflection, a transmission of approximately 10% is expected for a foil having both a thickness and a mean free path of about 5 nm. This may seem low, but in chapter 8 an interesting novel application will be shown for which this is already sufficient. For high transmission ratios, of about 50% and above a mean free path of around 20 nm or better is desired. Because of the small amount of data and the experimental techniques used, it is premature to draw definite conclusions from the measurements that reported the value of 5 nm. The fact that recently a value of 16.2 nm was measured for silver is encouraging. The dominant scattering mechanism is electron-electron scattering. Therefore one should look for a material with such an electronic configuration, that the possibilities for an incoming electron to interact with conduction electrons are minimal. At low energy, the electron-electron scattering decreases with decreasing energy. Therefore materials with a low workfunction or other means to lower the workfunction of the foil are attractive, because it allows the electron to travel at a lower energy with respect to the Fermi level. When the electron-electron scattering can be reduced considerably, the electron-phonon mean free path will become the limiting factor, which is around 30 - 40 nm [29].

In order to make optimal use of the energy filtering effect of the quantum mechanical reflections, the foil must be atomically flat within the diameter of the beam. This is a severe demand, but not impossible nowadays.

Chapter 3

Fabrication of ultra-thin foils

3.1 Introduction

The vacuum electron source proposed in chapter 4 requires an ultra-thin free-standing metal foil within tunnelling distance of a sharp metal tip. The foil acts as an energy filter for tunnelled electrons. In this way the energy-spread of the electron source can be reduced considerably with respect to a conventional cold field-emitter. In order to have sufficient transmission current through the foil, its thickness has to be of the order of the mean free path. This is typically 5 nm for electrons having an energy of a few eV. Kazmiruk et alii [2] have fabricated 5 nm thick platinum foils, using a microfabrication process. An array of 2 μm × 2 μm windows, containing the free-standing foils, was patterned in a Si_3N_4 membrane. A Scanning Tunnelling Microscope (STM) is used to position a sharp tip in front of one of these foils.

However, with STM it is very difficult to locate features of a few micrometers on a sample as large as a few millimetres, especially when the STM is mounted in an Ultra High Vacuum (UHV) system with limited means for optical inspection. Therefore a search pattern has to be designed around the area of interest. Here we describe a fabrication process for a new series of samples, containing 5 - 8 nm thick free-standing chromium foils in a Si_3N_4 membrane and a search pattern which facilitates the positioning of an STM tip in front of a foil.

3.2 Fabrication Process

The fabrication of these samples is performed on square pieces of 19 mm × 19 mm. These pieces are sawn out of a 4” Si(100) wafer, thickness 525 ± 20 μm, which is covered with 100 nm Si_3N_4 layers on both sides (figure 3.1a). The fabrication can be divided in three parts. First square holes and scribe lines are patterned on the backside of the pieces, respectively for creating the membranes and breaking the pieces into smaller samples afterwards. Secondly a pattern of markers is made on the front side of the samples. The last step is the deposition of a thin Cr film on the backside and making holes in the membrane from the front side, to obtain free-standing Cr foils. The whole process will be described in detail below.

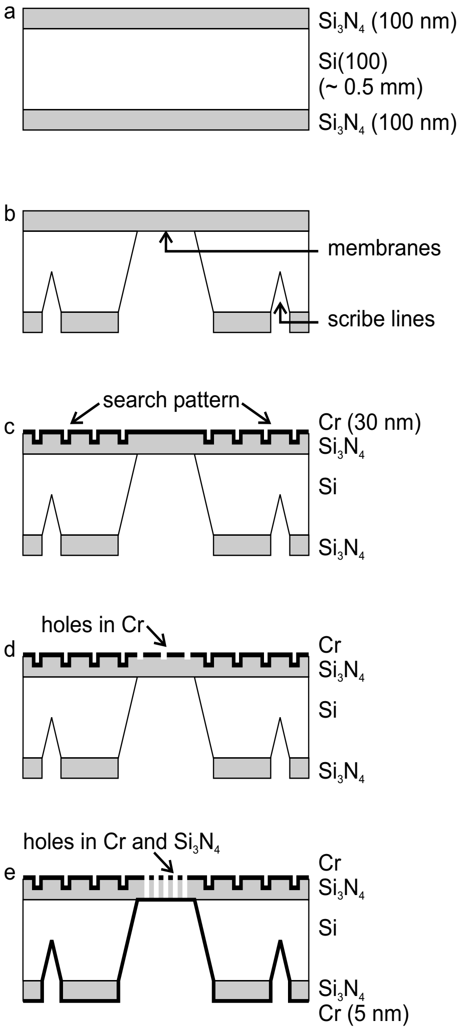

Figure 3.1: *Overview of the production process.*

In figure 3.1 the process is depicted schematically. The 19 mm × 19 mm pieces are sawn out of the wafer, with sawing directions parallel to the main crystal axes. The pieces are subjected to a cleaning procedure of a few steps, containing treatment in acetone, HNO_3, water and isopropanol. On both sides of the pieces, a PMMA resist layer is spun. The layer on the front side only serves as a protection layer against mechanical damage. On the backside a square mesh of scribe lines is written with Electron Beam Lithography, dividing the pieces into 2.12 mm × 2.12 mm samples. The width of the lines is 600 μm. Simultaneously a square window, size 836 μm × 836 μm, is written in the centre of each sample (see figure 3.2). The Electron Beam

Pattern Generator (EBPG) used for all lithography operations in this process is an EBPG5 HR100 FEG. For this step the resolution is set to a relatively poor value, 0.25 μm, to minimise the time of writing. After writing the pattern, the PMMA is developed by putting the sample in a mixture of methylisobutylketone and isopropanol (ratio 1:3) for 70 s. The samples are cleaned in an oxygen plasma for about 15 s, to be sure that the exposed areas are free of remains of resist or contamination. Then the Si_3N_4 in the exposed areas is removed in a SF_6/He plasma etch. To be sure that no contamination is left on the silicon, the samples are treated again in an oxygen plasma etch for about 20 s. The Si_3N_4 layer on the front side was still protected by a resist layer, which is stripped at this point. Next, Si is removed by etching for 4 hours in a 30% KOH solution at 85 °C. This anisotropic etch results in pyramidal holes, because Si is etched faster in the <100> direction than in the <111> direction. Also the KOH etchant erodes convex corners very fast. Therefore it is sufficient to write only outer contours with the EBPG, it is not necessary to expose all the interior of the lines and the windows (see figure 3.2). This reduces the time of writing from about 4 hours to about 30 minutes. The etch stops at the Si_3N_4 layer on the front side, creating 100 μm × 100 μm Si_3N_4 membranes in each sample (figure 3.1b). The square mesh is etched as well, creating the scribe lines for separating the samples afterwards. The samples are cleaned with water, HNO_3, and isopropanol.

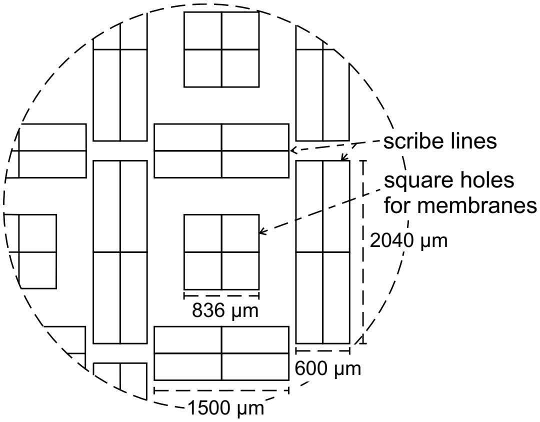

Figure 3.2: *Pattern on the backside for the membranes and the scribe lines. The EBPG only writes the contours, the black lines in the picture.*

The front side is masked with a PMMA layer. With Electron Beam Lithography a pattern of markers is written in this layer, around the membrane over the whole sample. On every 19 mm piece, 7 by 7 samples are written. The search pattern has to be aligned to the membranes. Because the membranes are transparent for 100 keV electrons, they can serve as alignment markers. On every piece 3 membranes are used for this purpose and lost for further sample production. Figure 3.3 shows an optical microscope image of part of the search pattern. It consists of arrow shaped markers of three different sizes. The farther away from the membrane, the larger the markers, so that during STM inspection there is some indication of the distance from the membrane. The smallest markers are within a square area of 196 μm × 196 μm, the largest outside a square of 540 μm × 540 μm. The three different marker sizes are: length 6 μm by width 2 μm, 4 μm by 2 μm and 2 μm by 1 μm. The lateral spacing is 8 μm, a convenient value as the lateral range of our STM is 12 μm. The resolution of the EBPG is set to 0.25 μm. For writing a pattern with EBPG, a simple rectangular geometry is preferred. Therefore the markers are arranged in 4 quadrants, each of them having all markers pointing in the same direction.

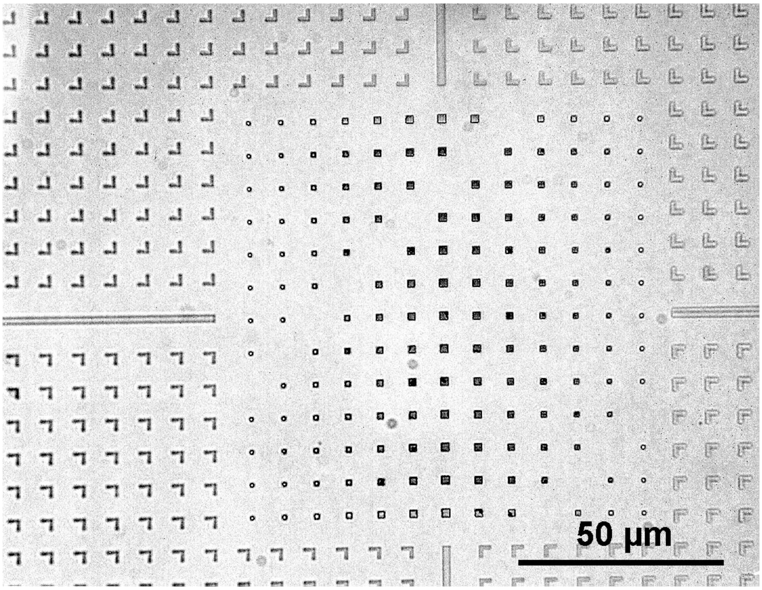

Figure 3.3: *Optical Microscope Photo of the search pattern markers, around the array of thin foils.*

The samples are subjected to the same development and oxygen-plasma etch as after the first lithography step. The Si_3N_4 in the exposed areas is removed with a SF_6/He plasma etch to a depth of 30 nm. This is a convenient height difference for the later STM inspections. Removing the resist and cleaning the surface is done by putting the samples in acetone, water, HNO_3 and isopropanol and finally treat them in an oxygen plasma etch for about 20 s.

With E-gun evaporation, a 20 nm Cr layer is deposited on the front side, to get a conducting surface layer (figure 3.1c). The deposition rate is about 0.01 - 0.02 nm/s, the pressure is about $2 \cdot 10^{-6}$ mbar.

The front side is again masked with PMMA and on the membranes an array of small square holes is written with EBPG (see figure 3.3). The resolution of the EBPG is set to 50 nm. The size of the holes ranges from 0.6 μm to 3 μ m. Lateral spacing is also 8 μm. The pattern is aligned using the same membranes as alignment-markers as during the previous lithography step. After development of the PMMA, the Cr in the holes is removed in a wet etch (figure 3.1d). After this etch, the sample is cleaned with water, acetone and isopropanol and exposed to an oxygen plasma etch for 5 minutes.

From the backside a thin Cr film, thickness 5 - 8 nm, is deposited with E-gun evaporation, using the same conditions as for the previous Cr deposition. From the front side, the Si_3N_4 in the holes in the Cr layer is etched in a SF_6/He plasma etch. This etch stops at the thin Cr layer on the backside, thus creating the free-standing foils (figure 3.1e). Although this etch is very selective to Si_3N_4 in comparison to Cr, care must be taken that the very thin Cr layer is not damaged. Therefore the conditions of the etch are chosen such that the sputter yield is low. Then the samples are subjected again to an oxygen plasma etch for about 20 s to clean the surface.

Finally, the samples are broken apart mechanically on the scribe lines.

3.3 Results

Several batches of samples, containing thin chromium foils and a search pattern, have been produced. These samples have been investigated with STM, optical microscopy and High Resolution Transmission Electron Microscopy (HRTEM).

The functionality of the search pattern has been tested in an STM in a UHV system. The lateral range of this STM is 12 μm. With slip-stick-movement, the tip of the STM can be moved from one spot to another over a range of about 4 mm. Starting at an arbitrary spot on the surface, an image such as shown in figure 3.4 is made. Then the tip is retracted and moved to the next spot, distance and direction depending on the size and direction of the arrow that has been observed. With this procedure the membrane can be found in about 5 steps. The limiting factor is not only the simple geometry of the search pattern, but also the inaccuracy of the slip-stick movement. The relative error in the displacement is of the order of 10%.

Because the samples have been exposed to air and to oxygen plasma etches, it may be assumed that the chromium surface is oxidised. Nevertheless the measurements show that the surface is still conducting and suitable for STM.

Figure 3.5 is an STM image of a hole in the membrane containing a free-standing foil. The measurement confirms that the foil is conducting as well. From figure 3.6, a HRTEM image of a foil, it can be seen that the foil is closed and has a quite uniform thickness. HRTEM and diffraction measurements show that the foils contain Cr crystallites, but also an amorphous layer. This could be accounted for by a chromium oxide layer.

3.4 Conclusion

A microfabrication process is described to produce samples with a search pattern that enables finding a small area of interest with STM. The area of interest is a membrane, 100 μm × 100 μm square, containing 0.6 - 3 μm square windows with 5 - 8 nm thick free-standing Cr foils. This membrane is localised by making an STM image somewhere on the search pattern and then moving the tip in the direction as indicated by the image. Measurements show that with this iterative procedure, the membrane can be found in about 5 steps.

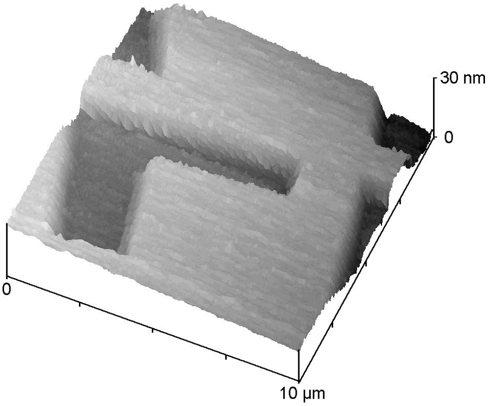

Figure 3.4: *STM image of a search pattern marker.*

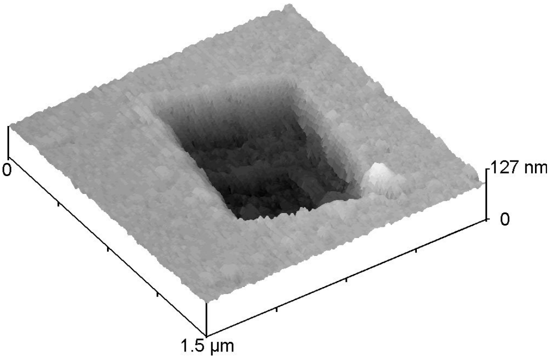

Figure 3.5: *STM image of a free-standing foil.*

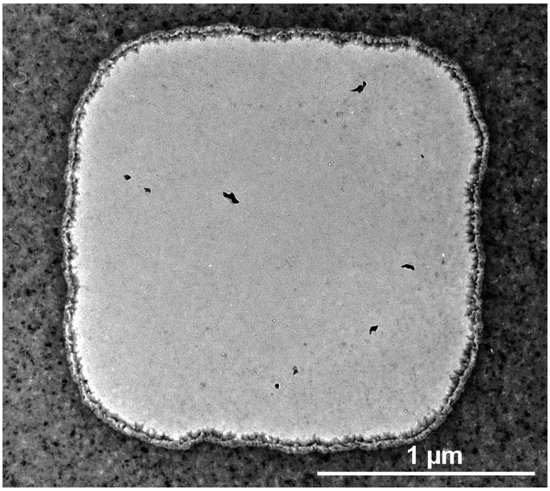

Figure 3.6: *HRTEM image of a Cr foil.*

Chapter 4

The Tunnel Junction Emitter

4.1 Introduction

Electron field emitters are used in a wide variety of applications, such as: electron microscopes, electron beam lithography machines, field emission displays, RF accelerators and vacuum micro electronics. Field emitters have some important advantages over thermionic emitters: they have a higher brightness and lower energy spread, they can operate at ambient temperature and they have a lower power consumption because no heating of a filament is required. Nevertheless, improvements are still desirable. For example the spatial resolution in low voltage electron probes is limited in part by the energy spread of the field emitter. Also a lower energy spread would allow to resolve fine spectroscopic detail in electron energy loss spectroscopy (e.g. chemical shifts of 50 to 100 meV). If it would be possible to operate a field emitter at low voltage, battery driven applications are in reach (e.g. displays for laptop computers). The tunnel junction emitter is expected to combine the properties of low energy spread, high brightness, operation at low voltage and low power consumption.

The tunnel junction emitter is constructed by placing a sharp tip within tunnelling range of a very thin metal foil (see figure 4.1). Between tip and foil a voltage larger than the workfunction of the foil surface is applied. Provided that the foil is sufficiently thin, a fraction of the tunnelled electrons will travel through the foil without scattering. Electrons with sufficient forward energy to overcome the workfunction are emitted into the vacuum . In this way the workfunction acts as a high-pass energy filter. Combined with the fact that the electrons originate from an atomic size tunnelling area, a monochromatic high-brightness electron source is expected. As for most metals the workfunction is of the order of a few eV, the source is operated at low voltage. Although the emitted current is only a fraction of the tunnel current, the power consumption is still low because of the low voltage operation and because no heating is required. The emitter can be operated at high frequency because only a small voltage difference is needed to switch between on and off and because the size of the emitter, and therefore its capacitance, can be kept small. This could be interesting for RF applications.

In this chapter the electron optical properties of the tunnel junction emitter will

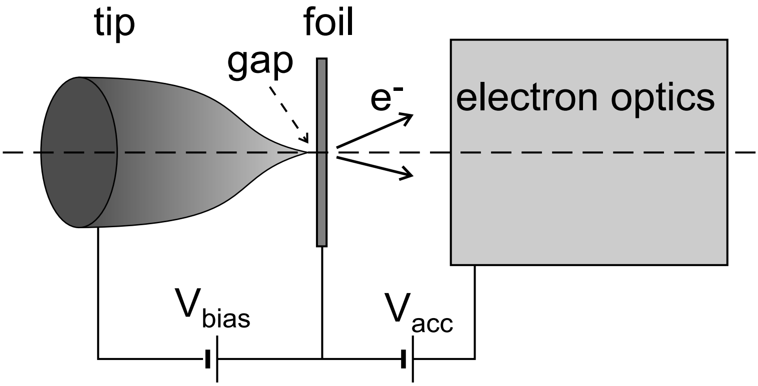

Figure 4.1: *Schematic view of the tunnel junction emitter.*

be calculated. In chapter 5, experimental work on the tunnel junction emitter will be presented.

4.2 Calculation of the electron optical characteristics

Van Bakel has calculated the electron optical characteristics of the emitter. A detailed treatment of this calculation was published in the Journal of Applied Physics [3]. For clarity, the essentials of this calculation will be repeated here. In addition the implications of operating an emitter in the diffraction limit are treated more extensively. A consequence is that the spherical and chromatic aberration of the accelerating field behind the emitter must be evaluated. Furthermore the Coulomb interactions are evaluated and the quantum mechanical interference effects are considered in comparison with the transmission of a free electron beam through a thin foil.

4.2.1 Modelling the emitter

The transport of electrons from the tip into the vacuum can be divided in three independent steps:

(1) Tunnelling of electrons from the tip through a vacuum gap into the foil.

(2) Electron transport through the foil.

(3) Transmission across the foil-vacuum emission surface.

It is assumed that the tunnel junction is operated in constant current mode, that is, the width of the gap between tip and foil is adjusted continuously by a feed-back system to keep the current to the foil constant. Furthermore it is assumed that the emitter is operated near the threshold for transmission of electrons through the foil. That means that the tunnel bias voltage must just exceed the potential barrier induced by the workfunction of the foil, typically 5 V. Throughout the whole model, several simplifications have to be made in order to make the calculation not too complicated. For some specific parts more sophisticated and complicated methods may exist, but have not been used because the extra effort would not lead to a significant improvement for the model as a whole.

The junction of a sharp tip in front of a flat foil is modelled by a simple planar junction with a small circular aperture of atomic size dimension. For the potential barrier between tip and foil a triangular shape is assumed. Figure 4.2 shows the energy scheme.

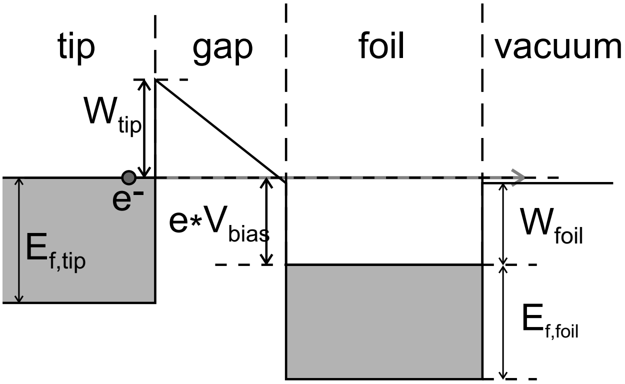

Figure 4.2: *Energy scheme of the tunnel junction emitter.*

For the calculation of the emitter characteristics, the energy and angular distribution of the tunnelled electrons must be known. The energy distribution of the tunnelled electrons is approximated well by:

$$\wp(\epsilon) = \frac{1}{\Delta\epsilon}\frac{e^{\epsilon/\Delta\epsilon}}{1+e^{\epsilon/kT}}, \text{ with } \Delta\epsilon \equiv \frac{\hbar}{d_{\text{gap}}}\sqrt{\frac{W_{\text{tip}}}{8m}}. \tag{4.1}$$

ϵ is the electron energy with respect to the Fermi level of the tip, d_{gap} is the size of the gap and m is the electron rest mass. Equation 4.1 holds for $kT \ll \Delta\epsilon$ (k: Boltzmann constant, T: temperature). $\Delta\epsilon$ represents the energy spread of the tunnelled electrons. Instead of trying to estimate the tunnel gap width, the energy spread is chosen equal to a typical value for a room temperature field emitter: $\Delta\epsilon = 0.2$ eV. The angular dependence is related to the energy dependence. A conduction electron in the tip having an angle of incidence α_{tip} with respect to the surface normal, has an amount of $E_{f,\text{tip}} \sin^2 \alpha_{\text{tip}}$ less forward energy. Based on this reduction of the forward energy, the angular spread and the angular dependence of the tunnelling probability in the small angle limit are derived.

$$(\Delta\alpha_{\text{tip}})^2 \equiv \frac{\Delta\epsilon}{E_{f,\text{tip}}} = \frac{\hbar}{d_{\text{gap}}E_{f,\text{tip}}}\sqrt{\frac{W_{\text{tip}}}{8m}}. \tag{4.2}$$

$\Delta\alpha_{\text{tip}}$ is the half width of the angular distribution on the tip side of the tunnel junction. Due to the potential difference between tip and foil, the electron beam is refracted, leading to an angular width in the foil of:

$$(\Delta\alpha_{\text{foil}})^2 = \frac{E_{f,\text{tip}}}{E_{f,\text{foil}} + eV_{\text{bias}}}(\Delta\alpha_{\text{tip}})^2 = \frac{\hbar}{d_{\text{gap}}(E_{f,\text{foil}} + eV_{\text{bias}})}\sqrt{\frac{W_{\text{tip}}}{8m}}. \tag{4.3}$$

The tunnelling probability as function of d_{gap}, ϵ and α_{tip} can conveniently be expressed as:

$$P_{\text{tunnel}}(d_{\text{gap}}, \epsilon, \alpha_{\text{tip}}) \propto e^{-d_{\text{gap}}/\Delta d_{\text{gap}}} e^{\epsilon/\Delta\epsilon} e^{-(\alpha_{\text{tip}}/\Delta\alpha_{\text{tip}})^2}. \tag{4.4}$$

For a work function and Fermi energy of both 5 eV for both the tip and the foil and a gap width of 1 nm, this results in values for the half-width angular distribution of: $\Delta\alpha_{\text{tip}} = 0.21$ rad and $\Delta\alpha_{\text{foil}} = 0.15$ rad. So far only an unapertured planar tunnel junction was evaluated. When a circular aperture of atomic size dimension is imposed, diffraction effects have to be taken into account. In the diffraction limit, the half opening angle is:

$$\Delta\alpha_{\text{foil}} = \frac{\lambda}{\pi R_t} \text{ with : } \lambda = \frac{h}{\sqrt{2mE_k}}, \tag{4.5}$$

in which R_t is the aperture radius, λ is the wavelength and E_k the electron kinetic energy in the foil. For the values of the work function and Fermi energy given above, the kinetic energy of electrons originating from the tips Fermi level is 10 eV and the wavelength is 0.4 nm. For an aperture radius of 0.35 nm, the resulting half opening angle is $\Delta\alpha_{\text{foil}} = 0.35$ rad. This is larger than the value derived for the unapertured planar tunnel junction. Thus the angular distribution of electrons is governed by diffraction, assumed that the estimates for the aperture radius, gap width, work function and Fermi energy are, in approximation, correct.

The next step is electron transport through the foil. Part of the electrons will be scattered, as discussed in section 2.3. For electrons that travel close to the foils surface normal, the attenuation of the ballistic current as function of the mean free path L_{mfp} and the foil thickness L is given by

$$I_{\text{ballistic}} = I_{\text{injected}} e^{-L/L_{\text{mfp}}}. \tag{4.6}$$

In section 2.3.1 it was concluded that at 4 - 5 eV above the Fermi level, electron-electron scattering is the dominant scattering mechanism and that the electron-electron interaction mean free path is proportional to $(E_\delta + E_f)/E_\delta^2$, with E_δ the electron energy relative to the Fermi level of the foil. Then the energy dependent mean free path, scaled to an experimentally measured value at an energy E_0, can be represented as

$$L_{\text{mfp}}(E_\delta) = L_{\text{mfp}}(E_0)\frac{E_0^2}{E_0 + E_{f,\text{foil}}}\frac{E_\delta + E_{f,\text{foil}}}{E_\delta^2}, \tag{4.7}$$

Electrons that have traversed the foil without scattering encounter the vacuum emission surface, which is modelled by a stepwise change in potential. This potential step is the actual high-pass forward energy filter. Because of quantum mechanical effects, part of the electrons with sufficient forward energy may still be reflected. Let

k_2 and k_3 be the forward components of the electron wave vector in the foil and after emission into the vacuum respectively, then the transmission probability is:

$$T = \frac{4k_2k_3}{(k_2+k_3)^2}. \tag{4.8}$$

In terms of the energy and the angle of incidence with the surface normal this becomes:

$$T(\alpha_{\text{foil}}, E_\delta) = \frac{4\cos\alpha_{\text{foil}}\sqrt{\cos^2\alpha_{\text{foil}} - (E_{f,\text{foil}} + W_{\text{foil}})/(E_\delta + E_{f,\text{foil}})}}{\left(\cos\alpha_{\text{foil}} + \sqrt{\cos^2\alpha_{\text{foil}} - (E_{f,\text{foil}} + W_{\text{foil}})/(E_\delta + E_{f,\text{foil}})}\right)^2} \tag{4.9}$$

A small part of the reflected electrons may travel forth and back the foil without scattering and can still be emitted. An electron entering the foil under an angle α_{foil} is laterally displaced over a distance $\alpha_{\text{foil}}L$ at the foils exit plane. After a roundtrip, the electron has an extra lateral displacement over a distance $2\alpha_{\text{foil}}L$. These indirectly emitted electrons give rise to a halo. In section 2.5 the interference between direct incoming and reflected electrons in a parallel beam is discussed. For the tunnel junction emitter the beam is divergent and has a small diameter. Therefore most electrons will be laterally displaced outside the beam after a roundtrip and interference effects will be much weaker. Interference effects are not included in the calculation. Because the angular distribution would have to be taken into account, it is too difficult to do so.

4.2.2 Calculation procedure

The vacuum emission current is the product of the tunnel junction current and the probability of tunnelled electrons to traverse the foil without scattering and cross the vacuum emission surface, taking into account their energy and angular distribution. An analytical solution, which requires an integration over ϵ and α_{foil}, is not possible. Therefore the vacuum emission probability is calculated numerically, using the Monte Carlo method. Each tunnelled electron is traced until it is emitted into the vacuum or absorbed in the foil, according to the following procedure:

(a) The electron is positioned at the tunnel junction and assigned a random angle and energy. Their probabilities are based on the angular and energy distribution, given by equations 4.1 to 4.4.

(b) The electron is given a random path length from an exponential distribution, parameterized by the mean free path. The energy dependent mean free path is calculated with equation 4.7.

(c) If this path length is shorter than the distance to be travelled until the electron encounters either surface, the electron is scattered and the procedure is terminated.

(d) The surface transmission probability is calculated with equation 4.9, the outcome decided using a random generator. If the electron is reflected, the procedure proceeds from step (b). An electron that is reflected before it is emitted is counted as indirectly emitted.

This calculation is performed for a large enough number of electrons.

4.2.3 Characterization of an emitter: brightness and energy spread

The two important properties characterizing the emitter are its energy spread and its reduced brightness. The energy distribution of the emitted electrons is used to calculate the energy spread that contains 50% of the vacuum emission current. The reduced brightness is the amount of current contained within a given source area ∂A and solid opening angle $\partial\Omega$, divided by the acceleration voltage V. This is a conserved property throughout an electron optical system and it is a measure for the ability to form a small probe with a high current density. The reduced brightness in $\mathrm{Am^{-2}sr^{-1}V^{-1}}$ is defined as:

$$B_r \equiv \frac{\partial I_{\mathrm{emission}}}{\partial A \partial \Omega V}. \tag{4.10}$$

For a full beam with a half opening angle $\Delta\alpha$ and originating from an area πR_t^2, this is approximately equivalent to

$$B_r \approx \frac{I_{\mathrm{emission}}}{\pi R_t^2 \pi (\Delta\alpha)^2 V}. \tag{4.11}$$

The spotsize, or to be precisely: the finite brightness contribution to the spotsize depends on the reduced brightness as:

$$d_{spot} = \frac{2}{\pi \alpha_{\mathrm{probe}}} \sqrt{\frac{I_{\mathrm{probe}}}{B_r V_{\mathrm{probe}}}}, \tag{4.12}$$

where d_{spot} is the diameter of the spot. Because the emitter is operated in the diffraction limit, the smallest possible spotsize is obtained by making the brightness contribution to the spotsize equal to the diffraction spotsize. This is achieved by letting $\Delta\alpha$ depend on R_t according to equation 4.5. A further reduction of the product $R_t \cdot \Delta\alpha$ is useless: the resulting increase of the reduced brightness can not be practically used because of the diffraction effects. By substitution of equation 4.5 into equation 4.11, the so-called diffraction limited reduced brightness is obtained, which can be regarded as the maximum practical usable reduced brightness. This is proportional to the emission current:

$$B_{r,\mathrm{diffr}} = \frac{2me}{h^2} I_{\mathrm{emission}} = 6.6 \cdot 10^{17} I_{\mathrm{emission}}.^{1} \tag{4.13}$$

From equation 4.13 it is evident that an accurate estimate for the source radius or the opening angle is not necessary to calculate the practical usable reduced brightness of a diffraction limited probe.

---

[1] Barth [5] reports a somewhat different result for the diffraction limited brightness. He has defined the brightness in terms of the diameter containing 50% of the current. The relation $\Delta\alpha_{\mathrm{foil}} = \lambda/(\pi R_t)$ used for the derivation in this chapter is based on the position of the first minimum in the diffraction pattern. The relation between the half opening angle and the radius encompassing 50% of the current is: $\Delta\alpha_{\mathrm{foil}} = 0.27\lambda/R_t$. Then equation 4.13 becomes: $B_{r,\mathrm{diffr}} = 9.2 \cdot 10^{17} I_{\mathrm{emission}}$.

Both the brightness and the diffraction spotsize contribute to the total spotsize. However, it must be pointed out that for a small emission current, the actual reduced brightness, calculated using the actual emission area and opening angle without considering diffraction effects, can be much larger than the diffraction limited brightness. In this case the brightness contribution to the spotsize is negligible. The diffraction contribution to the spotsize can be determined by substituting the diffraction limited brightness in equation 4.12. This demonstrates that for a diffraction limited beam, the diffraction limited brightness is the figure of interest because that determines the smallest possible spotsize.

Another consequence of operating the emitter in the diffraction limit is that the brightness in the probe may be diminished by the spherical and chromatic aberration. Normally the influence of these aberrations on the brightness can be ruled out with a beam limiting aperture. For a probe that is already diffraction limited, such a measure will increase the spot size due to diffraction. Therefore the spherical and chromatic aberration of the accelerating field behind the emitter must be analyzed here. The electrons that are emitted from the foil into the vacuum have a very small forward and radial velocity and must be accelerated. In a linear accelerating field, the electron trajectories will be parabolic. The situation is similar to that of emission microscopy, for which Bauer [7] has analyzed the aberrations. Under the assumption that the emission energy is small compared to the acceleration potential, the aberration discs of the accelerating field due to respectively the spherical and the chromatic aberration are:

$$\begin{aligned} d_{C_s} &= \sin^3\alpha \frac{LV}{V_{acc}} \\ d_{C_c} &= -2\sin\alpha \frac{L}{V_{acc}} \left(V_2 - \sqrt{V_1 V_2}\right). \end{aligned} \tag{4.14}$$

Here α is the emission half opening angle. The electrons have an energy distribution from eV_1 to eV_2 with the central initial energy being eV, hence the energy spread is $e\Delta V = e(V_2 - V_1)$. V_{acc} is the acceleration potential and L the distance from the emitter to the accelerator electrode. These are the disc sizes in the image plane for energy eV. In order to determine the disc sizes in a specific probe, the magnification from the source (at energy eV) to that probe must be included. When the emission energy approaches zero (implying $V_1 = 0$, $V_2 = \Delta V$) and consequently the emission half opening angle approaches 90°, as is the case for the tunnel junction emitter, the expressions simplify to:

$$\begin{aligned} d_{C_s} &= \frac{LV}{V_{acc}} \\ d_{C_c} &= -2\frac{L\Delta V}{V_{acc}} \end{aligned} \tag{4.15}$$

Both the starting energy and the energy spread are approximately 0.1 eV. The emitters source size is approximately equal to the wavelength, which is of the order of 1 nm at this energy. It can be seen that the field V_{acc}/L must exceed 10^8 V/m to keep the aberration discs below 1 nm. In a normal vacuum system, a field of 10^7 V/m can be obtained without flashovers between electrodes at about 1 mm distance. The maximum allowable field increases for electrodes at shorter distance from each other. Maybe a field of 10^8 V/m can be obtained with an extraction electrode very close to the foil. Alternatively such a field is easily obtained at the surface of sharp emitters because of the field enhancement. Thus for a final design it is recommended to give the emission surface of the tunnel junction emitter a shape resembling that of a field emitter, instead of a flat emission surface.

For slow electron beams, such as an electron beam that has just left the emitter, Coulomb interactions must be considered. These repelling interactions between the electrons cause displacements of the electron trajectories, which effectively result in a diminished brightness in the probe. The Coulomb interactions are mainly dependent on the beam current and the acceleration voltage. For an electron beam in an accelerating field, the dependencies do not lend themselves for an analytic expression and can better be calculated numerically. The calculation has been done with the slice method using Jiangs formulas [27, 28]. This method is as follows. The beam segment behind the emitter is divided into slices, perpendicular to the optical axis. The slices are sufficiently thin, such that in every slice the beam radius and voltage can be assumed constant. In every slice, the Coulomb interactions cause a deflection of the electrons, which leads to an increase of the angular spread of the beam. The deflection per meter in a slice at position z along the optical axis is:

$$\phi[r(z), V(z), I(z)] = \left(\frac{T_1 D_\lambda^{18/7} D_r^6 I(z)^{18/7} r(z)^{6/7} V(z)^{-15/7}}{T_4 + T_2^{1/7} D_r^6 D_\lambda^2 I(z)^2 r(z)^2 V(z)^{-1}} \right)^{7/6} \quad (m^{-1}). \qquad (4.16)$$

$r(z)$ is the beam radius and $V(z)$ the beam potential. $I(z)$ is the beam current which is constant for all z in the absence of apertures. D_λ and D_r are constants: $D_\lambda = \frac{m^{1/2}}{2^{7/2}\pi\epsilon_0 e^{1/2}}$, $D_r = \left(\frac{2\pi\epsilon_0}{e}\right)^{1/3}$, with ϵ_0 the permittivity of vacuum. The values of the coefficients T_1 and T_2 depend on whether the calculation is performed for a spot size defined by the full width half maximum or by the full width containing 50% of the current. For the latter, the values are: $T_1 = 4.618 \cdot 10^{-2}$ and $T_2 = 2.041 \cdot 10^5$. The value of T_4 depends on whether the spatial distribution of the beam is uniform or Gaussian. For a uniform distribution $T_4 = 6.25 \cdot 10^{-2}$.

The total deflection for the whole beam segment is obtained by summation of the deflections in all slices. In the summation, the magnification from the respective slice to the reference plane in which the total deflection is evaluated must be taken into account. Thus the summation becomes:

$$\Phi_{total} = \sum_n \phi[r(z_n), V(z_n), I(z_n)] \frac{r(z_n)}{r_{ref}} \sqrt{\frac{V(z_n)}{V_{ref}}}\, \Delta z_n, \qquad (4.17)$$

where z_n and Δz_n refer to the z-position and the thickness of the n^{th} slice, r_{ref} and V_{ref} are the radius and potential of the beam in the reference plane.

This deflection can be added to the beams full opening angle with a square root power sum, thus returning the increased angular spread. Because the probe size is inversely proportional to the opening angle, the probe size will increase with a factor:

$$\frac{\sqrt{\Phi_{total}^2 + (2\alpha_{ref})^2}}{2\alpha_{ref}}. \qquad (4.18)$$

The factor 2 comes in because α_{ref} is the half opening angle of the beam in the reference plane. The reduced brightness is inversely proportional to the square of the opening angle, hence the reduced brightness decreases with the square of this factor. For the calculation, it is convenient to use the relation:

$$\frac{1}{r_{ref}\sqrt{V_{ref}}} = \pi\alpha_{ref}\sqrt{\frac{B_r}{I}} \tag{4.19}$$

and to rewrite equation 4.17 as:

$$\frac{\Phi_{total}}{2\alpha_{ref}} = \frac{1}{2}\pi\sqrt{\frac{B_r}{I}}\sum_n \phi[r(z_n), V(z_n), I(z_n)]r(z_n)\sqrt{V(z_n)}\;\Delta z_n. \tag{4.20}$$

With this equation, the effect of the Coulomb interactions can be calculated without having to know the beam radius and potential in a reference plane.

It is assumed that the emitters reduced brightness depends on the beam current as given in equation 4.13. Then for a beam current of 1 nA and an accelerating field of 10^5 V/m, the decrease of the reduced brightness in the probe due to the Coulomb interactions is only 1%. When the high accelerating field of 10^8 V/m, necessary to reduce the chromatic and spherical aberration, is applied, the effect can be completely ignored (reduction $< 0.1\%$) for beam currents up to about 0.5 μA.

4.2.4 Calculation results

The graphs in figure 4.3 show the results of the Monte Carlo calculations. The parameters used in the calculation are: $\Delta\epsilon = 0.2$ eV, $kT = 25$ meV, $\Delta\alpha_{\text{foil}} = 0.35$ rad, $W_{\text{foil}} = 5$ eV, $E_{f,\text{foil}} = 5$ eV and $L_{\text{mfp}}(E_{f,\text{foil}} + 5\text{ eV}) = 5$ nm.

Figure 4.3a shows the ratio between the direct vacuum emission current and the tunnel current, as well as the energy spread as function of the excess tunnel bias voltage $V_{\text{bias}} - E_{f,\text{foil}}/e$. For increasing bias voltage, the emission current ratio increases, till it reaches a maximum of 0.1 at an excess bias voltage of 2 V. For higher bias voltages, the emission decreases due to the increased scattering at higher energies. The energy spread increases for increasing bias voltage, thus a trade-off exists between a small energy spread and a large emission current. This is plotted in figure 4.3b. The actual emission current and the reduced brightness scale with the tunnel junction current, which can best be obtained from experimental results. The measurements that will be discussed in sections 5.1 and 5.2 indicate that a stable tunnel current of 10 nA is possible. Then, at an excess tunnel bias voltage of 0.3 V, the emission current is 0.1 nA, 50% of which is contained within an energy range of 100 meV. Using equation 4.13, a reduced brightness follows of $6.7 \cdot 10^7$ Am^{-2}sr^{-1}V^{-1}. A maximum in the emission current ratio of 9% can be obtained, with an energy spread of 0.2 eV. With a 10 nA tunnel current, this results in a 0.9 nA emission current and a reduced brightness of $6 \cdot 10^8$ Am^{-2}sr^{-1}V^{-1}. For comparison: typical values for a Schottky emitter are $B_r = 2 \cdot 10^7$ Am^{-2}sr^{-1}V^{-1} with an energy spread of 0.5 eV. An additional note to these numbers must be made that recent research has shown that a reduced brightness of 1 to $2 \cdot 10^8$ Am^{-2}sr^{-1}V^{-1} can be obtained with a Schottky emitter [13, 61].

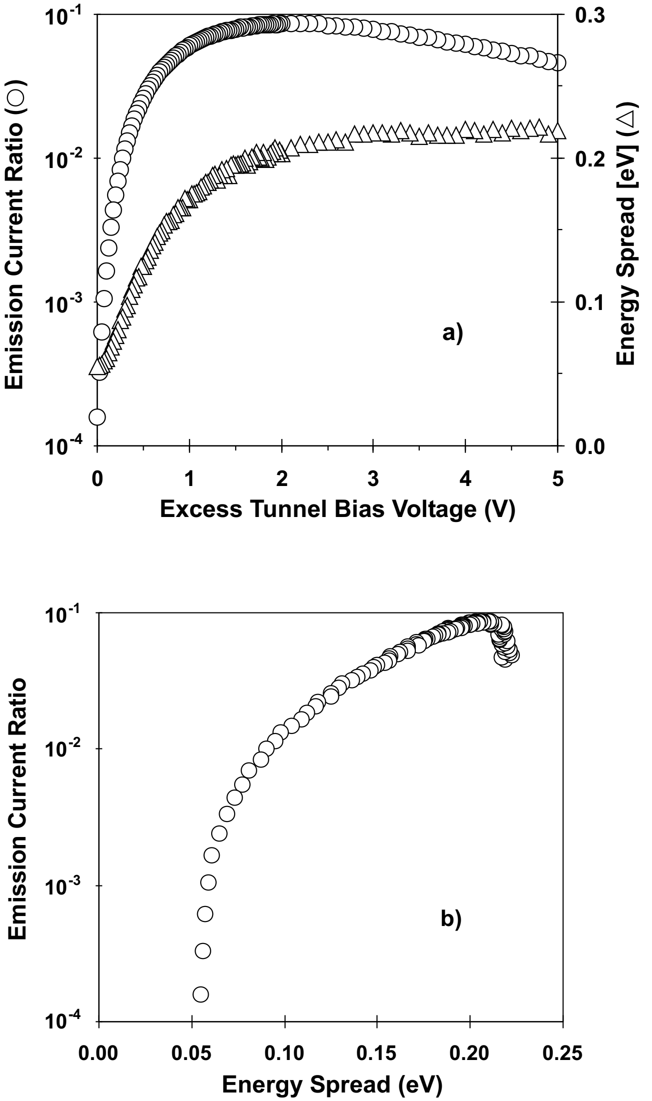

Figure 4.3: *Results of the Monte Carlo calculations by van Bakel. The parameters are* $\Delta\epsilon = 0.2$ *eV,* $kT = 25$ *meV,* $\Delta\alpha_{\mathrm{foil}} = 0.35$ *rad,* $W_{\mathrm{foil}} = 5$ *eV,* $E_{f,\mathrm{foil}} = 5$ *eV and* $L_{\mathrm{mfp}}(E_{f,\mathrm{foil}} + 5\ eV) = 5$ *nm. a) Ratio between the direct emission current and tunnel junction current and the energy spread (full width 50%) versus the excess tunnel bias voltage. Each datapoint is derived from 25000 direct emission events. b) Emission current ratio versus the energy spread.*

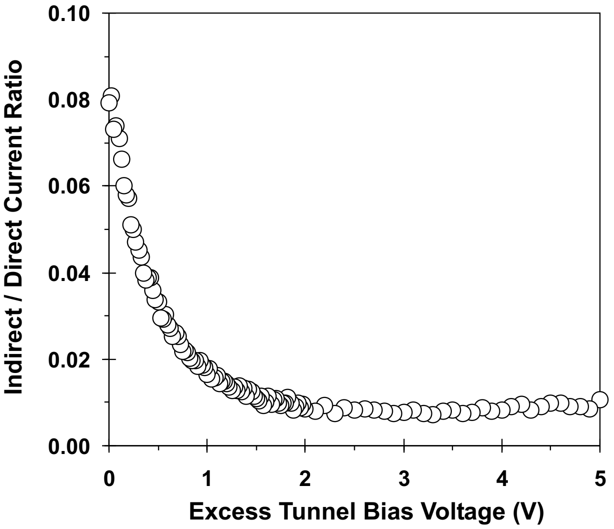

Figure 4.4: *Ratio between the indirect and the direct emission current versus the excess tunnel bias voltage. Parameters: see caption of figure 4.3.*

In figure 4.4 the ratio between the indirect and the direct emission current versus the excess tunnel bias voltage is shown. As discussed earlier, the indirectly emitted electrons may cause an interference effect, which was not included in the model. But at this point, an estimate of the effect can be made. The maximum ratio of indirectly emitted electrons occurs near the vacuum emission threshold and decreases rapidly. In this calculation example, the ratio is only 4.5% at an excess tunnel bias voltage of 0.3 V. For foils with a larger mean free path, the effect will be stronger of course. Due to the internal reflection and the angular distribution, the indirectly emitted electrons are displaced in lateral direction. The current of indirectly emitted electrons will mainly consist of electrons that have made one roundtrip. Then their lateral distribution is widened with a factor 3 compared to the directly emitted electrons and hence the intensity decreases with the same factor. Assuming a Gaussian distribution, the result of this is that the interference effect will be a factor 3 weaker in the centre of the emission spot and stronger at the edges.

The energy filtering of the tunnel junction emitter resembles much that of a retarding foil for which interference effects are negligible (see the dashed line in figure 2.5). The difference is that for the tunnel junction emitter there is only one potential step and for the retarding foil there is a double potential step that does the energy filtering. The latter causes a slower transition from zero to unity transmission. Hence the tunnel junction emitter has a better energy selectivity, provided that interference effects are negligible.

4.3 Conclusion

The calculations have shown that with the tunnel junction emitter a higher brightness and lower energy spread may be obtained than with conventional emitters. When the project was started, the criterion to determine whether this novel emitter is worthwhile to pursue was that it should have a clear advantage over the conventional Schottky emitter. This is the case when a low energy spread can be obtained with a higher brightness than that of a Schottky emitter with an energy filter, or alternatively if the low energy spread can not be obtained, when the brightness is better than that of an unfiltered Schottky emitter. Even if only a comparable brightness and energy spread can be obtained, this emitter may still have the advantages of low voltage operation, fast on/off switching and simple construction. This has led to the following criteria:

$$B_r > 10^6 Am^{-2} sr^{-1} V^{-1} \quad \text{with} \quad \Delta\epsilon < 0.1\text{eV} \quad \text{and} \quad \text{I} > 0.1\text{nA} \tag{4.21}$$

or

$$B_r > 10^7 Am^{-2} sr^{-1} V^{-1} \quad \text{with} \quad \Delta\epsilon < 1\text{eV} \quad \text{and} \quad \text{I} > 1\text{nA}. \tag{4.22}$$

According to the calculations, the first condition can be met abundantly: $B_r = 6.7 \cdot 10^7$ Am^{-2}sr^{-1}V^{-1} at $\Delta\epsilon = 0.1$ eV and I = 0.1 nA. Thus an experimental elaboration is justified. The maximum possible current according to the calculations is 0.9 nA, just below the 1 nA of the second condition. However at this current a reduced brightness of $B_r = 6 \cdot 10^8$ Am^{-2}sr^{-1}V^{-1} with an energy spread of $\Delta\epsilon = 0.2$ eV is obtained.

Chapter 5

Experiments with the Tunnel Junction Emitter

This chapter will deal with the following topics: a pilot experiment to demonstrate the principle of operation of the tunnel junction emitter, a discussion of the experimental results and the stability of the emitter, a method to fabricate the tunnel junction emitter in a solid state form and finally some recommendations for the further development of this type of emitter.

5.1 Pilot experiment in an UHV-STM

In order to demonstrate the principle of operation of the tunnel junction emitter and to study its properties, a set-up has been built with a Scanning Tunnelling Microscope (STM) in Ultra High Vacuum (UHV). A sample containing ultra-thin free-standing foils is put in the STM and a current collector behind this sample measures the emitted current. The advantage of such a set-up for this pilot experiment is that the gap between tip and foil can be varied. Thus, the tunnel junction can be operated at different tunnel currents. During spectroscopic measurements, in which the tunnel bias voltage is swept over a preset range, the STM can be set in either constant current or constant height mode. Furthermore measurements can easily be done on different spots on the sample that contains the foils. The fabrication of the samples is discussed in chapter 3.

5.1.1 Set-up

Overview

A schematic sketch of the set-up is given in figure 5.1. The STM is a Tops II from WA Technology / Oxford Instruments. An important consideration that led to the choice for this STM is that it required only a simple modification to have open space behind the sample. This is necessary to let the emitted electrons escape and be collected on the micro channel plate (MCP). The electronics of this STM allow two channels to be

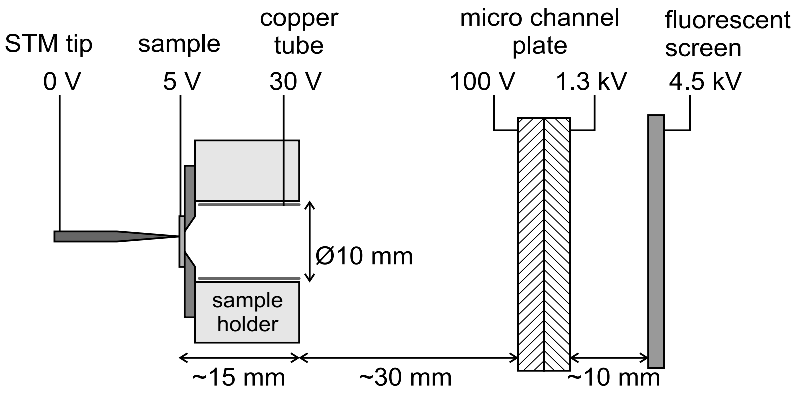

Figure 5.1: *Schematic sketch of the set-up for the pilot experiment (not to scale). Typical values for the voltages and distances are indicated in the figure.*

read in simultaneously during spectroscopic measurements: the tunnel current and the emitted current. (Note: the standard software of this instrument does not allow to make use of this feature, a modified version has been obtained to overcome this obstacle).

Photos of the STM are shown in figure 5.2. Figure 5.3 shows a photo of the complete set-up.

Vacuum system

The vacuum system is sketched in figure 5.4. A load lock system is used in order to exchange samples and tips without venting the complete system. During normal operation the valve between the load lock system and the STM chamber is closed. The load lock system is opened from the front to bring in sample holders and tips. They are put on a holder on a rail, that can be moved forth and back with a magnet after the load lock system is closed. The membrane roughing pump and the turbo molecular pump evacuate this chamber to a pressure of about $5 \cdot 10^{-7}$ mbar. The valve between the ion getter pumps and the STM is closed, the valve between the STM and the load lock system is opened and tip and sample can be put in the STM with the manipulator from the right. This manipulator is also moved with a magnet on the outside. During this operation, the micro channel plate is moved up because otherwise it would block the way. After the valve between the STM and the load lock system is closed and the valve between the ion getter pumps and the STM is opened again, the ion getter pumps reduce the pressure near the STM to about $3 \cdot 10^{-9}$ mbar. With the titanium sublimation pump, the pressure can be reduced further to approximately $5 \cdot 10^{-10}$ mbar. It is possible to bake out the whole system or the load lock system alone to a temperature of approximately 110 °C. A bake out is only performed after the system has been vented for a long period of time.

The membrane roughing pump and the turbo molecular pump cause mechanical

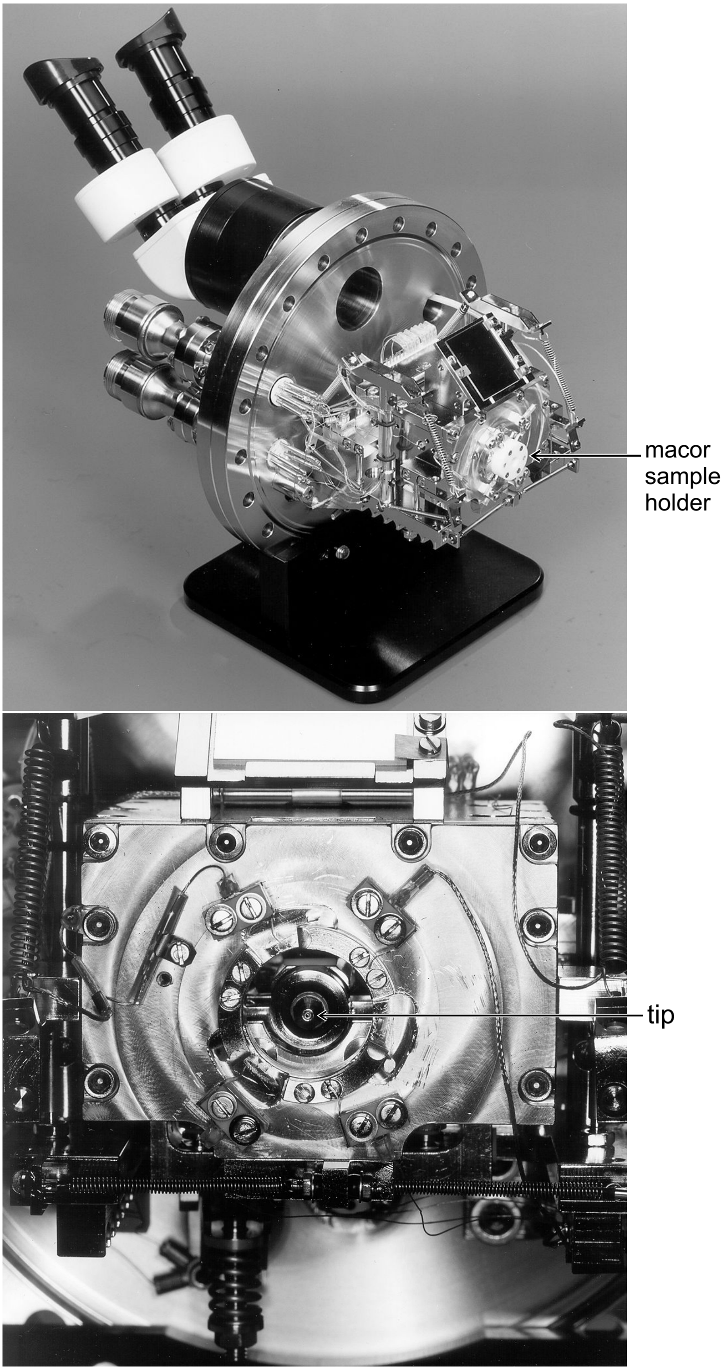

Figure 5.2: *Above: flange with the Tops II STM. The small white tube is a macor sample holder. Below: rear side of the STM with the sample holder removed, such that the tip can be seen.*

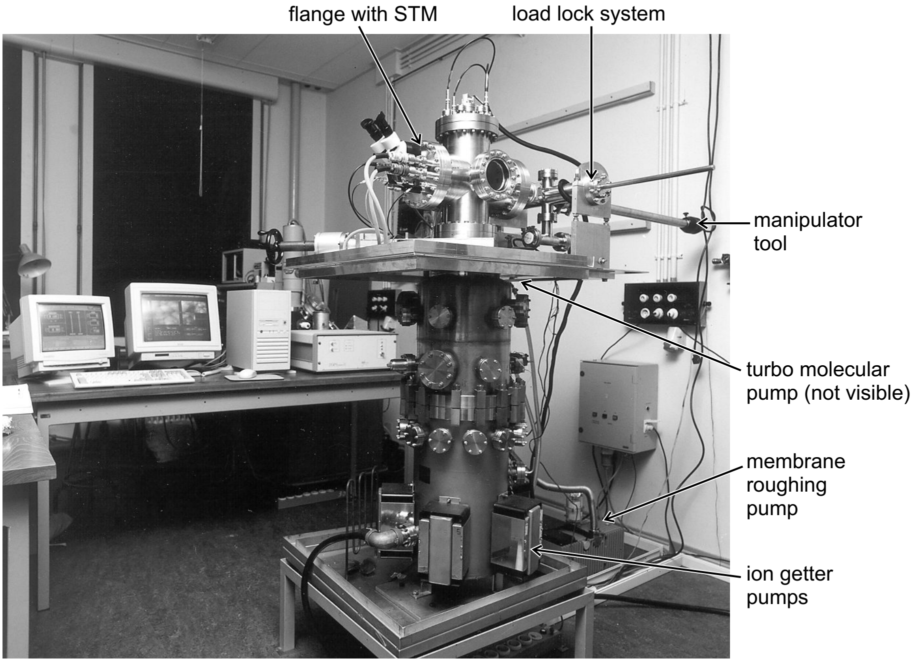

Figure 5.3: *Photo of the complete set-up.*

vibrations that are not desired during STM measurements and must be switched off. Before switching off, the valve above the turbo molecular pump is closed, thus isolating the load lock system. Due to outgassing, the pressure will rise in this chamber, but it is not exposed to air and thus easier to evacuate again, without the need to bake out.

In the ion getter pumps, secondary electrons are generated. Although the ion getter pumps are situated near the bottom of the kettle below the STM chamber, these secondary electrons can reach the micro channel plate. The associated current is of the same order as the emission current that is to be measured. To avoid this disturbance, the ion getter pumps are switched off during emission measurements. The emission measurements can be performed in maximal half an hour. In this time, the pressure near the STM may rise to maximal 10^{-8} mbar.

An inlet for neon gas was added to the vacuum system, because it was desired to sputter tips in situ with neon. The neon is contained in a high pressure bottle with a reduction valve that reduces the pressure to approximately 1 bar. The outlet of this reduction valve is connected to a needle valve, which allows the controlled inlet of neon. This needle valve is mounted on the flange on top, on which also the micro channel plate is mounted. During neon inlet, the valve between the STM and the ion getter pumps is closed and the valve between the STM and the load lock system is opened, such that the system is evacuated with the turbo molecular pump.

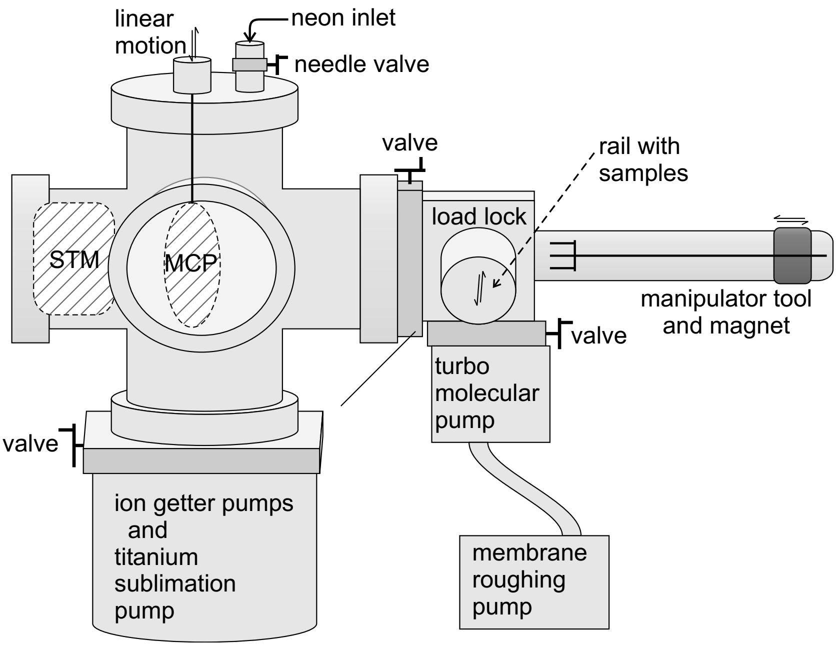

Figure 5.4: *Schematic sketch of the vacuum system.*

Tip fabrication

Sharp tungsten tips are produced with electrochemical wet etching. The base material is polycrystalline tungsten wire, Ø0.16 mm, cut to pieces of approximately 3 cm length. The wire is cleaned in acetone and in alcohol in an ultrasonic bath. Then the wire is pre-etched in a 2 molar KOH solution for several seconds, with the wire biased +5 V with respect to the counter electrode in the solution. A smooth and clean wire surface is obtained. Now, the wire end is put into a 2 molar NaOH solution for approximately 5 mm. As the wire end may contain cracks originating from the cutting, it is etched away completely. During etching in NaOH, the wire is biased +8 V with respect to the counter electrode. The new wire end is put into the NaOH solution for approximately 3 mm and etched again. When the lower wire end drops off, a sharp tip is created at the new wire end and the etch current will drop. When this current drop is observed, the power supply is switched off automatically, to prevent etching of the just created sharp tip. The tip is frequently replaced, because it may become blunt or damaged.

The measurements that will be presented in section 5.1.2 were done with tips prepared in this manner, without any extra treatment. Later, the possibility was added to heat and sputter the tip before it is put in the STM. This serves to remove oxides from the surface and to sharpen the tip. To perform this treatment, the tip is put on a holder near the fluorescent screen, that can be put on the same high potential as the screen. The valve between the STM and the ion getter pumps is kept closed and the system is maintained vacuum with the turbo molecular pump. First the tip is heated with an electron bombardment. The electrons are emitted from a thermionic filament, that is positioned a few millimeters aside the tip. The tip is put on a positive voltage of approximately 1.5 kV to accelerate the electrons towards the tip. Most electrons may hit the shanks of the tip instead of the apex. Through heat conduction, the heat will still reach the apex and since it can not escape through the vacuum, the apex becomes hot. The tip is bombarded with an electron current of approximately 10 μA for approximately 5 minutes. This heating will remove oxides and contamination from the tip, but it may also cause the tip to become blunt.

With sputtering, the tip is sharpened again. Neon is let in to a pressure of approximately 10^{-4} mbar. A negative voltage is applied to the tip with a counter electrode on ground potential placed about 1 cm opposite the tip, such that electrons are field emitted from the tip. Neon atoms are ionized by collisions with these electrons. The positive neon ions are attracted to the tip and do the sputtering. At the start of the sputtering process, the tip is put on a voltage of about -1 to -1.5 kV, such that the field emission current is 5 - 10 μA. The high voltage supply for the tip is operated in constant current mode. As the tip sharpens, the voltage will decrease. Usually, the voltage reaches a value between 450 and 800 V and does not decrease further from then on, meaning that the tip does not become sharper any more. A good description of the sputtering of polycrystalline tungsten tips is given by De Raad, Koenraad and Wolter [50]. These authors were able to obtain somewhat better results. They report that at the end of the sputtering process, a fast drop of the sputter voltage of the order of 50 V occurs, indicating a so-called Schiller-decapitation [54]. Their tips have an estimated radius of 8 - 15 nm. For demonstrating the principle of the tunnel junction emitter, such a very small tip radius is not an absolute requirement.

samples

A few different types of samples are used: commercially obtained gold foils on a grid and self manufactured chromium and platinum foils. The gold foils are polycrystalline and have a thickness of 11 nm, according to specifications. They are mounted on a square mesh grid, the grid bars have a width of 21 μm, the square open windows they enclose are 43 μm in size. The chromium foils have a thickness varying from 5 to 8 nm. Their lateral size ranges from $(0.6\ \mu\mathrm{m})^2$ to $(3\ \mu\mathrm{m})^2$ square. Each sample contains multiple foils of different lateral sizes, see for example figure 3.3. A complete description of these samples and the fabrication process is given in chapter 3. The platinum foils are fabricated in a similar manner as these chromium foils. The reason that chromium, a non noble metal, has been used is that it was easier to incorporate in the fabrication process and that the growth of thin, uniform and closed layers was achieved better for chromium than for platinum.

Measurement method

The sample is mounted on a hollow macor sample holder. A copper tube is put inside the sample holder to prevent charging. The voltages on this copper tube and the entrance of the micro channel plate are such, that emitted electrons are accelerated towards the micro channel plate. A ray tracing calculation has confirmed that with the voltages as indicated in figure 5.1, the emitted electrons can reach the micro channel plate. The amplification of the micro channel plate is about 10^6. The current on the fluorescent screen, which is at high voltage, is measured with a current meter which has an optocoupler to separate the high voltage from ground potential. The dynamic range of this meter is about 3 kHz and the smallest measurable emission current about 5 fA. The advantageous properties of this measurement method are the amplification of the micro channel plate and the fact that an image on the fluorescent screen is obtained which must truly originate from vacuum emitted electrons and can not be due to a leakage current.

5.1.2 Measurements

The first successful emission experiments have been done on the 11 nm thick gold foils. Several measurements have shown emission starting at bias voltages in the range of 4 to 6 V, thus confirming the threshold behaviour of the source. The workfunction of gold is 4.3 eV. The threshold variation in the experiments may be caused by adsorbates on the gold surface, which change the barrier. In these measurements, a spot on the fluorescent screen was observed, which is proof that it was a true emission current. A complicating factor in these measurements was that the tunnel current tended to become unstable at bias voltages exceeding about 3 to 4 V. Also, the emission was always pulsed, a continuous emission current could not be established.

Figures 5.5 and 5.6 show typical emission measurements. The tunnel current and the emission current are recorded while the bias voltage is swept from 2 to 7 V. The STM is operated in constant height mode, that is: the feed-back is switched off during the measurement such that the tip stays on a fixed position. Because the current meter as outlined in section 5.1.1 was not yet installed, the emission current is recorded with a photometer that records the light intensity on the fluorescent screen. Both measurements show an emission pulse at approximately 5 V. The tunnel current signal clips at 100 nA because that is the maximum in the range of the tunnel current meter. The power supply can deliver a current of up to 4 mA. In figure 5.5 there is a second pulse in the emission signal at 6.8 V. This pulse is much higher than the first one, but the tunnel current may have been much higher as well. The latter can not be verified in this case because the tunnel current meter had already reached its maximum. The fact that there is still a photometer signal after the voltage has been reduced (figure 5.5) or after the tunnel current has disappeared (figure 5.6) can be attributed to the slow decay time of the measurement equipment.

After the experiment, a DC current meter was connected to the fluorescent screen and an adjustable constant free electron current supplied to the micro channel plate in order to calibrate the photometer signal. Since the photometer was much more sensitive than this current meter, a precise calibration was not possible, only the order of magnitude of the photometer signal could be determined. When the photometer output signal reaches the maximum of its range of about 5 V, the measured current on the screen is 0.3 μA with an uncertainty in the measurement of 0.2 μA. This means that the second pulse in the emission signal in figure 5.5 is equivalent to a current of approximately 0.3 μA on the fluorescent screen and thus an emission current of the order of 0.1 to 1 pA. During the measurement in figure 5.6, the emission signal

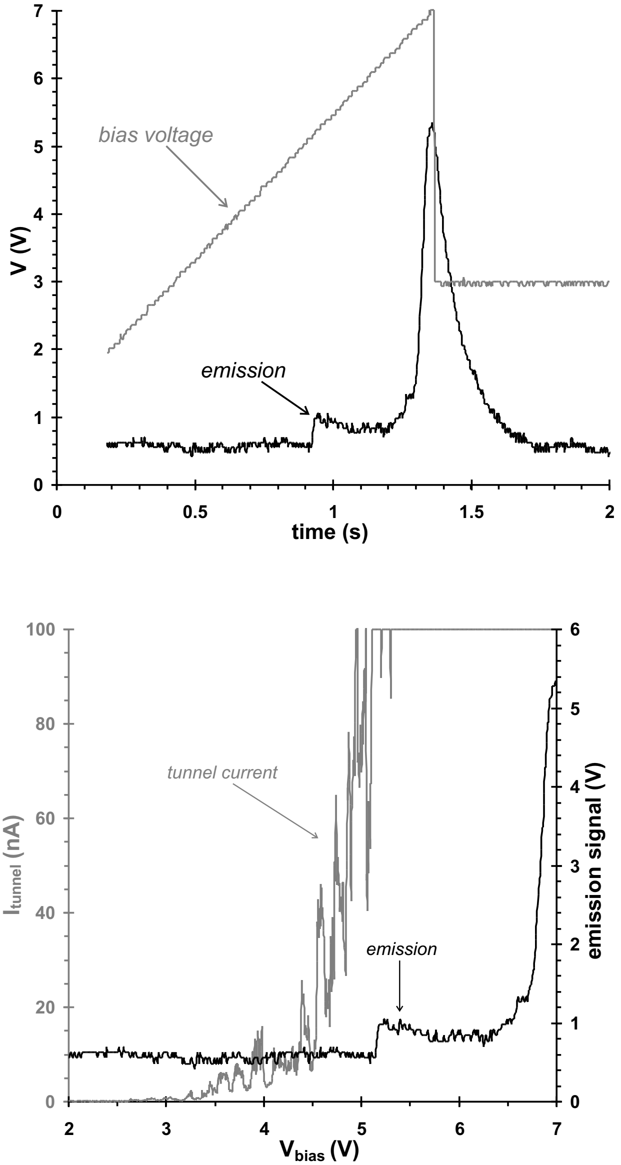

Figure 5.5: *Measurement of the tunnel and emission current during a voltage ramp. The STM is operated in constant height mode. Above: tunnel bias voltage and emission versus time. The emission current is measured by measuring the light intensity on the fluorescent screen. An output signal of 1 V corresponds to an emission current of the order of 0.1 pA, see the text for explanation. Below: tunnel current and emission current versus bias voltage.*

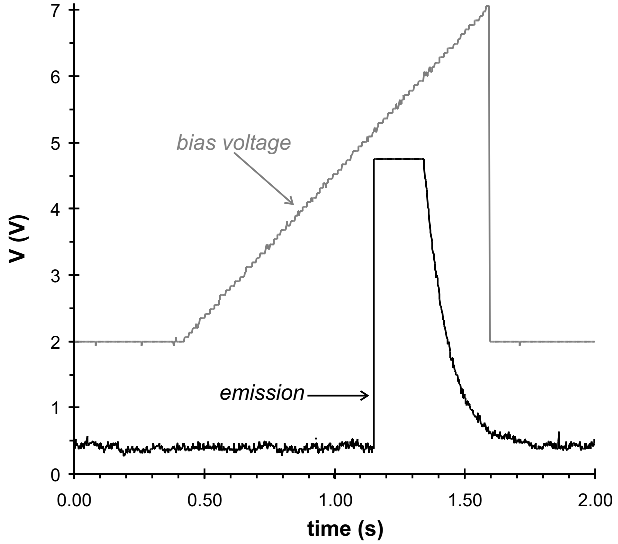

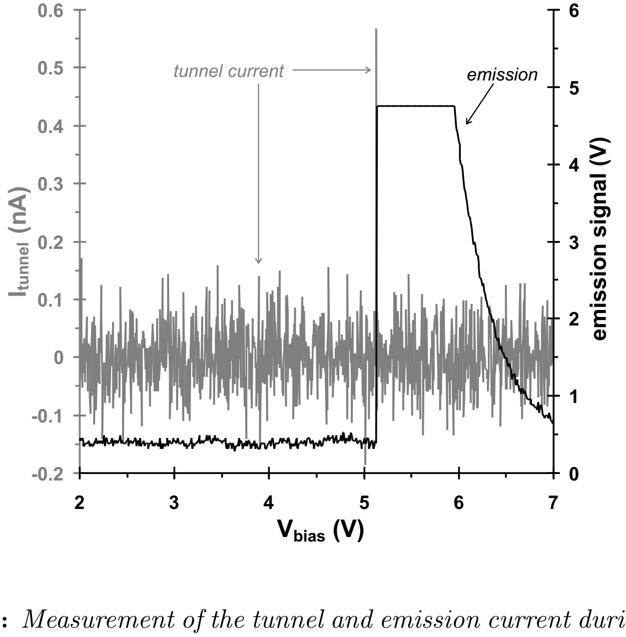

Figure 5.6: *Measurement of the tunnel and emission current during a voltage ramp, similar to the measurement in figure 5.5.*

has exceeded the maximum of the range, indicating an emission current of the order of a pA. The measured tunnel current during this emission pulse was 0.57 nA. This leads to an emission ratio of the order of 10^{-3}. Because of all the uncertainties in the measurement and because of the unstable tunnel contact, this result must be regarded with certain reservation.

Spectroscopic measurements in constant current mode, that is with the feed-back on, have been performed as well. Because the tunnel current tends to become unstable above 3 - 4 V, these measurements can not be regarded as truly constant current. Figure 5.7 shows a typical example. The graph suggests that the gap between tip and foil increases about 30 nm when the bias voltage is swept from 2 to 7 V. During other measurements, similar gap changes have been measured. In order to keep the current constant when the voltage is increased, it is to be expected that the feedback will increase the size of the gap as well. However, this can not account for an increase as large as 30 nm. An explanation can be that the foil is attracted towards the tip during the measurement because the electrostatic attraction between tip and foil increases when the bias voltage increases. This effect will be discussed in section 5.1.3. Note that the graph in fact represents the motion of the tip in the direction perpendicular to the surface. This is identical to the change of the gap size, only as long as the sample itself can not move during the measurement.

Emission experiments on the self manufactured chromium foils show similar results: an unstable tunnel current at higher voltage and when emission is established, it is always pulsed. Very often, these experiments resulted in damage to the foil, as is shown in figures 5.8 and 5.9. Figure 5.8a shows a STM image of a foil before experiments at a high bias voltage. Directly after this image was recorded, an area of 1 μm × 1 μm centered at the foil was scanned at a bias voltage of 6 V, see figure 5.8b. Figure 5.8c is recorded after this experiment, showing the damage to the surface. An identical experiment was performed on a foil on a different sample, which is shown in figure 5.9a. A scan at a bias voltage of 6 V was started on this foil and aborted halfway because the tunnelcurrent became very unstable. Figure 5.9b shows that the bottom part, that had just been scanned at 6 V, is completely ruined.

Subsequent experiments have been focussed on these instability problems. First possible causes as contamination and bad electrical contact have been considered and examined. For the self manufactured chromium foils, it must be checked that there is a good electrical contact to the foils. The layer that eventually forms the free-standing foil was deposited from the backside, while the rest of the sample was covered with chromium from the front side (see chapter 3. These layers may not make contact with each other. Therefore a contact between the front and back side is made with silverpaint at the side of the sample. Since normal STM images can be made on the foils, it can be concluded that this was sufficient. Because samples and tips are exposed to air, before they are put in the STM, a layer of oxide or contamination can be formed on the surface, that may disturb the tunnelling. The tip is cleaned from oxides and other contamination by in situ heating and subsequent sputtering to sharpen the tip again, as described in section 5.1.1. The chromium foils are probably oxidised after exposure to air. Since the whole surface of these samples consists of a chromium layer and normal STM images can be made on this surface, the chromium oxide layer that is formed must be either very thin or it must be conducting as well.

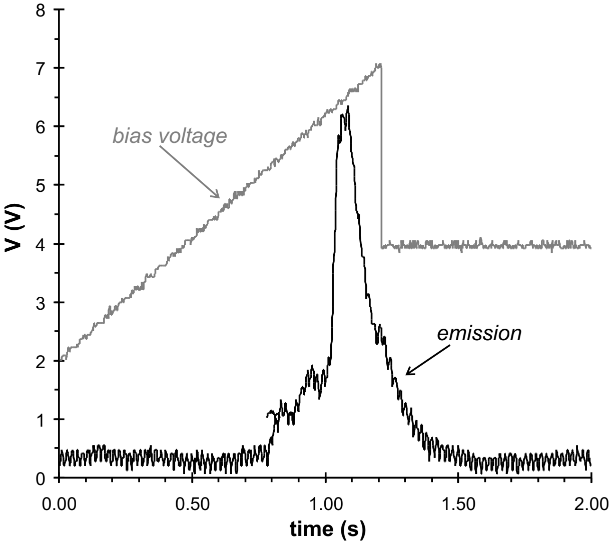

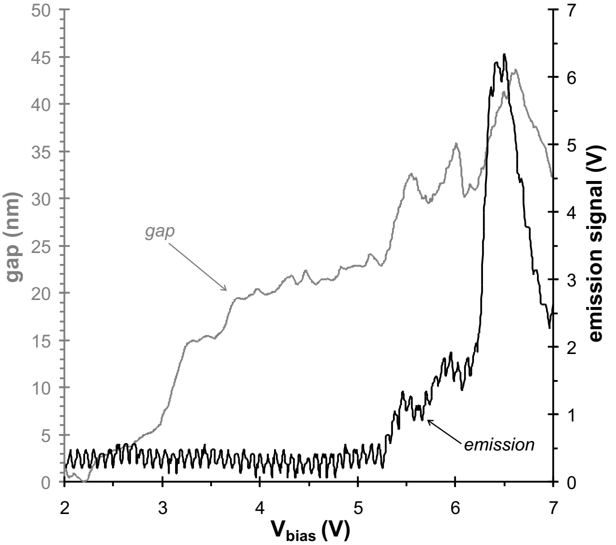

Figure 5.7: *Measurement of the tunnelling gap and the emission current during a voltage ramp. The STM is operated in constant current mode, with the tunnel current set to 0.1 nA. Above: tunnel bias voltage and emission versus time. Below: tunnelling gap and emission versus bias voltage. The emission current measurement is identical to the method in figures 5.5 and 5.6*

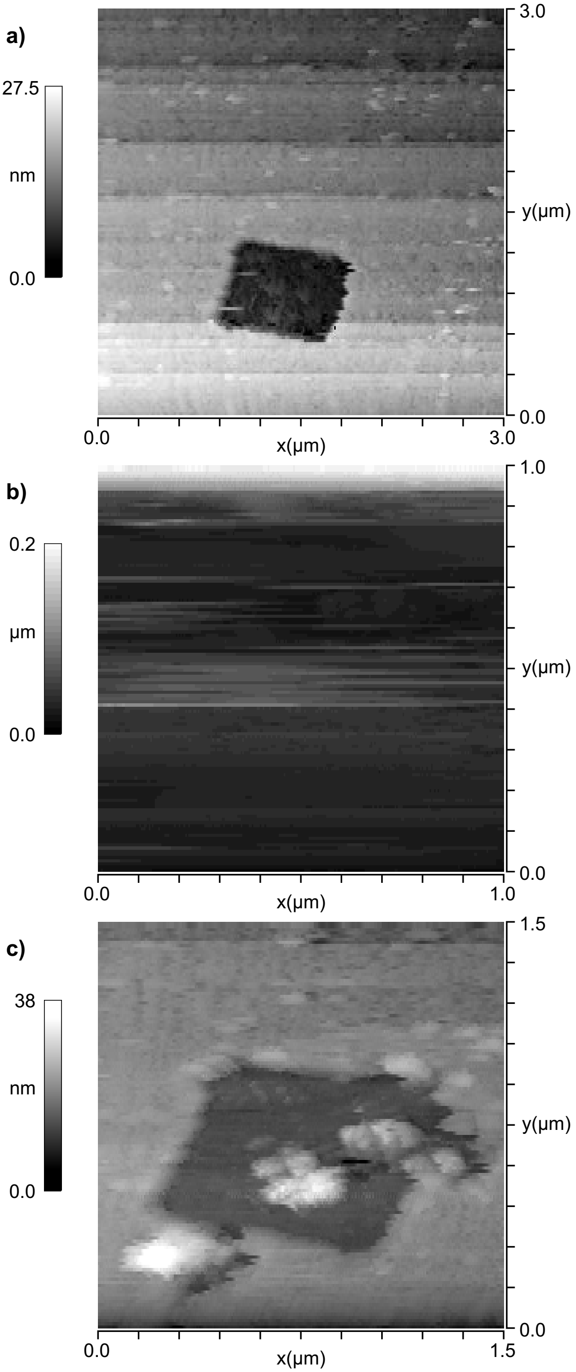

Figure 5.8: *STM images of a chromium foil before (a), during (b) and after (c) experimenting at a bias voltage of 6 V. The imaging parameters are: a:* $V_{\text{bias}} = 1.5$ *V,* $I_{\text{tunnel}} = 0.1$ *nA; b:* $V_{\text{bias}} = 6.0$ *V,* $I_{\text{tunnel}} = 1.0$ *nA; c:* $V_{\text{bias}} = 1.5$ *V,* $I_{\text{tunnel}} = 0.1$ *nA.*

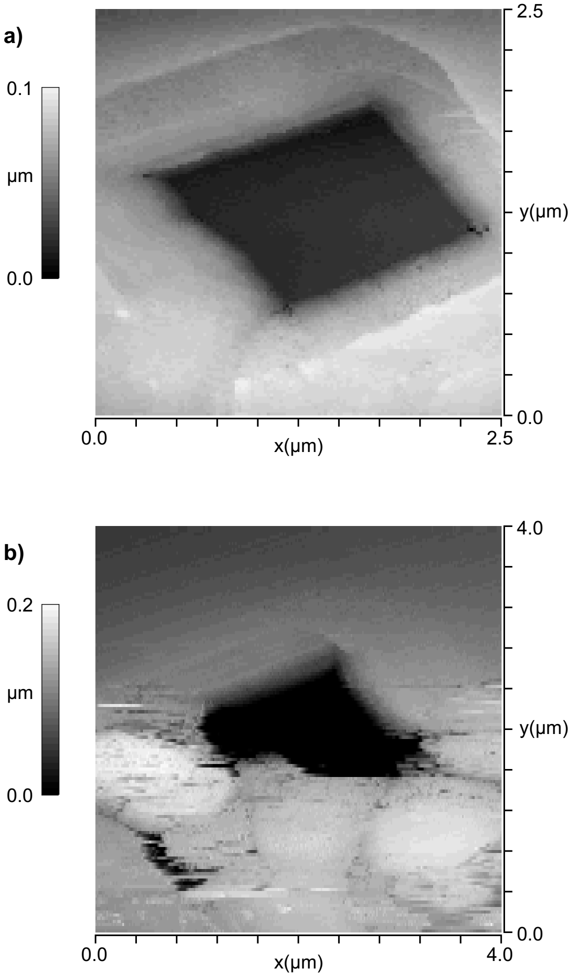

Figure 5.9: *STM images of a chromium foil before (a) and after (b) experimenting at a bias voltage of 6 V. The parameters for both images are:* $V_{\text{bias}} = 1.5$ *V,* $I_{\text{tunnel}} = 0.1$ *nA.*

As an extra check, the experiments have been repeated with gold and chromium foils on which a 2 nm platinum overlayer was deposited with E-gun evaporation, thus excluding surface oxidation. To minimise contamination, the samples were put in the vacuum system shortly after this deposition. Also platinum foils have been produced in a similar manner as the chromium foils (see chapter 3). All these measures did not result in improvements.

In Scanning Tunnelling Microscopy usually voltages below 1 V are used, a bias voltage of around 5 V is extraordinary. Several authors have reported that they were able to modify the surface by applying voltage pulses exceeding about 3 - 4 V (for some examples, see references [14, 33, 37, 62]). Many of these studies have not been done in UHV conditions and the authors relate the surface modification to the presence of water. Weierstall [62] was able to obtain surface modifications under UHV conditions by applying 5 V pulses, however this did not happen consistently, only in about 10 - 20 % of the cases. Hence it is relevant to check whether a stable tunnel contact at this voltage can be established on a 'normal' substrate, different than a free-standing foil. On a sample containing chromium foils, the tip is put on a rigid part of this sample, on the so-called search pattern. For several seconds the bias voltage is set to 5.5 V and the preset tunnel current to 0.5 nA. A stable tunnel contact is observed. STM images made before and after this test show that the surface is not damaged. Repeated experiments show that sometimes it may be more difficult to obtain a stable tunnel contact and surface damage may occur. Nevertheless the test shows a significant difference with the experiments on the free-standing foils. This can be attributed to the electrostatic attraction between tip and foil and the mechanical flexibility of the foil, which will be discussed in the next section.

5.1.3 Tip-foil attraction

When the bias voltage between tip and foil is increased to 5 V, the electrostatic attraction force will increase as well. This will cause the foil to bend towards the tip, till either the tensile force becomes in balance with the electrostatic force, or the foil touches the tip. When tip and foil make electrical contact, the electrostatic force disappears and the foil is released. Then the potential difference between tip and foil will be restored, the foil is attracted again and the whole process will repeat itself. When such a repetitive process occurs, an unstable tunnel current will be observed and a pulsed emission, till the foil or the tip are damaged so much that the emitter does not function any more.

Using a simple model, an estimate of the forces on the foil and the deflection will be obtained, to analyse whether the process described above is likely to occur. The set-up is sketched in figure 5.10. For simplicity a circular foil is assumed, radius R_{foil} and thickness t. The tip is positioned at a distance h from the sample in front of the centre of the foil. Due to the attractive electrostatic force, the foil bends. The maximum deflection, denoted by w, occurs in the centre. As a result, the gap between tip and foil becomes $s = h - w$.

The tip is modelled by a sphere with radius R_{tip}. This is allowed when the tip sample distance is small compared to the lateral dimension of the tip, that is: $h << R_{\text{tip}}$. According to Belaidi [8], the electrostatic force for this situation can be

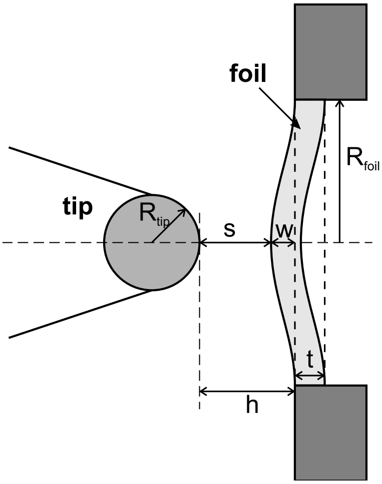

Figure 5.10: *Sketch of the tip in front of a circular foil. See the text for an explanation of the symbols.*

approximated by:

$$F_{\text{electrostatic}} \approx -\pi\epsilon_0 V_{\text{bias}}^2 \frac{R_{\text{tip}}}{s}. \tag{5.1}$$

The bending of the foil causes a tensile force in the opposite direction. For small deflections, the bending is elastic and the tensile force is [31]:

$$F_{\text{tensile}} = \frac{16\pi D_{fr}(h-s)}{R_{\text{foil}}^2}. \tag{5.2}$$

D_{fr} is the flexural rigidity, defined as:

$$D_{fr} \equiv \frac{E_{\text{young}} t^3}{12(1-\nu^2)}, \tag{5.3}$$

with E_{young} the Young's modulus and ν the Poisson ratio.

As an illustration, the electrostatic and the tensile force are plotted in figure 5.11 for a few typical configurations of the tip and the foil. The tip-sample distance must be chosen such that at 5 V, the required field at the tip for tunnelling is obtained, which is approximately 3 V/nm. For low bias voltages, the tip sample distance is much smaller than the tip radius and the field is simply V_{bias}/s. This can be verified by the observation that at constant current, the gap size increases linear with the voltage. At higher voltages, the distance will be larger and the effect of field enhancement at the tip may have to be taken into account. Mesa, Sáenz and García have done calculations for this so-called near field emission regime [43]. Their calculations show that for a tip with radius 50 nm and in the range of 0 to 5 V, the tip sample distance versus applied voltage at constant current is still almost linear. This means that field enhancement at the tip is negligible. For a tip radius of 5 nm, the field enhancement

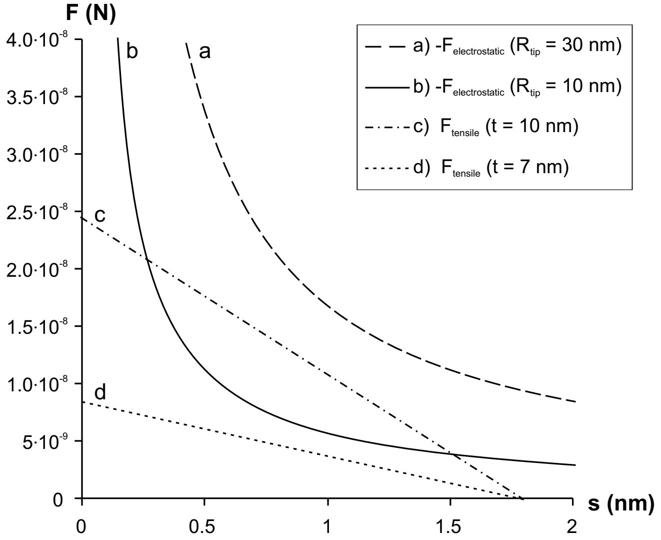

Figure 5.11: *Electrostatic and tensile force versus the tip-foil gap s for a few different configurations. The parameters are:* $E_{\text{young}} = 2.79 \cdot 10^{11} Pa, \nu = 0.21$ *(chromium) ,* $R_{\text{foil}} = 0.3 \mu m, V_{\text{bias}} = 4.5$ *V , tip-sample distance* $h = 1.8$ *nm (note: the foils deflection is* $w = h - s$*; the field at the tip is* V_{bias}/s *and must be around 3 V/nm for tunnelling). a)* $-F_{\text{electrostatic}}$ *for a tip radius* $R_{\text{tip}} = 30$ *nm; b)* $-F_{\text{electrostatic}}$ *for* $R_{\text{tip}} = 10$ *nm; c)* F_{tensile} *for a foil thickness* $t = 10$ *nm; d)* F_{tensile} *for* $t = 7$ *nm.*

effect is only slightly noticeable in the 0 to 5 V range. Therefore it is assumed that the field is V_{bias}/s.

Depending on the parameters, the graphs of F_{tensile} and $-F_{\text{electrostatic}}$ have either 2 or no intersections. No intersections means that the electrostatic force is always larger than the tensile force and the foil will bend till it touches the tip. Lines b) and c) have two intersections. Only the lower right intersection is a stable equilibrium, for a small increase or decrease of the foils deflection, the net force will be directed towards this point.

When interpreting these calculation examples, one should keep in mind the simplifications that were made to obtain these results. Besides the assumptions already mentioned above, the flexural rigidity of the foil was determined assuming bulk properties, though the foil is only a few nm thick. Further refinements of the model could lead to more precise results, but in this case that will not be very useful since the thickness of the foil and the radius of the tip are not known exactly. It is not required either because the approximate results obtained here already show that the process of tip and foil touching each other is likely to occur. When the tip bends towards the foil, the feedback of the STM will of course start to retract the sample because it detects that the tunnel current becomes too large. However the eigenfrequency of the foil is of the order of 10 MHz, which is due to the fact that the foils mass is very small. Thus it is practically not possible for the feedback to retract the sample in time.

There are several options to reduce the foil bending, however all of them have certain disadvantages or limitations. In the calculation example the tip was positioned at the centre of the foil, which is the worst case. The bending will be less if the tip is close to the edge of the foil. For a substantial reduction, the tip must be positioned very close to the edge (less than 100 nm). Such an accurate positioning is a tedious experimental job because of the hysteresis of the STM piezo stage and drift effects. Reducing the lateral size of the foil has the same effect, but that requires new samples with a modified design to be fabricated. Increasing the foils thickness is not very attractive, unless materials are found which have a mean free path that is considerably larger than 5 nm. A lower workfunction at the foils exit surface will have some beneficial effect, since this allows the emitter to be operated at a lower voltage. Lowering the voltage involves decreasing the gap size as well, in order to keep the tunnel current constant. Assuming that in constant current mode the field at the tip, thus V_{bias}/s must be kept constant, it can be seen that the electrostatic force decreases linear with decreasing voltage. Also a small tip radius is beneficial, even if the current is kept constant which means that the electric field must be increased for a tip with a smaller tunnelling area. The tunnel current is exponentially dependent on the electric field so the reduction of the electrostatic force due to the smaller tip radius will only partly be cancelled by the increased electric field strength. However it is experimentally difficult to obtain a tip radius smaller than 10 nm and to keep the tip that sharp during experiments. The etched tungsten tips typically had a radius of 50 - 100 nm. Since all of these measures will cause only a limited improvement, the best way to eliminate the instability problem is to fix the gap between tip and foil. This can be achieved by fabricating the tunnel junction emitter completely in solid state, which is discussed in the next section.

5.2 Simple fabrication method in solid state

The set-up with a complete STM seemed the most favourable for carrying out the pilot experiment. Apart from the instability problems, such a set-up is not convenient for use in a practical application. Therefore, in this section a method is described to fabricate a tunnel junction emitter as a solid state device, in which an oxide layer serves as gap between tip and foil. Such a device is similar to a conventional Metal-Oxide-Metal (MOM) cathode [1, 40, 56, 66]. The difference is that for this device, the lateral size of the tunnel contact is very small. In figure 5.12, the typical energy scheme for a device consisting of a tungsten tip, a WO_3 layer and a gold foil is given. The barrier for the transition from metal tip to oxide will be lower than for a metal - vacuum transition and additional scattering may occur in the part of the oxide where the potential is lower than the electron energy. It will be shown that tunnel junction emitters in the form of a solid state device can be fabricated with a relative simple method and a few measurements with these devices are presented.

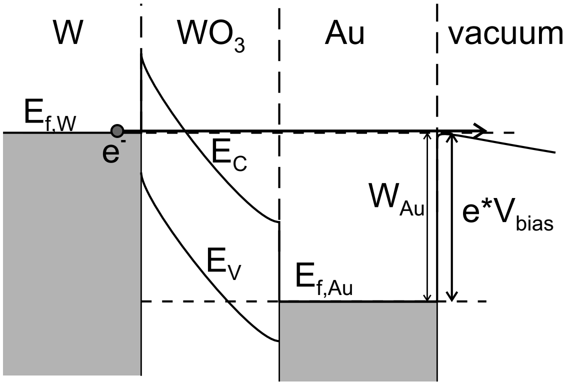

Figure 5.12: *Typical energy diagram for a W-*WO_3*-Au emitter.* $E_{f,W}$ *and* $E_{f,Au}$ *are the respective Fermi levels of the tungsten tip and the gold foil.* W_{Au} *is the workfunction of the gold foil.* V_{bias} *is the tunnel bias voltage.* E_C *and* E_V *are the levels of respectively the conduction band and the valence band of the* WO_3*. The band gap of* WO_3 *is between 2.5 and 3.1 eV [48].*

5.2.1 Fabrication method

In short, the fabrication is as follows. A glass plate is covered with a layer of epoxy resin. An oxidised Tungsten tip is put in the resin, against the glass plate. After hardening of the resin, the glass plate is removed and a thin metal foil is deposited (figure 5.13). All steps involved will be presented in detail below.

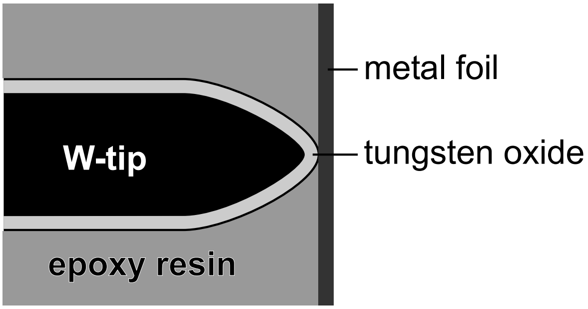

Figure 5.13: *Cross section sketch of the device.*

Sharp tungsten tips are fabricated from pieces of tungsten wire with electrochemical wet etching. For a description of this process, see section 5.1.1. A tungsten oxide layer is formed on the tip by means of anodisation in water. The wire is put in demineralised water. For about 1 minute a positive voltage is put on the wire, with respect to the counter electrode in the water. After sufficiently long anodisation time (which is the case here), the thickness of the oxide layer that is created does not increase any more. A voltage of 10 V was applied which resulted in an oxide layer thickness of approximately 20 nm (see figure 5.14). Because the tip is anodised at room temperature, it is expected that the oxide layer is WO_3 [46].

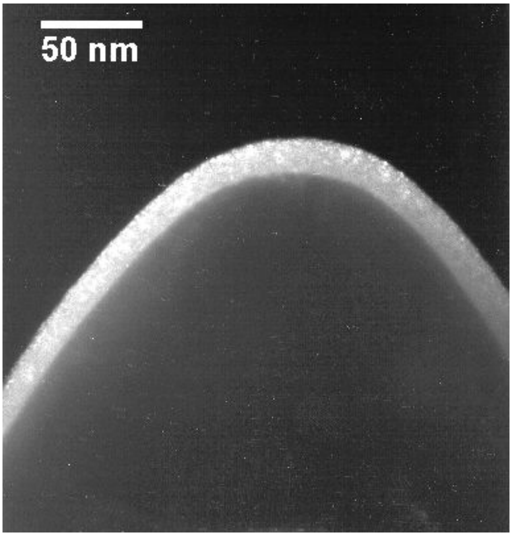

Figure 5.14: *Dark-field Transmission Electron Microscopy image of a tungsten tip after oxidation.*

The most delicate step is to put the tip in contact with a substrate, in an epoxy resin, as the tip may bend very easily. As the substrate, a microscope glass is taken, because its surface is relatively flat and easy to clean. A loop is made in the tungsten wire, which serves as pull relief after the resin has hardened. The tip is connected to a leafspring, in order to put it against the substrate with a low force (see figure 5.15). The leafspring is a tungsten wire, length approximately 10 cm, Ø0.16 mm. The spring constant is approximately 0.05 N/m. First the epoxy resin is put on the substrate. Then the tip is put in the resin and against the substrate. Whether the tip is in contact with the substrate is detected optically, which means that the deflection of the leafspring-end is about 1 mm. The applied force is therefore of the order of 10^{-4} N. This may seem small, however if the area of contact is of the order of (100 nm)2, the pressure is of the order of 10^5 bar. The question is what happens to the tungsten tip and the tungsten oxide layer under such a high pressure. Figure 5.16 shows a Transmission Electron Microscopy image of an oxidised tungsten tip after the above described operation. It can be seen that the oxide at the apex has been pushed away and that the remaining oxide thickness is only about a fifth of the original thickness. Very important is the observation that the shape of the tungsten tip seems not to have changed. This can be attributed to the fact that the hardness of the tungsten tip exceeds that of the glass substrate. The epoxy resin hardens within a few hours. After 24 hours, the hardening is complete. Because the resin sticks to the glass substrate quite well, it takes some effort to remove it. First the sample is put in alcohol in an ultrasonic bath. Then a scalpel knife is moved into the glass - resin interface and the substrate can be lifted off. The final step is the deposition of a metal layer. A 20 nm thick gold layer is deposited on the resin surface by sputtering.

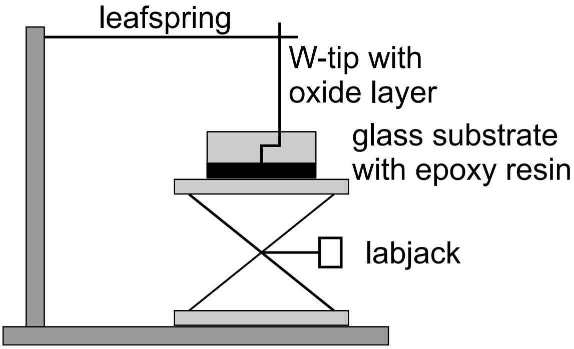

Figure 5.15: *Sketch of the set-up used to put the tip against the substrate.*

5.2.2 Experimental set-up

Several devices that show a tunnel current and emission into vacuum have been produced. For testing of these devices, the same equipment as for the pilot experiment has been used. The set-up in ultra high vacuum is sketched in figure 5.17. The device is connected to the electronics of the STM, in order to measure simultaneously the tunnel current and the emission current versus the bias voltage. The tunnel current is measured at the tip. The tip is at ground potential, the metal foil on a positive bias voltage. The emitted electrons are accelerated towards the micro channel plate (MCP), which has an amplification of approximately 10^6. The current emitted from the MCP is accelerated to a fluorescent screen. The emission current is determined by measuring the current on the screen. During the measurements, the pressure in the system was about 10^{-8} mbar.

5.2.3 Results

Figure 5.18 shows a measurement of the tunnel current and the emission current versus the bias voltage between tip and foil. It can be seen that the emission starts at 4.3 V, which is in agreement with the fact that the workfunction of gold is 4.3 eV. Several measurements have been done on different devices, which show that the threshold for emission is between 4 and 5 V. The variation in the threshold voltage may be caused by adsorbates on the gold surface which may locally change the barrier. During the measurements, a spot on the fluorescent screen was observed, which confirms that the measured current is a true emission current. For this measurement, above 3 V the tunnel current became so large that it exceeded the maximum range of 100 nA

Figure 5.16: *Dark-field Transmission Electron Microscopy image of an oxidised tungsten tip after contact with the substrate.*

of the current meter. At 6.5 V a destruction of the device must have occurred. Later measurements on this device did not show a tunnel or emission current any more.

In order to determine the ratio between emission and tunnel current at a constant voltage, pulses of 5 V during 20 ms were applied to a device (a different device than that of the previous measurement), see figure 5.19. From this measurement, it can be determined that the ratio is of the order of 10^{-5}. This is the highest ratio that has been measured for these devices. In section 4.2.4 this ratio was calculated for tunnel junction emitters having a 5 nm thick metal foil, a workfunction of 5 eV and a vacuum gap instead of an oxide. According to these calculations, the ratio is about 0.01 at 0.5 V above threshold. The very small ratio measured can only partially be attributed to the larger thickness of the gold foil and to some additional scattering in the oxide layer. For the remaining discrepancy we have no definite explanation yet. But the calculations also show that the ratio changes over orders of magnitude, from 10^{-3} to 10^{-1}, for the bias voltage ranging from 0.1 to 1.0 V above threshold. The emission currents measured should be compared to those measured by Meepagala and Baykul [41]. In a set-up with a STM-tip in tunnelling contact with a free-standing gold film of 60 nm thickness, they measured emission of a few electrons per second. The emission currents we have now measured are orders of magnitude higher, ranging from tens of fA's to tens of pA's.

All devices show rather unstable tunnel and emission currents. This is already visible in figures 5.18 and 5.19. To study the time behaviour of the devices, consecutive

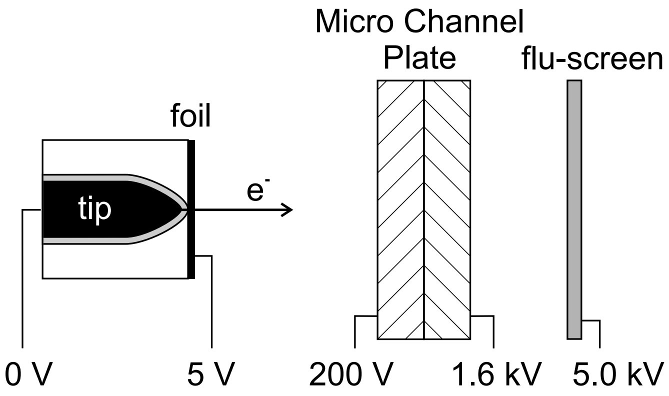

Figure 5.17: *Sketch of the set-up used to measure the tunnel and emission current characteristics of the devices. The typical voltages applied are indicated in the figure.*

IV-characteristics are recorded, see figures 5.20 and 5.21. From the third to the fourth measurement, there is a considerable increase in the tunnel current. After the fourth measurement, the tunnel current increases slightly till it finally reaches a constant level. This behaviour has been observed for several devices. It resembles stress induced leakage current as observed frequently in MOSFET gate oxides [57], where electrons are injected into the oxide by Fowler Nordheim tunnelling. For some devices, the tunnel current eventually drops to zero after prolonged measurements. It seems likely that at this point the gold foil is damaged (this may also apply to the current drop in figure 5.18). After deposition of an extra gold layer on one of these devices, electrical contact was indeed restored.

Whereas the tunnel current increases in time, the emission current doesn't. Most devices show the best emission properties during the first or the first few measurements, after which the emission current decreases, although the tunnel current has increased. Also, the emission current starts at higher voltages than the original threshold. Finally, the emission current drops to zero. An explanation for this behaviour can not yet be given, but it may be related to damage of the gold foil.

About one third of the devices produced with this method show no tunnel contact at all or an ordinary ohmic contact. This can be attributed to the fact that the procedure to put the tip against the substrate is very sensitive to experimental mistakes. From the devices that do show a tunnel contact, about half do not show an emission current. Explanations for this may be a variation in the thickness of the gold foil - causing a larger thickness at the tunnel contact and therefore more scattering - and the possibility of the presence of adsorbates on the gold foil.

5.2.4 Conclusion

It has been shown that tunnel junction emitters in the form of a solid state device can be fabricated with a relatively simple method. The threshold dependence of the

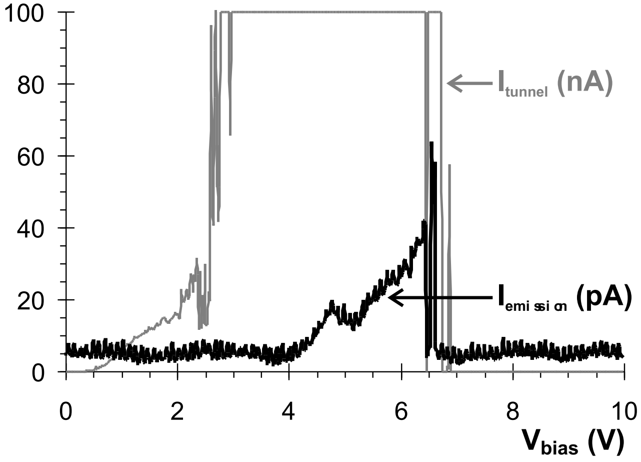

Figure 5.18: *Tunnel and emission current versus bias voltage for a tunnel junction emitter.* I_{tunnel}*: tunnel current through the junction in nA.* I_{emission}*: emission current in pA.* V_{bias}*: bias voltage between tip and foil in V.*

emission current on the applied bias voltage has been clearly demonstrated and is in agreement with the workfunction of the gold foil. The emission currents measured range from tens of fA's to tens of pA's. The best emission to tunnel current ratio measured was 10^{-5}. For consecutive IV-curves on the same device, the tunnel current increases. This must indicate a change in the properties of the oxide layer, which may be caused by scattering of electrons in the oxide. Simultaneously, the emission current decreases for consecutive IV-curves and finally drops to zero. For some devices the tunnel current eventually terminates, indicating that the gold foil has likely been damaged during the measurements.

5.3 Conclusion and recommendations

The experimental work, both on the tunnel junction emitter with a free-standing foil as on the solid state devices, has verified the principle of operation of this emitter. However the stability and the life time are still a major problem. This problem still prevents the measurement of the reduced brightness and energy spread and the use of the emitter in real applications.

For practical use, a solid state device design is the most convenient, so future research on the tunnel junction emitter can best be focussed in this direction. The stability problem of the devices produced for this research probably have their origin in the oxide layer. No efforts have yet been made to optimize this oxide layer. Both the fabrication of the insulating layer and the choice for the type of material are still open for improvement. Scattering of electrons may cause degradation of the oxide layer. This scattering can only occur when the electrons can enter the conduction

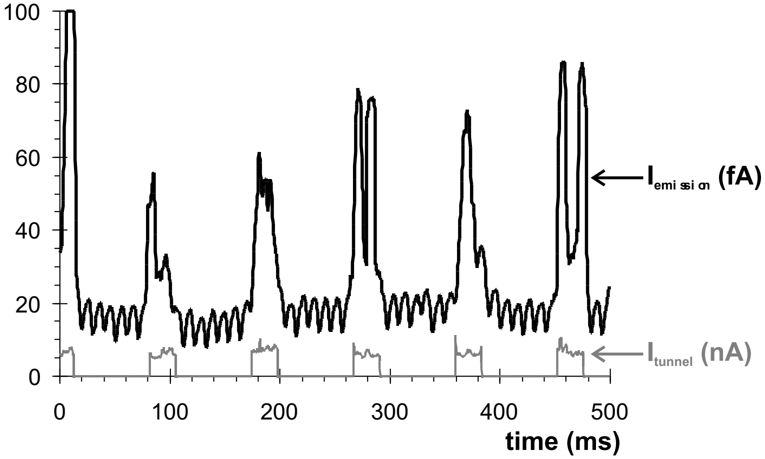

Figure 5.19: *Tunnel and emission current, when applying voltage pulses of 5 V, 20 ms.* I_{tunnel}*: tunnel current through the junction in nA.* I_{emission}*: emission current in fA.*

band of the oxide. That is the case in the region where the conduction band is pulled below the electron energy, due to the electric field over the oxide (see figure 5.12). Therefore an insulator with a large bandgap is the most attractive to use: the larger the bandgap, the smaller this scattering region will be. Defects and impurities in the insulating layer may create electron states in the bandgap and give rise to additional scattering, thus they should be minimised.

For simplicity, only emitters with a flat emission surface have been fabricated so far. In section 4.2.2 it was concluded that a sharp emitter shape is preferable because of the chromatic and spherical aberration of the accelerating field. A method to construct a tunnel junction emitter with such a shape, is to deposit an insulating layer on a field emitter tip and on top of that a thin conducting foil. By using a direction sensitive deposition method, it can be achieved that the oxide layer is thick at the shanks and thinnest at the apex of the tip.

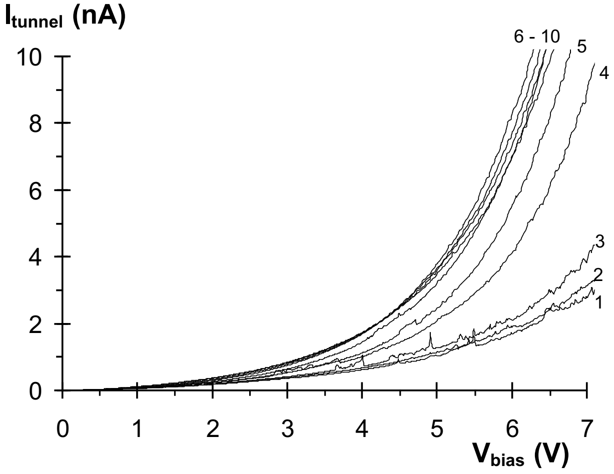

Figure 5.20: *The tunnel current of a device for 10 consecutive IV-measurements. The sequence of the measurements is as indicated by the numbers next to the lines in the graph.* I_{tunnel}*: tunnel current through the junction in nA.* V_{bias}*: bias voltage between tip and foil in V.*

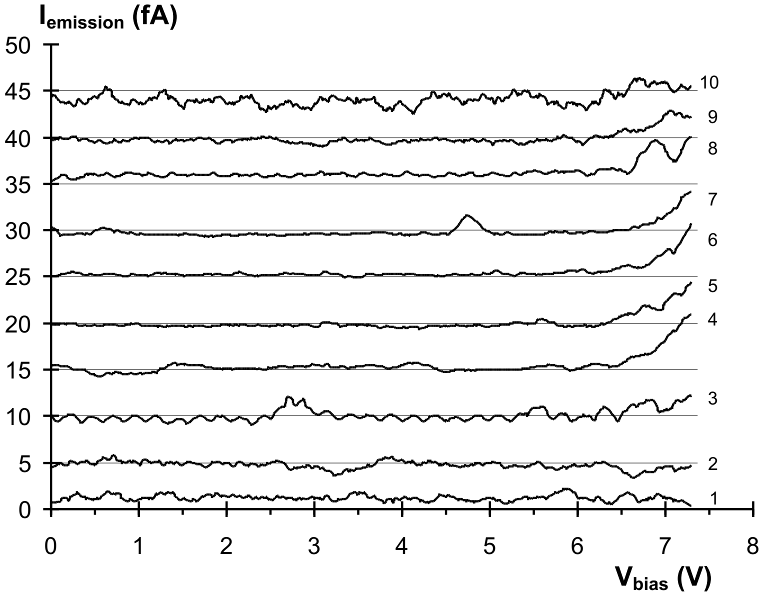

Figure 5.21: *The emission current for 10 consecutive IV-measurements, recorded simultaneously with the graphs in figure 5.20. The sequence of the measurements is as indicated by the numbers next to the lines in the graph, for clarity each measurement is offset 5 fA.* I_{emission}*: emission current in fA.* V_{bias}*: bias voltage between tip and foil in V.*

Chapter 6

Low-energy foil aberration corrector

6.1 Introduction

In electron microscopy, spherical and chromatic aberration of the lenses limit the resolution. Spherical aberration is the effect that the focussing power of the lens varies with the radius of incidence. Chromatic aberration is the dependence of the focussing power on the wavelength. In electron optics, it is more convenient to refer to the chromatic aberration as the dependence on the kinetic energy of the electron instead of its wavelength ($\lambda = \frac{h}{\sqrt{2mE_k}}$).

Scherzer [52] has shown that the spherical and chromatic aberration are always positive for electron lenses that are static, rotationally symmetric and space charge free. These conditions are satisfied by virtually all common lenses. To correct for aberrations Scherzers theorem has to be circumvented, for instance by using non rotationally symmetric optical elements. Several authors have recently reported on spherical and chromatic aberration correctors based on a series of multipoles [12, 20, 22, 42, 60, 63, 64, 67]. However, the design of these correctors is complicated, they are difficult to operate, as many parameters have to be adjusted correctly, and many power supplies of sufficient stability are needed. Compared to that a thin transparent foil, with which space charge can be put on the optical axis which can also act as a corrector with negative spherical aberration, seems very simple in design and operation. The first suggestion for a foil corrector was also from Scherzer [53], but at that time he still regarded the construction of a foil transparent to electrons as impossible. To avoid the problem of scattering in the foil, a gauze can be used instead. Some early examples of studies on a corrector with a gauze or foil are those by Barth [4] and Maruse [38]. Since then, Hanai, Hibino and Maruse have done a lot of theoretical and experimental work on foil correctors. For a recent example, see [15].

In order to avoid too much scattering in the foil, usually these correctors are operated at a beam energy at the foil of 100 keV and larger. The pressure in an electron microscope is usually 10^{-8} mbar at best and mobile adsorbates will be present on the foils surface. Electrons impinging on the surface with an energy larger than ~5 eV will crack these adsorbates and create a carbon species that locally sticks to the surface. As the adsorbates move over the surface, new adsorbates move into the beam and are cracked continuously. So the electron beam will cause a carbon build up on the foils surface. This contamination and its associated scattering and charging is a major problem for the use of phase plates in electron microscopes [10, 11] and has prevented the wide spread use of foil correctors in electron microscopes.

In chapter 2, the dependence of the scattering length on the beam energy is given. In general, the scattering length decreases for lower energy. However at very low energy, the electron mean free path increases again. For most metals the mean free path is about 5 nm for electrons entering the foil with almost zero kinetic energy. As shown in chapter 3, the fabrication of 5 nm thick free-standing foils is a practical possibility nowadays. Therefore, the development of a foil corrector operating at low kinetic energy has become interesting. Compared to high voltage foil correctors, the very low voltage operation makes the corrector more attractive for low-voltage SEM and it greatly reduces the contamination problem. An additional advantage is that by retarding the electrons to ~0 eV, the foil may act as a high-pass energy filter as explained in chapter 2.

6.2 Basic concept

6.2.1 Geometry

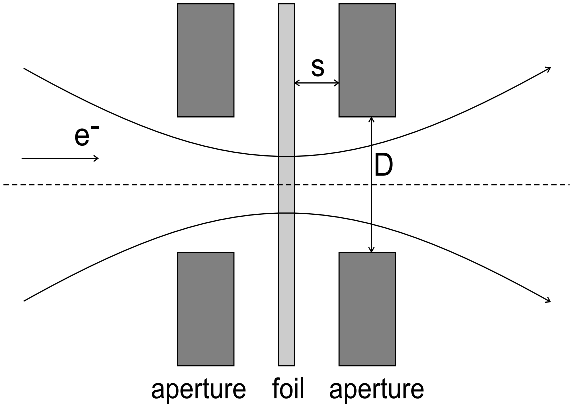

Figure 6.1: *Basic design of the foil corrector (not to scale). D: diameter of the aperture; s: gap between foil and aperture.*

A foil corrector in its most basic form is sketched in figure 6.1. It consists of a flat free-standing foil of nanometer size thickness with apertures on both sides. In the low-energy foil corrector, the foil is put on a retarding potential, such that the electrons have almost 0 eV kinetic energy when they enter the foil (and also when they have just left the foil at the other side).

6.2.2 Origin of aberration correction

In a positive lens, positive spherical aberration is the effect that the focussing power of the lens increases for increasing radius of incidence. In a negative lens with positive spherical aberration, the defocusing power of the lens decreases for increasing radius of incidence. This is illustrated in figure 6.2. In a spherical aberration corrector the opposite effect is desired.

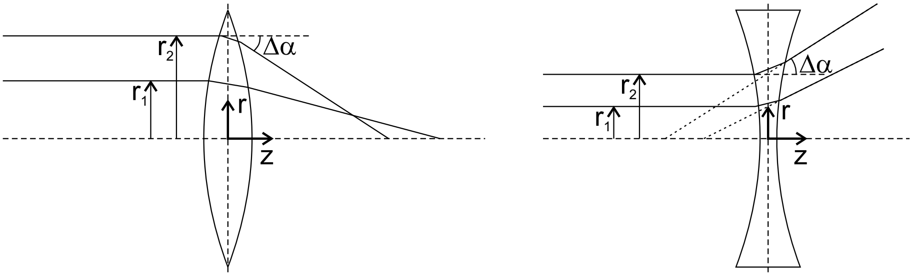

Figure 6.2: *Positive spherical aberration for a positive and a negative lens, illustrated with two rays entering the lens at different radii, r_1 and r_2. In both cases, the intercept with the z-axis shifts in the negative z direction for increasing radius of incidence.*

In order to explain the behaviour of the corrector in terms of easy to understand physics, an approximative description of its properties will be obtained by a simple analysis of the radial momentum the electron obtains in the electric field. Because of the symmetry around the foil, the calculation can be limited to one half part of the corrector: a flat surface (representing the foil) with an aperture in front of it. First, the calculation will be done for a conventional foil corrector operating at high beam energy. Thereafter the calculation for the low voltage foil corrector will be done according to the same reasoning and the difference between both correctors will be pointed out.

In a rotationally symmetric system, the radial momentum change obtained by an electron travelling in an electric field is:

$$\Delta p_r = \int_0^\infty -eE_r(z,r)dt = \int_0^\infty \frac{-eE_r(z,r)}{v_z(z,r)}dz \tag{6.1}$$

where $E_r(z,r)$ is the radial component of the electric field, and $v_z(z,r)$ is the electron's axial velocity component. A cylindrical coordinate system is adopted here in which the positive z-direction is perpendicular to the foil and directed towards the aperture, and the radial coordinate r is perpendicular to the z-axis. Close to the axis the potential $\Phi(z,r)$ can be expanded as [16]

$$\Phi(z,r) = \Phi(z) - \frac{r^2}{4}\Phi''(z) + \frac{r^4}{64}\Phi^{(4)}(z) + O(r^6) \tag{6.2}$$

where $\Phi''(z)$ and $\Phi^{(4)}(z)$ are the second and fourth derivative with respect to z, respectively. Then the radial component of the field can be written as

$$E_r(z,r) = -\frac{\partial\Phi(z,r)}{\partial r} = \frac{r}{2}\Phi''(z) - \frac{r^3}{16}\Phi^{(4)}(z) + O(r^5) \tag{6.3}$$

Inserting this in equation 6.1 and neglecting the $O(r^5)$ term, one obtains

$$\Delta p_r \approx \int_0^\infty \frac{-e}{v_z(z,r)}\left(\frac{r}{2}\Phi''(z) - \frac{r^3}{16}\Phi^{(4)}(z)\right) dz \tag{6.4}$$

Far from the corrector the field is almost zero, such that all derivatives of Φ become zero for $z \to \infty$. For a high beam energy, the electron velocity may be assumed constant and its height change can be neglected. In that case, the radial momentum change becomes:

$$\Delta p_r \approx \frac{e}{v_z}\left(\frac{1}{2}\Phi'(0)r - \frac{1}{16}\Phi'''(0)r^3\right) \tag{6.5}$$

The deflection angle due to this radial momentum is:

$$\Delta\alpha = \frac{\Delta p_r}{p_z} \tag{6.6}$$

p_z is the axial momentum of the electron leaving the corrector. If the velocity of the electron is assumed to be constant and the radial velocity component is negligible, the following substitution is allowed:

$$p_z v_z \approx 2eU \tag{6.7}$$

with U the beam potential. Inserting equations 6.5 and 6.7 into equation 6.6, a relation between the radius of incidence and the deflection angle is obtained:

$$\Delta\alpha \approx \frac{1}{4U}\left(\Phi'(0)r - \frac{1}{8}\Phi'''(0)r^3\right) \tag{6.8}$$

The first term linear in r represents the 1^{st} order focal strength. The second term proportional to r^3 is the 3^{rd} order focal strength and is a measure for the 3^{rd} order spherical aberration.

It is expected that the radial momentum change is somehow related to the electric field in the z direction at the foil because the right end of the corrector is field free. Indeed, for this situation Gauss law states that for a cylindrical box of radius R along the z-axis, the axial electric field flux entering this box at the foil is equal to the radial electric field flux leaving it through its side. In formula: $\int_0^R E_z 2\pi r dr = \int_0^\infty E_r 2\pi R dz$. An explicit relation between the deflection angle and the field is easily obtained when noting the similarity between equation 6.8 and the series expansion of the electric field in the z-direction at the foil:

$$E_z(0,r) = -\frac{\partial\Phi(z,r)}{\partial z}(z=0) = -\Phi'(0) + \frac{1}{4}\Phi'''(0)r^2 + O(r^4) \tag{6.9}$$

Thus, the deflection angle can be expressed in terms of the z-field at the foil (neglecting the $O(r^4)$ term):

$$\Delta\alpha \approx -\frac{r}{8U}\left(E_z(0,r) + E_z(0,0)\right) \tag{6.10}$$

In figure 6.3, the electric field lines in the corrector are sketched. It is evident that the absolute field strength on the foil is lowest at $r = 0$. This means that in the expression for $E_z(0,r)$, the constant term and the term proportional to r^2 must have the same sign and thus that $\Phi'(0)$ and $\Phi'''(0)$ always have opposite sign. This is also illustrated in figure 6.4 which is obtained by calculating the electric field by means of a finite element method (see section 6.4). When the foil is put on a retarding potential with respect to the aperture, $\Phi'(0)$ is positive and the corrector is a negative lens with negative spherical aberration. When the distance between the foil and the aperture is decreased, $\Phi'''(0)$ increases and thus the spherical aberration correction increases as well.

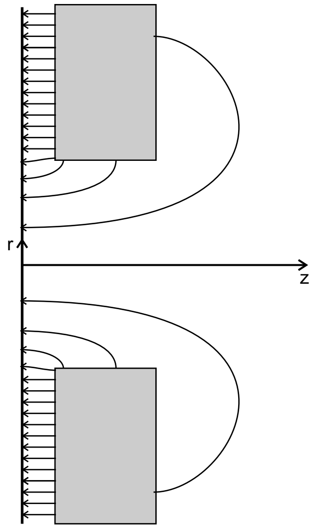

Figure 6.3: *Sketch of the electric field lines in the foil corrector.*

This calculation also applies to a set-up of two apertures without a foil, because somewhere in between the apertures there will be a flat equipotential plane as well. Therefore one may wonder whether the calculation is consistent with the well known fact that such a two aperture lens has a positive spherical aberration. In case of a foil corrector, both apertures can be put on a higher potential than the foil and both sides have a negative spherical aberration. Without the foil, this is not possible of course.

The side at the aperture with the lower potential has a positive spherical aberration. Because the electron velocity is lower at this side, its contribution is larger than the side with the negative spherical aberration and the net result is always positive.

The derivation above is not adequate for the low-energy foil corrector. We must return to equation 6.4 and substitute a suitable expression for v_z. v_z is lower for the electrons closer to the axis. Thus they will spend more time in the corrector and obtain a larger deflection away from the axis than when v_z was assumed constant. This effect contributes to a positive spherical aberration. In the low-energy foil corrector, the velocity is reduced to almost zero at the foil. Consequently, the kinetic energy depends mainly on the difference between the local potential at the position of the electron and the foil potential. In approximation, v_z can be taken equal to the total velocity:

$$v_z(z,r) \approx \sqrt{\frac{2E_k}{m}} = \sqrt{\frac{2e\Phi(z,r)}{m}} \tag{6.11}$$

E_k is the kinetic energy and m is the electron mass. After substitution into the integral in equation 6.4, a new expression for the radial momentum change is obtained. The $1/v_z$ term in the integral can be expanded into a series of r using equation 6.2. The deflection angle is $\Delta p_r/p_z$ (equation 6.6). As p_z is the axial momentum of the electron when leaving the corrector, it is (under the same approximation for v_z as above)

$$p_z \approx \sqrt{2me\Phi(\infty)} \tag{6.12}$$

with $\Phi(\infty)$ the axial potential at $z \to \infty$, which is equal to the potential on the aperture. The deflection angle is then evaluated as:

$$\Delta\alpha \approx \frac{-1}{\sqrt{\Phi(\infty)}} \left\{ \frac{1}{4} \int_0^\infty r \frac{\Phi''(z)}{\sqrt{\Phi(z)}} dz + \frac{1}{32} \int_0^\infty \frac{r^3}{\sqrt{\Phi(z)}} \left(\frac{\Phi''(z)^2}{\Phi(z)} - \Phi^{(4)}(z) \right) dz \right\} \tag{6.13}$$

Only terms up to third order in r have been kept in this expression. The integral over the 4^{th} derivative of $\Phi(z)$ is always positive, contributing to a negative spherical aberration. The integral over the square of the 2^{nd} derivative contributes to a positive spherical aberration. Which term dominates, depends on the size of the gap between foil and aperture, relative to the aperture diameter. In figure 6.4 the axial potential and its derivatives, as obtained by the finite element method to be described in section 6.4, are plotted for a fixed diameter and different gap sizes. For increasing gap size, the 4^{th} derivative decreases rapidly and hence the spherical aberration correction will become smaller and eventually turn into a positive spherical aberration. The presence of the term with $\Phi''(z)$, originating from the fact that the electron velocity decreases for lower radius of incidence, is the difference with its high voltage counterpart. For a foil corrector operating at high voltage, the spherical aberration correction decreases as well for increasing gap size, but does not change sign. Furthermore, equation 6.13 shows that the deflection angle is independent of the magnitude of the voltage applied to the aperture, provided this voltage remains positive. When the voltage on the aperture is increased with a factor n, all terms with Φ, including its derivatives, increase with a factor n. The net result is that $\Delta\alpha$ remains the same.

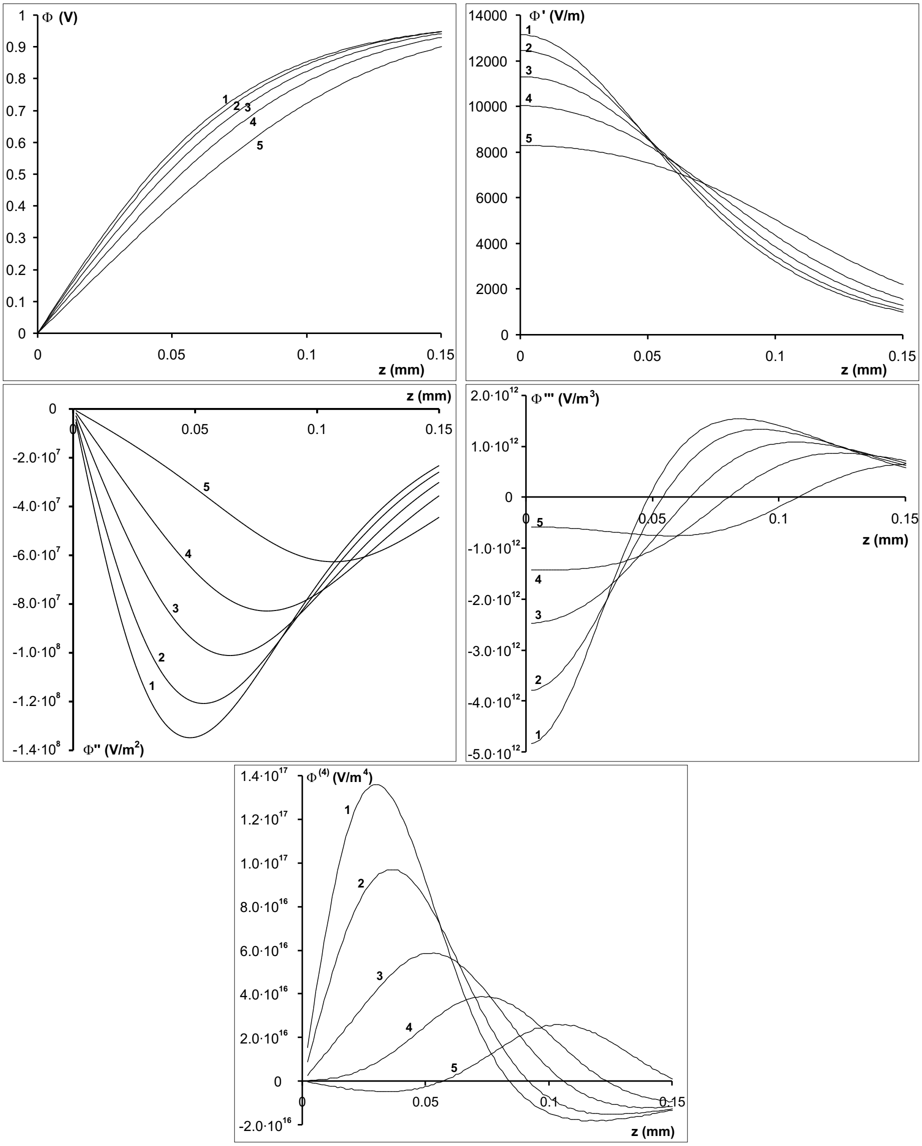

Figure 6.4: *Axial potential and its derivatives with respect to z as calculated by the finite element program Elens for aperture diameter* $D = 0.2$ *mm and different corrector gaps, indicated by the numbers in the plots. 1:* $s = 0.01$ *mm; 2:* $s = 0.03$ *mm; 3:* $s = 0.05$ *mm; 4:* $s = 0.07$ *mm; 5:* $s = 0.1$ *mm. The foil is at 0 V and the aperture at unit potential.*

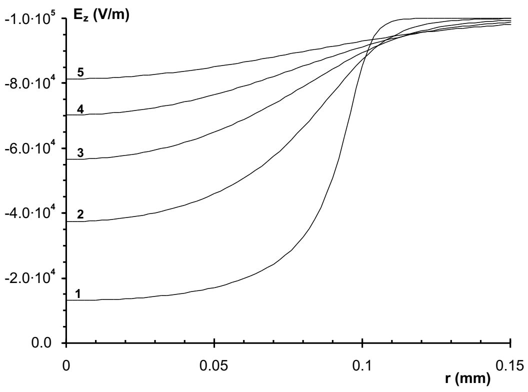

Figure 6.5: *Electric field strength in z-direction at the foils surface as function of r for aperture diameter $D = 0.2$ mm and different corrector gaps, indicated by the numbers in the plots. 1: $s = 0.01$ mm; 2: $s = 0.03$ mm; 3: $s = 0.05$ mm; 4: $s = 0.07$ mm; 5: $s = 0.1$ mm. The foil is at 0 V, the aperture is put at such potential that V/s = 100 V/mm. Note that for $r << \frac{1}{2}D$, $E_z(r)$ has a parabolic shape conform to equation 6.9.*

As mentioned in the introduction of this chapter, Scherzers theorem is circumvented in this corrector by using the foil to put charge on the optical axis. The charge on the foil is proportional to the electric field strength at the foils surface:

$$\sigma(r) = \epsilon_0 E_z(0, r), \tag{6.14}$$

where $\sigma(r)$ is the charge density in C/m^2. In figure 6.5, the field strength at the foils surface is plotted as function of r.

A positive electrostatic lens will, in general, have a positive chromatic aberration: electrons with a larger velocity will spend less time in the lens field and are less deflected. So the focussing power is weaker for higher energies. In a negative lens, the higher energy electrons are less deflected as well and the defocusing power is weaker. This results in a negative chromatic aberration for negative electrostatic lenses. Therefore a foil corrector with the foil on a retarding potential is expected to have a negative chromatic aberration.

6.3 Methods to determine C_s and C_c

The analytic evaluation above is not intended to obtain exact results. Existing aberration integrals, such as given by Typke [58] and Hawkes [18], are not suitable for this problem. They can not be applied in a situation where the electron energy goes to zero. A derivation of the aberration integrals that is suitable for this problem will be given in chapter 7. Meanwhile, the properties of any optical element can also be determined, when the electron trajectories in the exit plane are known as function of their radius and angle of incidence. Therefore, the spherical and chromatic aberration can be determined from ray tracing results. This will be discussed below. Again, the symmetry around the foil is used. The electrons start just in front of the foil, perpendicular to its surface with almost zero kinetic energy.

6.3.1 Spherical aberration

C_s is obtained from ray tracing results in two steps (see figure 6.2 for visual illustration):

1. Evaluate the deflection angle as function of the radius of incidence:

$$\Delta\alpha = a_1 r + a_3 r^3 + a_5 r^5 + ... \tag{6.15}$$

in which the focal distance is: $f = -1/a_1$.

2. Plot the z-intercept versus the radius of incidence:

$$z = z_0 - C_{s3}\alpha_1^2 - C_{s5}\alpha_1^4 + ... \tag{6.16}$$

z_0 is the intercept with the axis in absence of any aberration. α_1 is the angle under which the ray would intercept the optical axis, when only the 1^{st} order lens effect is taken into account. For rays that have entered parallel to the optical axis, this angle is equal to the deflection angle due to the 1^{st} order lens effect:

$$\alpha_1 = a_1 r \tag{6.17}$$

So C_{s3} and C_{s5} are obtained by fitting to:

$$z = z_0 - C_{s3}(a_1 r)^2 - C_{s5}(a_1 r)^4 + ... \tag{6.18}$$

a_1 is obtained from equation 6.15, by fitting the deflection angle to the polynomial in r.

6.3.2 Chromatic aberration

The chromatic aberration coefficients are obtained from

$$z = z_0 + C_{c1}\left(\frac{E_{start}}{eU_{end}}\right) + C_{c2}\left(\frac{E_{start}}{eU_{end}}\right)^2 + ... \tag{6.19}$$

in which E_{start} is the starting energy of the electron, U_{end} the potential in the exit plane and C_{c1} and C_{c2} the coefficients of 1st and 2nd order chromatic aberration.

6.4 Calculation method

The electric field was calculated with Elens [34], a finite element program. The geometry for the calculation is shown in figure 6.6. Elens divides this geometry into a fine mesh of maximum 100,000 points. The potential on every mesh point is determined such that the total energy is minimized.

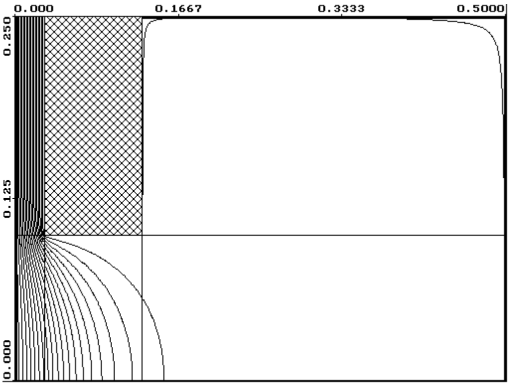

Figure 6.6: *Foil corrector with equipotentials as calculated by Elens.*

The electron trajectories are calculated with Trasys [35]. Trasys uses a high accuracy interpolation in z and r to determine the potential in between the mesh points, as described by Chmelik and Barth[9]. With this information, it can calculate the electric force on the electron at any point and thus trace its trajectory.

Trajectories starting at different radii of incidence and different energies must be calculated in order to determine the geometrical and the chromatic aberrations respectively. For every setting, a total of 16 trajectories are calculated: starting at $r = 0.05; 0.075; 0.1$ and $0.125 * D$, with forward kinetic energy $E_{start} = 0; 0.1; 0.3$ and $0.6\ eV$.

6.5 Results

The corrector has 3 independent parameters: the gap s between foil and aperture, the diameter D of the aperture and the voltage V applied to the aperture. An important result of the calculations is that the magnitude of the voltage on the aperture has little influence on the trajectories. The f, C_{s3}, C_{s5} and C_{c1} are hardly affected by the voltage, as is illustrated in figure 6.7, only the C_{c2} is. For a fixed ratio between corrector gap and diameter, the results scale linearly with the size of the corrector. Therefore the corrector properties as function of the gap are normalized to the diameter of the aperture, see figure 6.8.

For $s << D$ the f, C_{s3} and C_{c1} converge to a constant value:

$$\begin{aligned} f &= -D \\ C_{s3} &= -D \\ C_{c1} &= -2D \end{aligned} \tag{6.20}$$

Figures 6.9 and 6.10 show that the coefficient of second order chromatic aberration is independent of the gap and increases for increasing voltage respectively.

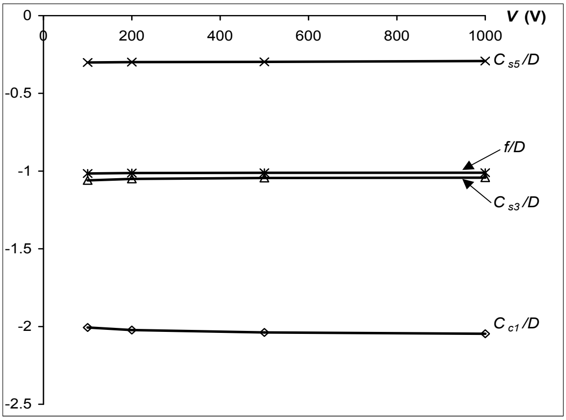

Figure 6.7: *Focal distance f, coefficients C_{s3} and C_{s5} of respectively 3^{rd} and 5^{th} order spherical aberration and coefficient of 1^{st} order chromatic aberration C_{c1} versus the voltage on the aperture, all normalized to the aperture diameter D. Ratio gap - diameter: $s/D = 0.1$.*

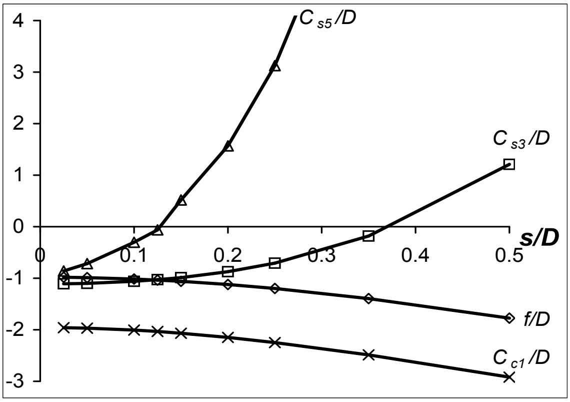

Figure 6.8: *Focal distance f, coefficients C_{s3} and C_{s5} of respectively 3^{rd} and 5^{th} order spherical aberration and coefficient of 1^{st} order chromatic aberration C_{c1} versus the corrector gap, all normalized to the aperture diameter D. Voltage on aperture: V = 100 V.*

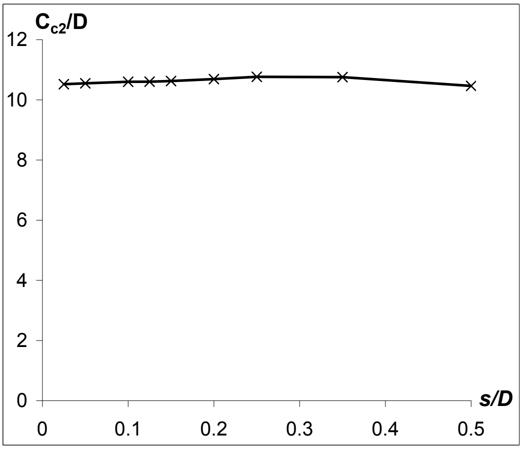

Figure 6.9: *Coefficient of 2^{nd} order chromatic aberration C_{c2}, normalized to the aperture diameter D, versus the corrector gap. Voltage on aperture: $V = 100V$.*

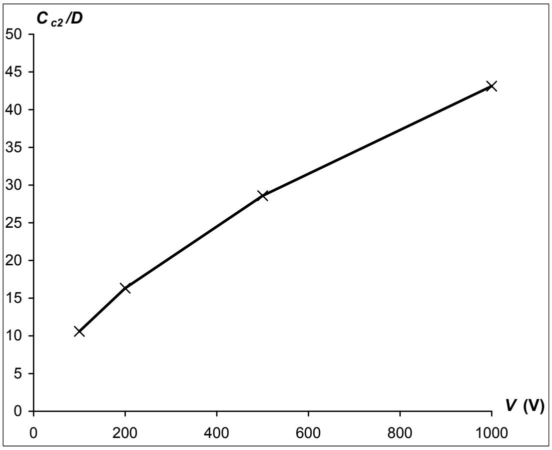

Figure 6.10: *Coefficient of 2^{nd} order chromatic aberration C_{c2}, normalized to the aperture diameter D, versus voltage V on the aperture for $s/D = 0.1$.*

6.6 Discussion

The results show that it is possible to obtain a correction for both the spherical and the chromatic aberration. To obtain a negative spherical aberration, the gap between foil and aperture should be sufficiently small, with respect to the aperture diameter. This is in agreement with the analytical evaluation in section 2. Also the observation that the magnitude of the voltage on the aperture is of little influence on the trajectories is in good agreement with the analytical evaluation.

For use in a microscope system, additional optics will be necessary to tune the corrections to a desired value and to focus the beam. A typical microscope system with this corrector is sketched in figure 6.11. The focussing lenses have to be put close to the corrector because the corrector is a very strong negative lens. Therefore, focussing the beam with magnetic lenses is not favourable, as the foil would have to be placed in the magnetic field. The consequence of this field would be that the electrons obtain a tangential velocity. Then, depending on the radius of incidence at the foil, the path length in the foil is increased, causing more scattering, and the forward energy is reduced, causing more electrons to be reflected at the foil. These problems are avoided with electrostatic lenses. In chapter 7, a calculation example on a realistic set-up with some additional electrodes will be given, showing that it is possible to focus the beam and still maintain a negative spherical and chromatic aberration.

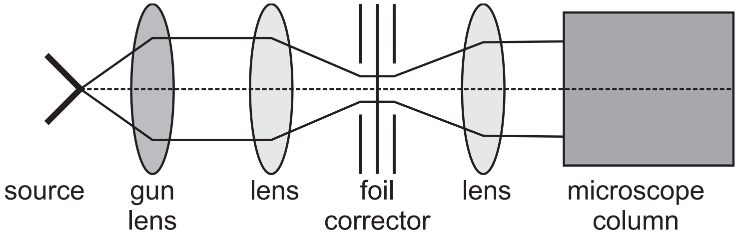

Figure 6.11: *Microscope column with the foil corrector.*

As mentioned in the introduction, the foil will act as a high pass energy filter because the electrons in the lower part of the energy distribution do not have sufficient energy to pass the foil. Furthermore, a quantum mechanical effect due to the wave character of the electrons has to be taken into account. When the electrons enter the foil, their kinetic energy is increased with around 10 eV, being the difference between the vacuum level and the bottom of the conduction band. As a consequence the wavelength is decreased. Opposed to its high voltage counterpart, this effect is not negligible for the low-energy foil corrector. The electrons form a standing wave in the foil and a quantum mechanical reflection at the foils surfaces can occur. This subject has been discussed in detail in chapter 2. The calculations in chapter 2 of the transmission as function of the electron kinetic energy show an oscillating behaviour, causing a high cut-off as well.

As the electron energy is decreased to 0 eV in the corrector, Coulomb interactions may become significant. This will set a limit to the current that can be allowed. The angular deflection caused by Coulomb interactions has been calculated with the slice method using Jiangs formulas [27] and is compared to the illumination angle. This calculation method has been explained in section 4.2.3. A corrector geometry is assumed of identical apertures on both sides of the foil, gap sizes 30 μm, aperture diameters 200 μm and a voltage between foil and apertures of 300 V, which is based on the practical limit of 10 kV/mm. It has been taken into account that in this case the field on the optical axis is considerably lower, see fig. 6.4. Then for an electron beam with a reduced brightness of 10^8 $\mathrm{Am^{-2}sr^{-1}V^{-1}}$, a diameter of 40 μm at the foil (20% of the aperture diameter) and current 1 nA (assuming no current loss in the foil), the illumination angle is $5.8 \cdot 10^{-6}$ rad and the Coulomb interactions angular deflection is $2.2 \cdot 10^{-6}$ rad. This causes an increase of the spot size of about 7%.

When the third order C_s and the first order C_c are corrected, the fifth order C_s and the second order C_c can limit the spot size. The calculations show that the C_{s5} of the corrector can be zero, giving no extra contribution to the spot size due to aberrations. Ray tracing calculations that will be presented in chapter 8 indicate that the spot size due to the second order chromatic aberration can be kept sufficiently small.

The main uncertainty is whether the transmission of electrons through the foil will be sufficient, as this has not yet been experimentally verified. There is some experimental work on the transmission of free electrons through foils at very low energies, as discussed in section 2.3.2. However, to obtain conclusive results for the low-energy foil corrector, the transmission should be measured for sub 10 nm foils and with a sub 0.1 eV energy resolution because of the quantum mechanical reflection.

6.7 Conclusion

A low voltage spherical and chromatic aberration corrector is proposed based on a thin transparent foil sandwiched between two apertures. The electrons are retarded to almost zero energy at the foil; at this energy the electrons may travel ballistically through the foil. From an approximate analytical model the feasibility to correct spherical and chromatic aberrations was shown. The third and fifth order spherical aberration coefficients as well as the first and second order chromatic aberration coefficients were obtained from electric field simulations and ray tracing. A schematic design of a corrector for potential use in a low voltage scanning electron microscope or in the gun-section of a scanning transmission electron microscope has been described. The major uncertainty is whether the current transmission through the foil will be sufficient.

Chapter 7

Aberration integrals for the low-voltage foil corrector

7.1 Introduction

In the previous chapter, the basic design for the low-voltage foil corrector was introduced (see fig. 6.1). The optical properties of this configuration depend mainly on the ratio of the gap s over the diameter D. For s sufficiently small, it is a strong negative lens with negative spherical and chromatic aberration (see fig. 6.8). Additional electrodes are necessary to focus the beam (fig. 7.1). In order to maintain the aberration correction, these electrodes must be placed close to the foil. As a consequence, the fields overlap and for calculating the optical properties, the foil, central electrodes and additional electrodes must be treated as one device.

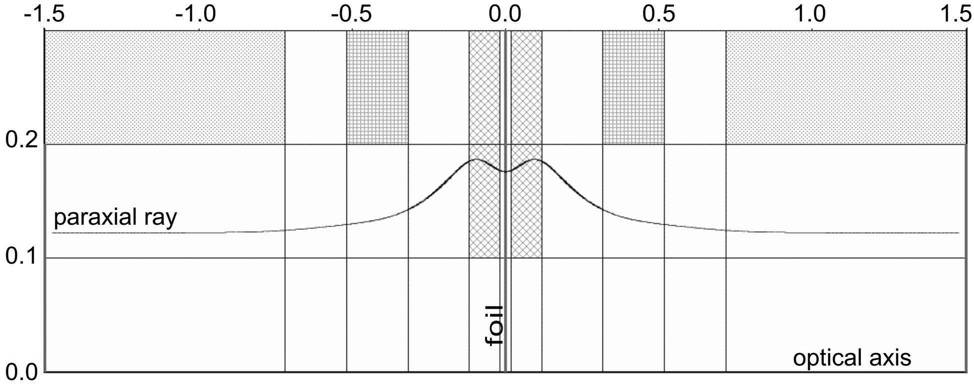

Figure 7.1: *Example design of the foil corrector with additional electrodes to focus the beam. Measures are in mm.*

The optical properties of this device can be determined by ray tracing calculations.

However, even the simple set-up in figure 7.1 has many parameters that can be varied: the sizes of all the apertures, the gaps between them and the voltage applied to them. For a system design it is convenient to have analytical expressions for the aberration integrals as well. Such formulae allow accurate calculations for many different configurations within a reasonable time. Also, the aberration integrals may better reveal the dependencies of the optical properties on the individual parameters. Finally, the validity of both methods can be confirmed by comparing their results.

Due to the presence of the foil, the odd derivates of the axial potential are discontinuous. A review of expressions for the 3^{rd} order spherical aberration for foil or gauze lenses is given by Hawkes and Kasper [16, 18]. However, most of these expressions include a simplification which is not allowed when the electron energy at the foil goes to almost zero. An exception is the paper by Munro and Wittels [45]. Their expressions for the aberration coefficients still hold at very low energies. For a characterization of the corrector independent of the probe forming system, the aberration coefficients are less suitable and the slope aberrations must be derived (as will be explained in section 7.4). These can be obtained by taking the derivatives from the equations by Munro and Wittels, but then some additional recalculations are necessary for the following reasons. The integrals by Munro and Wittels require that the height of one of the principal rays in the image plane is calculated and have the restriction that the integration must start in the object plane. For a numerical calculation this is less suitable, because the object and image position may be outside the geometry that is simulated or they may be virtual (see section 7.3). For clarity and the convenience of having the complete calculation together, the aberration terms are re-calculated starting from general trajectory equations, carefully marking the approximations used.

7.2 Derivation of C_s and C_c integrals

7.2.1 Equation for the aberrated trajectories

A trajectory equation in a time independent form can be obtained from the Lagrange equation. In a rotationally symmetric system, the Lagrange function in cylindrical coordinates ρ and z is [17]:

$$L(\rho, \rho', z) = [\varphi(\rho, z)]^{\frac{1}{2}} \left[1 + \rho'^2\right]^{\frac{1}{2}}. \tag{7.1}$$

$\varphi(\rho, z)$ is the potential and primes denote derivatives to z. The corresponding Lagrange equation is:

$$\frac{d}{dz}\left[\frac{\rho'}{(1+\rho'^2)^{\frac{1}{2}}}\varphi^{\frac{1}{2}}\right] - \frac{(1+\rho'^2)^{\frac{1}{2}}}{2\varphi^{\frac{1}{2}}}\frac{\partial\varphi}{\partial\rho} = 0. \tag{7.2}$$

The total differentiation with respect to z is performed, collecting the terms in $\partial\varphi/\partial\rho$ and $\partial\varphi/\partial z$ and the equation is multiplied by $\left(1+\rho'^2\right)^{\frac{3}{2}}/\varphi^{\frac{1}{2}}$:

$$\rho'' + \frac{1+\rho'^2}{2\varphi}\left(\rho'\frac{\partial\varphi}{\partial z} - \frac{\partial\varphi}{\partial\rho}\right) = 0. \tag{7.3}$$

The potential can be expanded as

$$\varphi(\rho,z)=\Phi(z)-\frac{\rho^2}{4}\Phi''(z)+\frac{\rho^4}{64}\Phi^{(4)}(z)+O(\rho^6) \tag{7.4}$$

where $\Phi(z)$ is the axial potential and $\Phi^{(4)}(z)$ is the fourth derivative with respect to z. In order to obtain the first and third order geometrical properties, ρ in equation 7.3 is substituted by:

$$\rho=\lambda r+\lambda^3\Delta r_3+.... \tag{7.5}$$

Collecting the terms in λ leads to the paraxial ray equation:

$$r''+\frac{\Phi'}{2\Phi}r'+\frac{\Phi''}{4\Phi}r=0 \tag{7.6}$$

and collecting the terms in λ^3 leads to the equation:

$$\begin{aligned}&\Delta r_3''+\frac{\Phi'}{2\Phi}\Delta r_3'+\frac{\Phi''}{4\Phi}\Delta r_3=\\&-\frac{1}{2}\frac{\Phi'}{\Phi}r'^3-\frac{1}{4}\frac{\Phi''}{\Phi}r'^2r+\frac{1}{8}\frac{\Phi'''\Phi-\Phi''\Phi'}{\Phi^2}r'r^2+\frac{1}{32}\frac{\Phi^{(4)}\Phi-2\Phi''^2}{\Phi^2}r^3.\end{aligned} \tag{7.7}$$

Equation 7.6 can be rewritten as:

$$\frac{d}{dz}\left[\Phi^{\frac{1}{2}}r'\right]+\frac{\Phi''}{4\Phi^{\frac{1}{2}}}r=0 \tag{7.8}$$

To the right hand part of equation 7.7 the term

$$\frac{1}{\Phi^{\frac{1}{2}}}\frac{d}{dz}\left[\frac{1}{2}\Phi^{\frac{1}{2}}r'^3+\frac{1}{8}\frac{\Phi''}{\Phi^{\frac{1}{2}}}r'r^2\right] \tag{7.9}$$

is added in the closed form and subtracted in the differentiated form. Furthermore the r'' terms are removed by substitution of equation 7.6 and the whole equation is multiplied by $\Phi^{\frac{1}{2}}$. The left hand part of equation 7.7 is rewritten in a differential form, similar to equation 7.8. Then equation 7.7 transforms into:

$$\begin{aligned}&\frac{d}{dz}\left[\Phi^{\frac{1}{2}}\Delta r_3'\right]+\frac{\Phi''}{4\Phi^{\frac{1}{2}}}\Delta r_3=\\&\frac{d}{dz}\left[\frac{1}{2}\Phi^{\frac{1}{2}}r'^3+\frac{1}{8}\frac{\Phi''}{\Phi^{\frac{1}{2}}}r'r^2\right]+\Phi^{\frac{1}{2}}\left[\frac{1}{32}\frac{\Phi^{(4)}\Phi-\Phi''^2}{\Phi^2}r^3-\frac{1}{8}\frac{\Phi''}{\Phi}r'^2r\right].\end{aligned} \tag{7.10}$$

7.2.2 Spherical aberration

Equation 7.10 is an inhomogeneous equation of the form

$$\frac{d}{dz}\left[\Phi^{\frac{1}{2}}\Delta r_3'\right]+\frac{\Phi''}{4\Phi^{\frac{1}{2}}}\Delta r_3=F(z) \tag{7.11}$$

with the paraxial trajectory equation 7.8 as the homogeneous part. Let r_α and r_β be any two independent solutions of the paraxial equation 7.8 with Wronski determinant

$$W_{\alpha\beta}=\Phi^{\frac{1}{2}}\left(r_\alpha'r_\beta-r_\beta'r_\alpha\right), \tag{7.12}$$

Then any solution of 7.11 can be written as:

$$\Delta r_3 = \alpha r_\alpha(z) + \beta r_\beta(z) + \frac{1}{W_{\alpha\beta}} \left\{ r_\alpha(z) \int^z F(\zeta) r_\beta(\zeta) d\zeta - r_\beta(z) \int^z F(\zeta) r_\alpha(\zeta) d\zeta \right\}. \tag{7.13}$$

The constants α and β are obtained from the initial conditions in the object plane:

$$\Delta r_3\left(z_o\right) = \Delta r_3'\left(z_o\right) = 0. \tag{7.14}$$

Suffix o refers to the object plane and in the forthcoming, suffix i will refer to the image plane. This leads to the general expression for the third order geometrical aberration:

$$\begin{aligned} \Delta r_3 = & -\frac{\Phi_o^{\frac{1}{2}}}{2W_{\alpha\beta}} \left[r'^2(z_o) + \frac{\Phi''(z_o)}{4\Phi_o^{\frac{1}{2}}} r^2(z_o) \right] r'(z_o) \left[r_\alpha(z) r_\beta(z_o) - r_\alpha(z_o) r_\beta(z) \right] \\ & + \frac{r_\alpha(z)}{2W_{\alpha\beta}} \int_{z_o}^{z} \left\{ -\Phi^{\frac{1}{2}} r'^3 r_\beta' - \frac{1}{4}\frac{\Phi''}{\Phi^{\frac{1}{2}}} r' r^2 r_\beta' - \frac{1}{4}\frac{\Phi''}{\Phi^{\frac{1}{2}}} r'^2 r r_\beta + \frac{1}{16}\left[\frac{\Phi^{(4)}}{\Phi^{\frac{1}{2}}} - \frac{\Phi''^2}{\Phi^{\frac{3}{2}}} \right] r^3 r_\beta \right\} d\zeta \\ & - \frac{r_\beta(z)}{2W_{\alpha\beta}} \int_{z_o}^{z} \left\{ -\Phi^{\frac{1}{2}} r'^3 r_\alpha' - \frac{1}{4}\frac{\Phi''}{\Phi^{\frac{1}{2}}} r' r^2 r_\alpha' - \frac{1}{4}\frac{\Phi''}{\Phi^{\frac{1}{2}}} r'^2 r r_\alpha + \frac{1}{16}\left[\frac{\Phi^{(4)}}{\Phi^{\frac{1}{2}}} - \frac{\Phi''^2}{\Phi^{\frac{3}{2}}} \right] r^3 r_\alpha \right\} d\zeta \end{aligned} \tag{7.15}$$

The coefficient of third order spherical aberration is defined as:

$$C_s = \frac{\Delta r_3(z_i)}{r'^3(z_i)}. \tag{7.16}$$

By making an appropriate choice for the rays r_α and r_β, the expression for C_s can be simplified to an integral over only one trajectory. Let their initial conditions in the object plane be:

$$r_\alpha(z_o) = 0,\ r_\alpha'(z_o) = 1,\ r_\beta(z_o) = 1,\ r_\beta'(z_o) = 0, \tag{7.17}$$

hence

$$\begin{aligned} & W_{\alpha\beta} = \Phi_o^{\frac{1}{2}}, \\ & r_\alpha(z_i) = 0,\ r_\alpha'(z_i) = M_a, \\ & r_\beta(z_i) = M = \sqrt{\frac{\Phi_o}{\Phi_i}} \frac{1}{M_a} = \sqrt{\frac{\Phi_o}{\Phi_i}} \frac{1}{r_\alpha'(z_i)}, \end{aligned} \tag{7.18}$$

in which M is the magnification and M_a is the angular magnification. The trajectory $r(z)$ can be written as:

$$r(z) = r'(z_o) r_\alpha(z). \tag{7.19}$$

This results in:

$$C_s = -\frac{1}{2\Phi_i^{\frac{1}{2}} r_\alpha'^4(z_i)} \int_{z_o}^{z_i} \left\{ -\Phi^{\frac{1}{2}} r_\alpha'^4 - \frac{1}{2}\frac{\Phi''}{\Phi^{\frac{1}{2}}} r_\alpha'^2 r_\alpha^2 + \frac{1}{16}\left[\frac{\Phi^{(4)}}{\Phi^{\frac{1}{2}}} - \frac{\Phi''^2}{\Phi^{\frac{3}{2}}} \right] r_\alpha^4 \right\} d\zeta, \tag{7.20}$$

which can also be written as:

$$C_s = \frac{1}{2\Phi_i^{\frac{1}{2}} r_\alpha'^4(z_i)} \int_{z_o}^{z_i} \Phi^{\frac{1}{2}} \left\{ \left[r_\alpha'^2 + \frac{1}{4}\frac{\Phi''}{\Phi} r_\alpha^2 \right]^2 - \frac{1}{16}\frac{\Phi^{(4)}}{\Phi} r_\alpha^4 \right\} d\zeta. \tag{7.21}$$

The latter form shows that only the term with the 4^{th} derivative of the axial potential can contribute to a negative spherical aberration.

In previous work on aberration integrals, the C_s integral is usually integrated to obtain expressions without the $\Phi^{(4)}$ term. This is not allowed when Φ approaches zero and is not necessary nowadays because the axial potential and its derivatives can be calculated accurately, as will be demonstrated by the calculation example in section 7.5.

7.2.3 Chromatic aberration

For the first order chromatic aberration, equation 7.6 is rewritten as:

$$r'' + \frac{\Phi'}{2(\Phi + \Delta\Phi)} r' + \frac{\Phi''}{4(\Phi + \Delta\Phi)} r = 0 \tag{7.22}$$

where

$$r = r(\Delta\Phi) \tag{7.23}$$

The chromatic aberration of the trajectory is defined as:

$$\Delta r_c = \lim_{\Delta\Phi = 0} \frac{\partial r}{\partial(\Delta\Phi)} \tag{7.24}$$

Differentiation of equation 7.22 with respect to $\Delta\Phi$ and taking the values at $\Delta\Phi = 0$ leads to the equation:

$$\Delta r_c'' + \frac{\Phi'}{2\Phi}\Delta r_c' + \frac{\Phi''}{4\Phi}\Delta r_c = \left[\frac{\Phi'}{2\Phi} r' + \frac{\Phi''}{4\Phi} r \right] \frac{\Delta\Phi}{\Phi}. \tag{7.25}$$

From the right hand part of equation 7.25 the term

$$\frac{\Delta\Phi}{2\Phi^{\frac{1}{2}}} \frac{d}{dz} \left[\frac{r'}{\Phi^{\frac{1}{2}}} \right] \tag{7.26}$$

is subtracted in the closed form and the same term is added in the differentiated form, with substitution of equation 7.6 to remove the r'' term. The whole equation is multiplied by $\Phi^{\frac{1}{2}}$ and the left hand part is rewritten in a differential form, similar to equation 7.8. Then equation 7.25 transforms into:

$$\frac{d}{dz}\left[\Phi^{\frac{1}{2}} \Delta r_c' \right] + \frac{\Phi''}{4\Phi^{\frac{1}{2}}}\Delta r_c = \left[-\frac{d}{dz}\left[\frac{r'}{\Phi^{\frac{1}{2}}} \right] + \frac{\Phi''}{4\Phi^{\frac{3}{2}}} r \right] \frac{\Delta\Phi}{2}. \tag{7.27}$$

The solution for Δr_c is identical to that for Δr_3 in equation 7.13, with $F(z)$ equal to the right hand part of equation 7.27. With the initial condition

$$\Delta r_c(z_o) = \Delta r_c'(z_o) = 0, \tag{7.28}$$

the general expression for the first order chromatic aberration is:

$$\begin{aligned}\Delta r_c = &\frac{\Delta\Phi}{2W_{\alpha\beta}\Phi_o^{\frac{1}{2}}} r'(z_o)\left[r_\alpha(z) r_\beta(z_o) - r_\alpha(z_o) r_\beta(z)\right] \\ &+ \frac{r_\alpha(z)\Delta\Phi}{2W_{\alpha\beta}} \int_{z_o}^{z} \left\{\frac{1}{\Phi^{\frac{1}{2}}} r' r'_\beta + \frac{1}{4}\frac{\Phi''}{\Phi^{\frac{3}{2}}} r r_\beta\right\} d\zeta \\ &- \frac{r_\beta(z)\Delta\Phi}{2W_{\alpha\beta}} \int_{z_o}^{z} \left\{\frac{1}{\Phi^{\frac{1}{2}}} r' r'_\alpha + \frac{1}{4}\frac{\Phi''}{\Phi^{\frac{3}{2}}} r r_\alpha\right\} d\zeta. \qquad (7.29)\end{aligned}$$

The coefficient of first order chromatic aberration is defined as:

$$C_c = -\frac{\Phi_i}{\Delta\Phi}\frac{\Delta r_c(z_i)}{r'(z_i)}. \qquad (7.30)$$

With the same boundary conditions as in equations 7.17 to 7.19, C_c can be written as:

$$C_c = \frac{\Phi_i^{\frac{1}{2}}}{2r'^2_\alpha(z_i)} \int_{z_o}^{z_i} \left\{\frac{1}{\Phi^{\frac{1}{2}}} r'^2_\alpha + \frac{1}{4}\frac{\Phi''}{\Phi^{\frac{3}{2}}} r_\alpha^2\right\} d\zeta. \qquad (7.31)$$

7.3 Integrals for numerical calculation

For a numerical calculation, the integrals from object to image plane are less suitable, because the object and image position may be outside the geometry that is simulated or they may be virtual. It is more convenient to have an integral from start to exit plane, being the boundary planes of the geometry that is simulated. The electron ray is supposed to come from the object plane to the start plane through field free space. Also the trajectory from exit plane to image plane is supposed to be field free. Then the integrals from object to image can be rewritten as follows:

$$\begin{aligned}&\int_{z_o}^{z_i} f(r(z), \Phi(z), ...)d\zeta = f(r(z_s), \Phi(z_s), ...)(z_s - z_o) \\ &+ \int_{z_s}^{z_e} f(r(z), \Phi(z), ...)d\zeta + f(r(z_e), \Phi(z_e), ...)(z_i - z_e). \qquad (7.32)\end{aligned}$$

Suffixes s and e denote the start and exit plane respectively. For any ray r_χ in field free space:

$$(z_s - z_o) = \frac{r_\chi(z_s) - r_\chi(z_o)}{r'_\chi(z_s)}, \; (z_i - z_e) = \frac{r_\chi(z_i) - r_\chi(z_e)}{r'_\chi(z_e)}. \qquad (7.33)$$

Equations 7.20 and 7.31 are rewritten as:

$$\begin{aligned} C_s = \frac{1}{2}\left(\frac{\Phi_s}{\Phi_e}\right)^{\frac{1}{2}}\frac{r_\alpha(z_s)}{r'^4_\alpha(z_e)} - \frac{1}{2\Phi_e^{\frac{1}{2}} r'^4_\alpha(z_e)}\int_{z_s}^{z_e}\Bigg\{ -\Phi^{\frac{1}{2}} r'^4_\alpha - \frac{1}{2}\frac{\Phi''}{\Phi^{\frac{1}{2}}} r'^2_\alpha r^2_\alpha \\ + \frac{1}{16}\left[\frac{\Phi^{(4)}}{\Phi^{\frac{1}{2}}} - \frac{\Phi''^2}{\Phi^{\frac{3}{2}}}\right] r^4_\alpha\Bigg\} d\zeta - \frac{1}{2}\frac{r_\alpha(z_e)}{r'_\alpha(z_e)} \end{aligned} \tag{7.34}$$

$$C_c = \frac{1}{2}\left(\frac{\Phi_e}{\Phi_s}\right)^{\frac{1}{2}}\frac{r_\alpha(z_s)}{r'^2_\alpha(z_e)} + \frac{\Phi_e^{\frac{1}{2}}}{2r'^2_\alpha(z_e)}\int_{z_s}^{z_e}\left\{\frac{1}{\Phi^{\frac{1}{2}}} r'^2_\alpha + \frac{1}{4}\frac{\Phi''}{\Phi^{\frac{3}{2}}} r^2_\alpha\right\} d\zeta - \frac{1}{2}\frac{r_\alpha(z_e)}{r'_\alpha(z_e)}. \tag{7.35}$$

Special attention must be paid to the case that the potential at the foil is exactly zero. Only trajectories that are incident perpendicular to the foil have to be considered, other trajectories will be reflected at the foil. To understand the behaviour of the integrals, it is helpful to look at the series expansion of the potential and the trajectory as function of z:

$$\begin{aligned} \Phi(z) &= E_1|z-z_f| + \frac{E_3}{6}|z-z_f|^3 + \frac{E_5}{120}|z-z_f|^5 + O(|z-z_f|^7) \\ r(z) &= r_f\left[1 - \frac{E_3}{12E_1}(z-z_f)^2 + O((z-z_f)^4)\right], \end{aligned} \tag{7.36}$$

where suffix f refers to the foil, E_1 and E_3 are constants. This series expansion shows that Φ'', $\Phi^{(4)}$ and r'_α go to zero as Φ. Using l'Hospitals rule, it can be seen that the integrand in equation 7.34 equals zero at the foil. For the integrand in equation 7.35, the term $\frac{r'^2_\alpha}{\Phi^{\frac{1}{2}}}$ equals zero as well, but the term $\frac{1}{4}\frac{\Phi''}{\Phi^{\frac{3}{2}}}r^2_\alpha$ goes to infinity as $1/\Phi^{\frac{1}{2}}$. A cure is to subtract a term $K\frac{d}{dz}(\Phi^{\frac{1}{2}})$ from the integrand which cancels the infinity. This term can be integrated analytically, so the integrated term can be added to the remaining integral to compensate the modification of the integrand. The value for the constant K is found by applying l'Hospitals rule to the new integrand:

$$\begin{aligned} \lim_{z\to z_f} \quad & \frac{\frac{1}{4}\Phi'' r^2_\alpha - K\Phi^{\frac{3}{2}}\frac{d}{dz}\left(\Phi^{\frac{1}{2}}\right)}{\Phi^{\frac{3}{2}}} = \lim_{z\to z_f}\frac{\frac{d}{dz}\left(\frac{1}{4}\Phi'' r^2_\alpha - K\Phi^{\frac{3}{2}}\frac{d}{dz}(\Phi^{\frac{1}{2}})\right)}{\frac{d}{dz}(\Phi^{\frac{3}{2}})} = \\ \lim_{z\to z_f} \quad & \frac{\frac{1}{4}\Phi''' r^2_\alpha - \frac{1}{2}K\Phi'^2}{\frac{3}{2}\Phi'\Phi^{\frac{1}{2}}} \end{aligned} \tag{7.37}$$

The proper choice of K makes the numerator of the last term equal to zero. Because the odd order derivatives are discontinuous at the foil, the integration left and right from the foil is treated separately. The symbols z_{f-} and z_{f+} refer to the position at the foils left and right side:

$$z_{f-} = \lim_{z\uparrow z_f} z\ ,\ z_{f+} = \lim_{z\downarrow z_f} z. \tag{7.38}$$

A suitable term to cancel the infinity for the integration from start plane to foil is:

$$\int_{z_s}^{z_f}\frac{\Phi'''(z_{f-})r^2_\alpha(z_{f-})}{2\ \Phi'^2(z_{f-})}\frac{d}{dz}(\Phi^{\frac{1}{2}})dz = -\frac{\Phi'''(z_{f-})r^2_\alpha(z_{f-})}{2\ \Phi'^2(z_{f-})}\Phi^{\frac{1}{2}}(z_s), \tag{7.39}$$

and for the integration from foil to end plane:

$$\int_{z_f}^{z_e} \frac{\Phi'''(z_{f+})r_\alpha^2(z_{f+})}{2\ \Phi'^2(z_{f+})}\frac{d}{dz}(\Phi^{\frac{1}{2}})dz = \frac{\Phi'''(z_{f+})r_\alpha^2(z_{f+})}{2\ \Phi'^2(z_{f+})}\Phi^{\frac{1}{2}}(z_e), \tag{7.40}$$

The integrands in the left hand parts are subtracted from the integrand in 7.35 and the right hand parts are added to the new integrals:

$$\begin{aligned} C_c = {} & \frac{1}{2}\left(\frac{\Phi_e}{\Phi_s}\right)^{\frac{1}{2}}\frac{r_\alpha(z_s)}{r_\alpha'^2(z_e)} - \frac{1}{2}\frac{r_\alpha(z_e)}{r_\alpha'(z_e)} \\ & + \frac{\Phi_i^{\frac{1}{2}}}{2r_\alpha'^2(z_e)}\left\{\int_{z_s}^{z_f}\left[\frac{r_\alpha'^2}{\Phi^{\frac{1}{2}}} + \frac{\Phi'' r_\alpha^2}{4\Phi^{\frac{3}{2}}} - \frac{\Phi'''(z_{f-})r_\alpha^2(z_{f-})\Phi'}{4\Phi'^2(z_{f-})\Phi^{\frac{1}{2}}}\right]d\zeta - \frac{\Phi'''(z_{f-})r_\alpha^2(z_{f-})}{2\Phi'^2(z_{f-})}\Phi^{\frac{1}{2}}(z_s)\right\} \\ & + \frac{\Phi_i^{\frac{1}{2}}}{2r_\alpha'^2(z_e)}\left\{\int_{z_f}^{z_e}\left[\frac{r_\alpha'^2}{\Phi^{\frac{1}{2}}} + \frac{\Phi'' r_\alpha^2}{4\Phi^{\frac{3}{2}}} - \frac{\Phi'''(z_{f+})r_\alpha^2(z_{f+})\Phi'}{4\Phi'^2(z_{f+})\Phi^{\frac{1}{2}}}\right]d\zeta + \frac{\Phi'''(z_{f+})r_\alpha^2(z_{f+})}{2\Phi'^2(z_{f+})}\Phi^{\frac{1}{2}}(z_e)\right\}. \end{aligned} \tag{7.41}$$

7.4 Slope aberrations

A typical system with a foil corrector is sketched in figure 7.2. The integrals that have been obtained in the previous section can be used to calculate the C_s and C_c for different corrector setups. When comparing these different set-ups independent of the probe forming lens system, it is required that they have the same first order optics. Otherwise, the first order optics of the probe forming lens system should be adjusted as well, causing the system to have a different spherical and chromatic aberration.

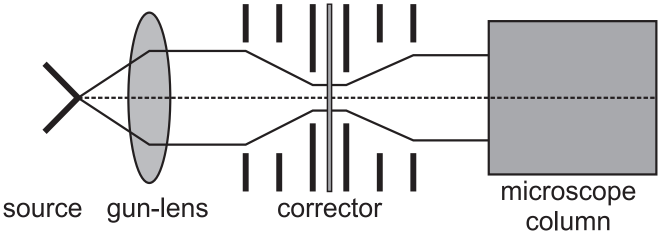

Figure 7.2: *Microscope column with the foil corrector.*

In order to characterize the corrector independent of the probe forming lens system, the situation in which the electron ray enters and leaves the corrector parallel to the axis is used. The coefficients of spherical and chromatic aberration C_s and C_c are related to an intercept with the optical axis, so they cannot be calculated. However, in the parallel case the contributions of the corrector to the total C_s and C_c of the probe forming system are simply proportional to the 3^{rd} order slope aberration $\Delta r_3'$

and the chromatic slope aberration $\Delta r'_c$ at the corrector exit:

$$C_{s,p} = -\Delta r'_3(z_e) r_s \left[\frac{\Phi_e}{\Phi_p}\right]^{\frac{1}{2}} \frac{1}{tan^4(\alpha_p)}, \tag{7.42}$$

$$C_{c,p} = \Delta r'_c(z_e) r_s \frac{[\Phi_e \Phi_p]^{\frac{1}{2}}}{\Delta\Phi} \frac{1}{tan^2(\alpha_p)}. \tag{7.43}$$

Suffix p refers to the probe. α_p is the half opening angle in the probe. r_s is the radius of incidence at the corrector start plane.

The general expressions for the slope aberrations are obtained by differentiating equations 7.15 and 7.29:

$$\begin{aligned}
\Delta r'_3 = &\frac{1}{2}\left[r'^2(z) + \frac{\Phi''}{4\Phi} r^2(z)\right] r'(z) \\
&- \frac{\Phi_o^{\frac{1}{2}}}{2W_{\alpha\beta}} \left[r'^2(z_o) + \frac{\Phi''(z_o)}{4\Phi_o^{\frac{1}{2}}} r^2(z_o)\right] r'(z_o) \left[r'_\alpha(z) r_\beta(z_o) - r_\alpha(z_o) r'_\beta(z)\right] \\
&+ \frac{r'_\alpha(z)}{2W_{\alpha\beta}} \int_{z_o}^{z} \left\{-\Phi^{\frac{1}{2}} r'^3 r'_\beta - \frac{1}{4}\frac{\Phi''}{\Phi^{\frac{1}{2}}} r' r^2 r'_\beta - \frac{1}{4}\frac{\Phi''}{\Phi^{\frac{1}{2}}} r'^2 r r_\beta + \frac{1}{16}\left[\frac{\Phi^{(4)}}{\Phi^{\frac{1}{2}}} - \frac{\Phi''^2}{\Phi^{\frac{3}{2}}}\right] r^3 r_\beta\right\} d\zeta \\
&- \frac{r'_\beta(z)}{2W_{\alpha\beta}} \int_{z_o}^{z} \left\{-\Phi^{\frac{1}{2}} r'^3 r'_\alpha - \frac{1}{4}\frac{\Phi''}{\Phi^{\frac{1}{2}}} r' r^2 r'_\alpha - \frac{1}{4}\frac{\Phi''}{\Phi^{\frac{1}{2}}} r'^2 r r_\alpha + \frac{1}{16}\left[\frac{\Phi^{(4)}}{\Phi^{\frac{1}{2}}} - \frac{\Phi''^2}{\Phi^{\frac{3}{2}}}\right] r^3 r_\alpha\right\} d\zeta
\end{aligned} \tag{7.44}$$

$$\begin{aligned}
\Delta r'_c = &-\frac{\Delta\Phi}{2\Phi} r'(z) + \frac{\Delta\Phi}{2W_{\alpha\beta}\Phi_o^{\frac{1}{2}}} r'(z_o) \left[r'_\alpha(z) r_\beta(z_o) - r_\alpha(z_o) r'_\beta(z)\right] \\
&+ \frac{r'_\alpha(z)\Delta\Phi}{2W_{\alpha\beta}} \int_{z_o}^{z} \left\{\frac{1}{\Phi^{\frac{1}{2}}} r' r'_\beta + \frac{1}{4}\frac{\Phi''}{\Phi^{\frac{3}{2}}} r r_\beta\right\} d\zeta - \frac{r'_\beta(z)\Delta\Phi}{2W_{\alpha\beta}} \int_{z_o}^{z} \left\{\frac{1}{\Phi^{\frac{1}{2}}} r' r'_\alpha + \frac{1}{4}\frac{\Phi''}{\Phi^{\frac{3}{2}}} r r_\alpha\right\} d\zeta.
\end{aligned} \tag{7.45}$$

Following the method outlined in section 7.3, the slope aberrations at the corrector exit can be written as:

$$\begin{aligned}
\Delta r'_3(z_e) = &\frac{1}{2} r'^3(z_e) - \frac{\Phi_o^{\frac{1}{2}}}{2W_{\alpha\beta}} r'^3(z_s) \left[r'_\alpha(z_e) r_\beta(z_s) - r_\alpha(z_s) r'_\beta(z_e)\right] \\
&+ \frac{r'_\alpha(z_e)}{2W_{\alpha\beta}} \int_{z_s}^{z_e} \left\{-\Phi^{\frac{1}{2}} r'^3 r'_\beta - \frac{1}{4}\frac{\Phi''}{\Phi^{\frac{1}{2}}} r' r^2 r'_\beta - \frac{1}{4}\frac{\Phi''}{\Phi^{\frac{1}{2}}} r'^2 r r_\beta + \frac{1}{16}\left[\frac{\Phi^{(4)}}{\Phi^{\frac{1}{2}}} - \frac{\Phi''^2}{\Phi^{\frac{3}{2}}}\right] r^3 r_\beta\right\} d\zeta \\
&- \frac{r'_\beta(z_e)}{2W_{\alpha\beta}} \int_{z_s}^{z_e} \left\{-\Phi^{\frac{1}{2}} r'^3 r'_\alpha - \frac{1}{4}\frac{\Phi''}{\Phi^{\frac{1}{2}}} r' r^2 r'_\alpha - \frac{1}{4}\frac{\Phi''}{\Phi^{\frac{1}{2}}} r'^2 r r_\alpha + \frac{1}{16}\left[\frac{\Phi^{(4)}}{\Phi^{\frac{1}{2}}} - \frac{\Phi''^2}{\Phi^{\frac{3}{2}}}\right] r^3 r_\alpha\right\} d\zeta
\end{aligned} \tag{7.46}$$

$$\Delta r_c'(z_e) = -\frac{\Delta\Phi}{2\Phi_e}r'(z_e) + \frac{\Delta\Phi}{2W_{\alpha\beta}\Phi_o^{\frac{1}{2}}}r'(z_s)\left[r_\alpha'(z_e)r_\beta(z_s) - r_\alpha(z_s)r_\beta'(z_e)\right]$$
$$+ \frac{r_\alpha'(z_e)\Delta\Phi}{2W_{\alpha\beta}}\int_{z_s}^{z_e}\left\{\frac{1}{\Phi^{\frac{1}{2}}}r'r_\beta' + \frac{1}{4}\frac{\Phi''}{\Phi^{\frac{3}{2}}}rr_\beta\right\}d\zeta - \frac{r_\beta'(z_e)\Delta\Phi}{2W_{\alpha\beta}}\int_{z_s}^{z_e}\left\{\frac{1}{\Phi^{\frac{1}{2}}}r'r_\alpha' + \frac{1}{4}\frac{\Phi''}{\Phi^{\frac{3}{2}}}rr_\alpha\right\}d\zeta. \tag{7.47}$$

Because the object plane may be asymptotic, the boundary condition for r_α in equation 7.17 is unsuitable. Alternatively, the principal rays will now be defined by their conditions at the foil:

$$r_\alpha(z_f) = 0,\ r_\alpha'(z_f) = 1,\ r_\beta(z_f) = 1,\ r_\beta'(z_f) = 0,\ W_{\alpha\beta} = \Phi_f^{\frac{1}{2}}. \tag{7.48}$$

For the low-voltage foil corrector, it is desired that the beam has zero slope at the foil. So the first order optics of the corrector must meet three requirements: zero slope at the start plane, at the foil and at the exit plane. One of these three can be taken as a starting point in the calculations and subsequently the proper settings must be found such that also the other two conditions are met. When the zero slope at the start plane is taken as starting point, the trajectory satisfies:

$$r(z) = \left[\frac{\Phi_s}{\Phi_f}\right]^{\frac{1}{2}} r_s\left[r_\alpha'(z_s)r_\beta(z) - r_\beta'(z_s)r_\alpha(z)\right] \tag{7.49}$$

This can be substituted into equations 7.46 and 7.47.

However, with the definition of the principal rays in equation 7.48, the expressions take their most simple form when the zero slope at the foil is taken as starting point:

$$r(z) = r_f r_\beta(z) \tag{7.50}$$

and the slope aberrations are:

$$\Delta r_3'(z_e) = \frac{1}{2}r_f^3\left[r_\beta'^3(z_e) - \frac{\Phi_o^{\frac{1}{2}}}{\Phi_f^{\frac{1}{2}}}r_\beta'^3(z_s)\left[r_\alpha'(z_e)r_\beta(z_s) - r_\alpha(z_s)r_\beta'(z_e)\right]\right]$$
$$+ \frac{r_f^3 r_\alpha'(z_e)}{2\Phi_f^{\frac{1}{2}}}\int_{z_s}^{z_e}\left\{-\Phi^{\frac{1}{2}}r_\beta'^4 - \frac{1}{2}\frac{\Phi''}{\Phi^{\frac{1}{2}}}r_\beta^2 r_\beta'^2 + \frac{1}{16}\left[\frac{\Phi^{(4)}}{\Phi^{\frac{1}{2}}} - \frac{\Phi''^2}{\Phi^{\frac{3}{2}}}\right]r_\beta^4\right\}d\zeta$$
$$- \frac{r_f^3 r_\beta'(z_e)}{2\Phi_f^{\frac{1}{2}}}\int_{z_s}^{z_e}\left\{-\Phi^{\frac{1}{2}}r_\beta'^3 r_\alpha' - \frac{1}{4}\frac{\Phi''}{\Phi^{\frac{1}{2}}}r_\beta' r_\beta^2 r_\alpha' - \frac{1}{4}\frac{\Phi''}{\Phi^{\frac{1}{2}}}r_\beta'^2 r_\beta r_\alpha + \frac{1}{16}\left[\frac{\Phi^{(4)}}{\Phi^{\frac{1}{2}}} - \frac{\Phi''^2}{\Phi^{\frac{3}{2}}}\right]r_\beta^3 r_\alpha\right\}d\zeta \tag{7.51}$$

$$\Delta r_c'(z_e) = \frac{1}{2}\Delta\Phi r_f\left[-\frac{r_\beta'(z_e)}{\Phi_e} + \frac{r_\beta'(z_s)}{(\Phi_f\Phi_o)^{\frac{1}{2}}}\left[r_\alpha'(z_e)r_\beta(z_s) - r_\alpha(z_s)r_\beta'(z_e)\right]\right]$$
$$+ \frac{\Delta\Phi r_f r_\alpha'(z_e)}{2\Phi_f^{\frac{1}{2}}}\int_{z_s}^{z_e}\left\{\frac{1}{\Phi^{\frac{1}{2}}}r_\beta'^2 + \frac{1}{4}\frac{\Phi''}{\Phi^{\frac{3}{2}}}r_\beta^2\right\}d\zeta$$
$$- \frac{\Delta\Phi r_f r_\beta'(z_e)}{2\Phi_f^{\frac{1}{2}}}\int_{z_s}^{z_e}\left\{\frac{1}{\Phi^{\frac{1}{2}}}r_\beta' r_\alpha' + \frac{1}{4}\frac{\Phi''}{\Phi^{\frac{3}{2}}}r_\beta r_\alpha\right\}d\zeta. \tag{7.52}$$

If also the conditions of zero slope at the start and exit plane are met, the expressions simplify to (with the substitution $r_f = r_s/r_\beta(z_s)$):

$$\Delta r_3'(z_e) = \frac{r_s^3 r_\alpha'(z_e)}{2\Phi_f^{\frac{1}{2}} r_\beta^3(z_s)} \int_{z_s}^{z_e} \left\{ -\Phi^{\frac{1}{2}} r_\beta'^4 - \frac{1}{2}\frac{\Phi''}{\Phi^{\frac{1}{2}}} r_\beta^2 r_\beta'^2 + \frac{1}{16}\left[\frac{\Phi^{(4)}}{\Phi^{\frac{1}{2}}} - \frac{\Phi''^2}{\Phi^{\frac{3}{2}}}\right] r_\beta^4 \right\} d\zeta \quad (7.53)$$

$$\Delta r_c'(z_e) = \frac{\Delta\Phi r_s r_\alpha'(z_e)}{2\Phi_f^{\frac{1}{2}} r_\beta(z_s)} \int_{z_s}^{z_e} \left\{ \frac{1}{\Phi^{\frac{1}{2}}} r_\beta'^2 + \frac{1}{4}\frac{\Phi''}{\Phi^{\frac{3}{2}}} r_\beta^2 \right\} d\zeta \quad (7.54)$$

7.5 Calculation example

As an example, the spherical and chromatic aberration for the corrector design in figure 7.1 will be calculated and compared to results from ray-tracing calculations. The design is symmetric around the foil and for simplicity, also the same potentials (mirror symmetric) are applied to the electrodes at both side of the foil. The foil is put at 0.1 V, the electrodes closest to the foil at 100.1 V and the outermost electrodes at 1500.1 V. When the potential on the electrodes in between is set to 937.1 V (see figure 7.3), the paraxial ray as shown in figure 7.1 is obtained, which is parallel at the foil and at the start and exit plane. The axial potential and its 2^{nd} and 4^{th} derivative with respect to z (figure 7.4) are calculated with the finite element program Elens [34].

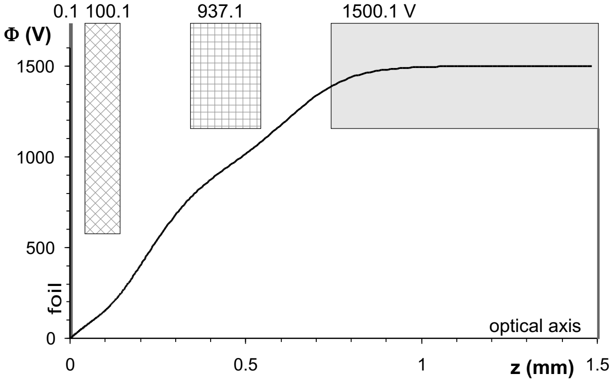

Figure 7.3: *Corrector set-up of figure 7.1 with the axial potential as calculated by the finite element program Elens (the set-up is symmetric around the optical axis and mirror symmetric in the foil). The numbers above the electrodes denote the voltages applied to them.*

The slope aberrations $\Delta r_3'$ and $\Delta r_c'$ are calculated with formulas 7.53 and 7.54. In figure 7.5 the values of their integrands are plotted. For this calculation, an energy spread of $\Delta\Phi = 0.2$ eV was taken and a radius of incidence at the start plane of $r_s = 0.015$ mm. The graphs show that the part closest to the foil contributes to a negative

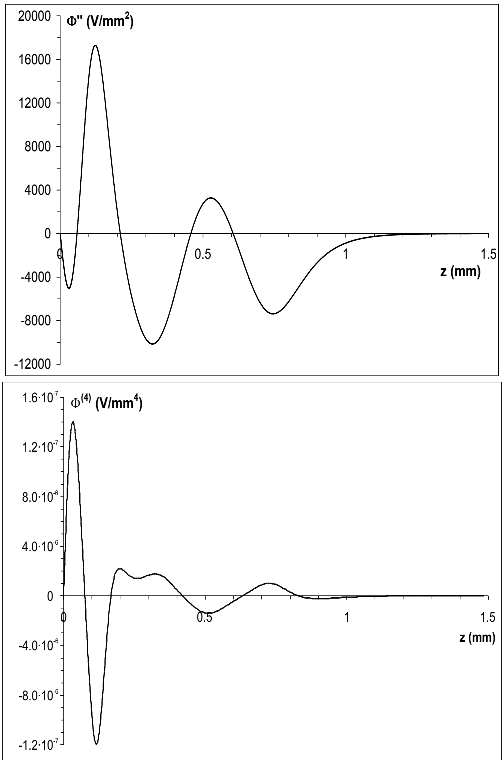

Figure 7.4: *2^{nd} and 4^{th} derivative of the axial potential with respect to z as calculated by Elens for the corrector configuration in figure 7.3.*

spherical and chromatic aberration (note that C_s and $\Delta r_3'$ have opposite sign). For the spherical aberration, this is due to the positive $\Phi^{(4)}$ and for the chromatic aberration due the negative Φ'' close to the foil. In order to avoid that this negative part is cancelled by the positive part following it, the potential must be the lowest at the foil and the radius of the trajectory must not be too small at the foil.

The results of the calculation are listed in table 7.1. With formulas 7.42 and 7.43 the coefficients of spherical and chromatic aberration in a specified probe are calculated. For this example, a 1 kV probe was taken with a half opening angle of α_p = 21 mrad (which is the diffraction limited opening angle at a 1 nm spot size).

For comparison, the slope aberrations are calculated from ray tracing as well. A large number of trajectories starting at different radii of incidence and with different energies have been calculated with Trasys [35]. Trasys uses a high accuracy interpolation in z and r to determine the potential in between the Elens mesh points, as described by Chmelik and Barth [9]. Thus, it can accurately trace the trajectories. The results are listed in table 7.1 as well. The differences with the results from the aberration integrals are less than 10%, which is quite acceptable.

The example is not intended as an optimised final corrector design, but it does

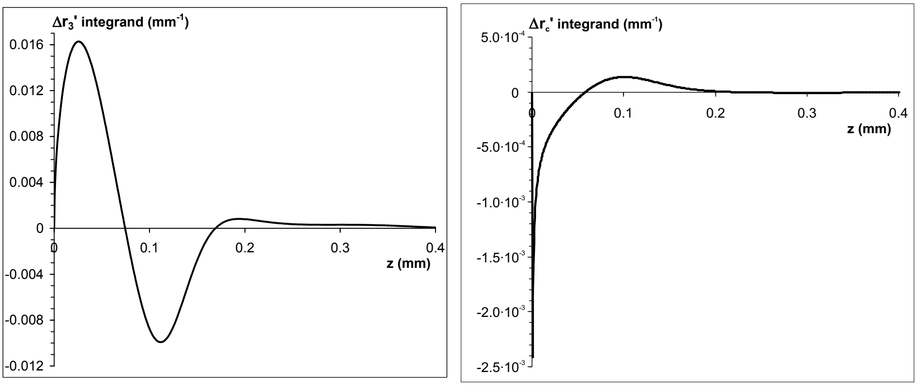

Figure 7.5: $\Delta r_3'$ *and* $\Delta r_c'$ *integrands as function of z for the corrector configuration in figure 7.3, with* r_s *= 0.015 mm and* $\Delta\Phi$ *= 0.2 eV.*

Table 7.1: *Calculation results for the configuration in figure 7.3.*

Corrector settings	Probe settings
radius of incidence $r_s = 0.015$ mm energy spread $\Delta\Phi = 0.2$ eV	probe voltage $V_p = 1$ kV half opening angle $\alpha_p = 21$ mrad
Results obtained with aberration integrals	
$\Delta r_3' = 6.85 \cdot 10^{-4}$ $\Delta r_c' = -2.37 \cdot 10^{-5}$	$C_{s,p}$ = -64.6 mm $C_{c,p}$ = -4.9 mm
Results from ray tracing	
$\Delta r_3' = 6.50 \cdot 10^{-4}$ $\Delta r_c' = -2.57 \cdot 10^{-5}$	$C_{s,p}$ = -61.4 mm $C_{c,p}$ = -5.3 mm

show that the low-voltage foil corrector can have negative spherical and chromatic aberration and thus can correct for both aberrations simultaneously. Previous attempts to find such a corrector were unsuccessful, because the chromatic aberration correction was too weak [21, 59]. Due to the very low potential of the foil, the low-voltage foil corrector can have a much stronger chromatic aberration correction. For a specific system, the corrector settings that give the required correction still have to be found. As the corrector can have a large negative spherical aberration, the use of a spherical aberration lens with tuneable positive spherical aberration is an option as well.

7.6 Conclusion

Integrals have been obtained that describe correctly the spherical and chromatic aberration correction for the low-voltage foil corrector. The integrals for the spherical aberration contain the 4^{th} derivative of the axial potential. Nowadays, the axial potential can easily be calculated with sufficient accuracy, allowing the 4^{th} derivative and the aberration integrals to be calculated numerically.

For a characterization of the corrector independent of the probe forming system, the geometrical and chromatic slope aberrations are more suitable than the aberration coefficients. Therefore integrals for the slope aberrations as well as for the aberration coefficients have been derived.

The example calculation has shown that the results obtained with the aberration integrals are in agreement with results from ray tracing. The example has also demonstrated that the low-voltage foil corrector can correct for both the spherical and chromatic aberration simultaneously.

The calculation method proposed in this paper offers a fast, easy and reliable calculation of the optical properties for many different settings.

Chapter 8

Design of an aberration corrected low-voltage SEM

8.1 Introduction

In chapters 6 and 7 it has been demonstrated that the low-voltage foil corrector can be used to simultaneously correct the spherical and chromatic aberration of an electron microscope. In this chapter, a design for a low-voltage Scanning Electron Microscope with a low-voltage foil corrector will be given. The corrector can be used in other types of electron microscopes as well. A low-voltage SEM is taken as example because the low-voltage foil corrector has some specific advantages for this type of microscope: it is convenient that the corrector can operate at low voltage and correction of both the spherical and chromatic aberration is desired for a low voltage probe. At higher voltage, the chromatic aberration becomes less important because it scales with the relative energy spread.

8.2 Column Design

The microscope column consists of electrostatic lenses only. At low voltage, electrostatic lenses can easily be made sufficiently strong and it allows for the design of a very compact column. The central part is the foil with apertures on both sides. As explained in chapter 6, the distance between the foil and the apertures closest to it must be small compared to the diameter of these apertures, in order to obtain aberration correction.

For the electron source, a conventional 5 kV Schottky emitter is taken. The potential of the spot on the sample is 1 kV. The potential of the foil is typically 0.1 V. For the calculations it is convenient to let the 0 V potential correspond to 0 eV kinetic energy. When implementing this design, of course all potentials may be decreased or increased with an identical amount, such that for example the sample is at ground potential. On both sides of the foil, there are five electrodes (see figure 8.1). The outermost electrode at the left side is put at the potential of the source and

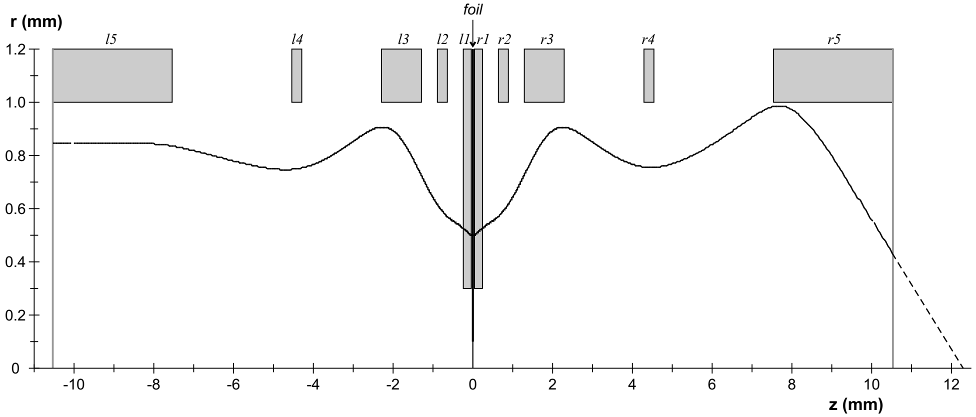

Figure 8.1: *Design of a low-voltage SEM column with a low-voltage foil corrector. The design is rotationally symmetric in the z-axis. Above the drawing, the numbering of de electrodes is designated. In the drawing, the paraxial ray for the settings in table 8.2 is shown. For the visibility, its radial extent is drawn 5 times larger than the maximum beam radius. Note that this ray has started in the object position which is far left from the left border, thus it enters the column with a very small, but non-zero slope.*

the outermost electrode at the right side at the potential of the image. The electrodes next to them are used to focus the beam at the desired object and image position. Hence the three electrodes at both sides nearest to the foil remain for setting the desired spherical and chromatic aberration correction. To avoid bending of the foil, the electrostatic fields at both sides of the foil must be equal. This is achieved by making the apertures next to it mirror symmetric in the foil and applying identical voltages to them. For simplicity, the geometry of the other four electrodes at both sides is mirror symmetric in the foil as well. This facilitates the calculations and there is no indication that a non symmetric geometry would be better. The mirror symmetry is also effectuated in the potentials applied to the three electrodes closest to the foil, in order to apply approximately the same amount of aberration correction left and right from the foil.

The systems first order optics must satisfy a number of conditions, that have to be evaluated first.

(a) The electron beam must be incident perpendicular to the foil. In other words the trajectory must have zero slope at the foil. This is used as the first boundary condition when calculating the paraxial trajectory. Hence the object and image position may change when the settings are altered.

(b) The virtual probe size of a Schottky emitter is approximately 30 nm. In order to obtain a spot size of the order of 1 nm, a demagnification is required. As a consequence, the image distance has to be much shorter than the object distance.

(c) In order to have a reasonable amount of current in a small probe, the half open-

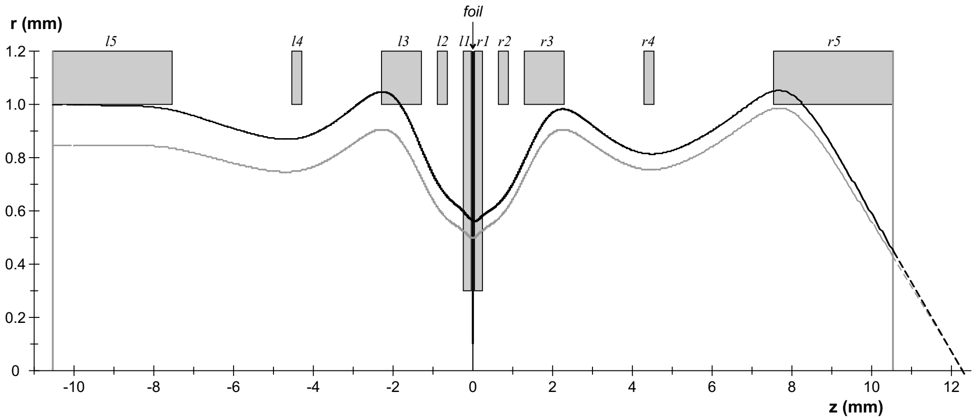

Figure 8.2: *Paraxial ray starting in the object plane with zero slope and unity height, for the settings in table 8.2. Plotted In grey: the paraxial ray starting from the object position, as shown in figure 8.1.*

Table 8.1: *Measures of the column design in figure 8.1. The design is mirror symmetric in the foil, only the measures for the electrodes at the right side are listed.*

electrode no.	thickness (mm)	aperture radius (mm)	distance to next electrode (mm)
foil	0	-	0.04
$r1$	0.20	0.30	0.40
$r2$	0.25	1.00	0.40
$r3$	1.00	1.00	2.00
$r4$	0.25	1.00	3.00
$r5$	3.00	1.00	-

ing angle at the probe must be as large as possible. This follows simply from the conservation of reduced brightness.

In uncorrected systems, the opening angle can not be made too large, in order to avoid an increase of the spot size due to the 3^{rd} order spherical aberration. In this system, the opening angle may be increased till the 5^{th} order spherical aberration becomes significant. In order to obtain a large opening angle at the probe, the image distance - and thus the working distance - is kept as short as possible. When the working distance is increased and the opening angle kept constant, the width of the beam in the corrector increases proportionally. The limitation here is the lateral size of the free-standing foil. In the drawing in figure 8.1 it can be seen that the free-standing foil extends over the whole diameter of the column. It only has to be as thin as a few nm over a diameter that encompasses the beam diameter. Outside, the foil can be made thicker, as long as the thicker shape has negligible effect on the electric field.

The considerations above have led to the design in figure 8.1. The distance between the electrodes is chosen such that voltage differences of a few kV can be applied, taking into account that for avoiding flashovers, the maximum tolerable field is 10 kV/mm. The distance between the foil and its neighbouring electrodes is 0.04 mm, so a maximum voltage of 400 V can be applied to these electrodes.

8.3 Calculation procedure

The axial potential and its derivatives with respect to z up to the 4^{th} derivative are calculated with the finite element program Elens [34]. The axial potential and its derivatives are calculated for every electrode separately, by putting the respective electrode at unit potential and all the others at zero potential. Afterwards, the axial potential and derivatives for the whole column are constructed by superposition of the contributions of all electrodes, multiplied by a factor representing the voltage on the respective electrode. This procedure allows the potentials on the electrodes to be changed easily, without having to do a complete calculation again. For the calculation with Elens, it is required that the left and right border of the structure are shut off with an electrode. Therefore sheet electrodes are put at these borders, which are on the same potential as electrodes $l5$ and $r5$. The measures of electrodes $l5$ and $r5$ are such that the left and right border are almost field free, such that these artificial sheet electrodes will not affect the calculation results. The object and image plane may very well be outside the simulated structure, this can easily be accounted for in the calculation as explained in section 7.3.

Two methods have been used to calculate the aberration coefficients. First the coefficients of 3^{rd} order spherical and 1^{st} order chromatic aberration are calculated using the aberration integrals that have been derived in chapter 7 (respectively formulas 7.34 and 7.35). This is a very fast calculation method. When the potential on one of the electrodes is changed, the effect on the aberrations can be seen immediately. Hence this method is very suitable to study the effect on the aberrations of a change in potential of every electrode and to find a setting that gives net zero aberration.

After a setting has been found that gives the desired aberration correction, a ray tracing calculation is performed with Trasys [35]. Trasys uses a high accuracy interpolation in z and r to determine the potential in between the Elens mesh points, as described by Chmelik and Barth [9]. The ray tracing calculation serves as a verification of the results obtained with the aberration integrals and it also allows to obtain an estimate of the 5^{th} order spherical and the 2^{nd} order chromatic aberration.

When a real microscope column is fabricated according to the design that will be proposed in this chapter, its properties may still differ somewhat from the calculated properties because there will always be small differences between the design and the result of a fabrication process. Therefore it is desired to know how the potentials on the electrodes must be changed to increase or decrease a specific aberration correction, while maintaining the same focus and magnification. For the three electrodes closest to the foil, a general characterisation of the systems response to a change of one of these potentials can not be given, because it depends on the specific system settings. Therefore after a suitable setting has been found, the effect of changing the electrode

Table 8.2: *Electrode potentials and calculation results for an optimum setting based on aberration integral calculations.*

electrode no.	potential (V)
$l5$	5000.1
$l4$	8900.1
$l3$	770.1
$l2$	2950.1
$l1$	340.1
foil	0.1
$r1$	340.1
$r2$	2950.1
$r3$	770.1
$r4$	9000.1
$r5$	1000.1

optical property	aberration integrals	ray tracing
Z_o	-394 mm	-515 mm
Z_i	12.3 mm	12.3 mm
a_1	-0.275 mm^{-1}	-0.272 mm^{-1}
M	-0.0204	-0.0155
C_{s3}	-0.68 mm	18 mm
C_{c1}	-0.002 mm	-0.83 mm
C_{s5}		3.2·10^3 mm
C_{c2}		5.3·10^2 mm

Table 8.3: *Optical properties calculated with aberration integrals for a foil potential of respectively 0.1, 0.4 and 1.0 V. The potentials of the other electrodes with respect to the foil are the same as in table 8.2.*

optical property	$V_{\text{foil}} = 0.1$ V	$V_{\text{foil}} = 0.2$ V	$V_{\text{foil}} = 0.4$ V
Z_o	-393.7 mm	-392.6 mm	-390.4 mm
Z_i	12.32 mm	12.32 mm	12.32 mm
a_1	-0.275 mm^{-1}	-0.275 mm^{-1}	-0.275 mm^{-1}
M	-0.0204	-0.0204	-0.0205
C_{s3}	-0.682 mm	-0.683 mm	-0.687 mm
C_{c1}	-0.002 mm	0.056 mm	0.164 mm

potentials is studied for this specific setting, using the aberration integrals. From this information, a characterisation of the systems response for this setting can be obtained.

8.4 Calculation results

Using the aberration integrals, an optimised setting has been found that has overall almost zero chromatic aberration and a small negative third order spherical aberration. In table 8.2 the potentials on the electrodes are listed for this setting and the resulting optical properties. The purpose of the small negative 3^{rd} order spherical aberration is to partly compensate the positive 5^{th} order spherical aberration. This will be explained in section 8.5. In the drawing of the column design in figure 8.1, the corresponding paraxial ray is inserted. For this calculation, the boundary conditions for the two independent paraxial rays r_α and r_β as given in equation 7.17 have been used. r_α starts in the object plane from the axis with unity slope. Only this paraxial ray is required for the aberration integral calculation, as is explained in section 7.2.2.

The paraxial ray shown in figure 8.1 is equal to r_α except for a constant factor. r_β starts in the object plane with zero slope and unity height. This ray is shown in figure 8.2. Figure 8.3 shows the C_s and C_c integrand as function of z. The graphs show that a big aberration correction occurs near the foil, which is partly cancelled in the region of electrodes $l3$, $l2$ and $r2$, $r3$ where the beam is deflected towards the optical axis. An indication of the amount of aberration correction by the corrector in this set-up can easily be obtained as follows. The aberration correction must, in approximation, equal the aberrations of the objective lens. It can be seen that in this set-up, the objective lens is effectively in the region of $z > 6$ mm. The aberration coefficients of this objective lens are obtained by simply taking the aberration integrals from $z = 6$ mm to $z = z_i$. This results in $C_s = 24.7$ mm and $C_c = 4.3$ mm. The results in table 8.2 apply for a beam that has an energy of 0.1 eV at the foil. Since the beam will have an energy spread of a few tenths eV, in table 8.3 also the results are listed for energies at the foil of 0.2 and 0.4 eV. This has been calculated by increasing the potentials on all electrodes with respectively 0.1 and 0.3 eV with respect to the settings in table 8.2. The effect on the results is small.

In table 8.2 the resulting optical properties from a ray tracing calculation are listed as well. These results show a small negative chromatic aberration, a considerable positive spherical aberration and somewhat weaker 1^{st} order properties. The difference between the two calculation methods is much larger than for the calculation example in section 7.5. This is probably due to the fact that this calculation had to be done with a lower spatial resolution. Both calculations were performed with the maximum of 200,000 mesh points allowed by the version of Elens that was available at the moment. The geometry presented here is a few times larger than that of the calculation example in section 7.5, hence a much lower mesh density had to be used. It is not a critical problem, because it can be shown that the corrector can be tuned to positive as well as negative spherical and chromatic aberration, thus a setting with net zero aberration must exist. Due to the lower calculation accuracy, it just requires some more effort to find this specific setting. By making use of the system characterisation that will be given below and doing a series of ray tracing calculations in an iterative approach, the settings have been found for which the ray tracing calculation results show the required aberration correction. These results are listed in table 8.4.

For the settings in tables 8.2 and 8.4 the position of the image is respectively $Z_i = 12.3$ mm and $Z_i = 12.2$ mm. Electrode $r5$ starts at position $z = 7.54$ mm. Thus a working distance of approximately 4.5 mm can be created. When the image is kept fixed at this position, there is a constant relation between the radius of the beam at the foil (r_{foil}) and the half opening angle α at the image:

$$\alpha = r_{\text{foil}} \cdot 450 \text{ mrad/mm} \tag{8.1}$$

with α in mrad and r_{foil} in mm.

The system is designed to have net zero aberrations, but when a ray is interrupted somewhere halfway, it may still be aberrated. Thus a ray that has travelled from the source to the foil may not be incident exactly perpendicular to the foil. For very low energies, this may result in reflection of the ray at the foil. Whether this has a significant effect on the transmission can best be checked with a ray tracing calculation. For the settings in table 8.4 rays with various energies have been traced.

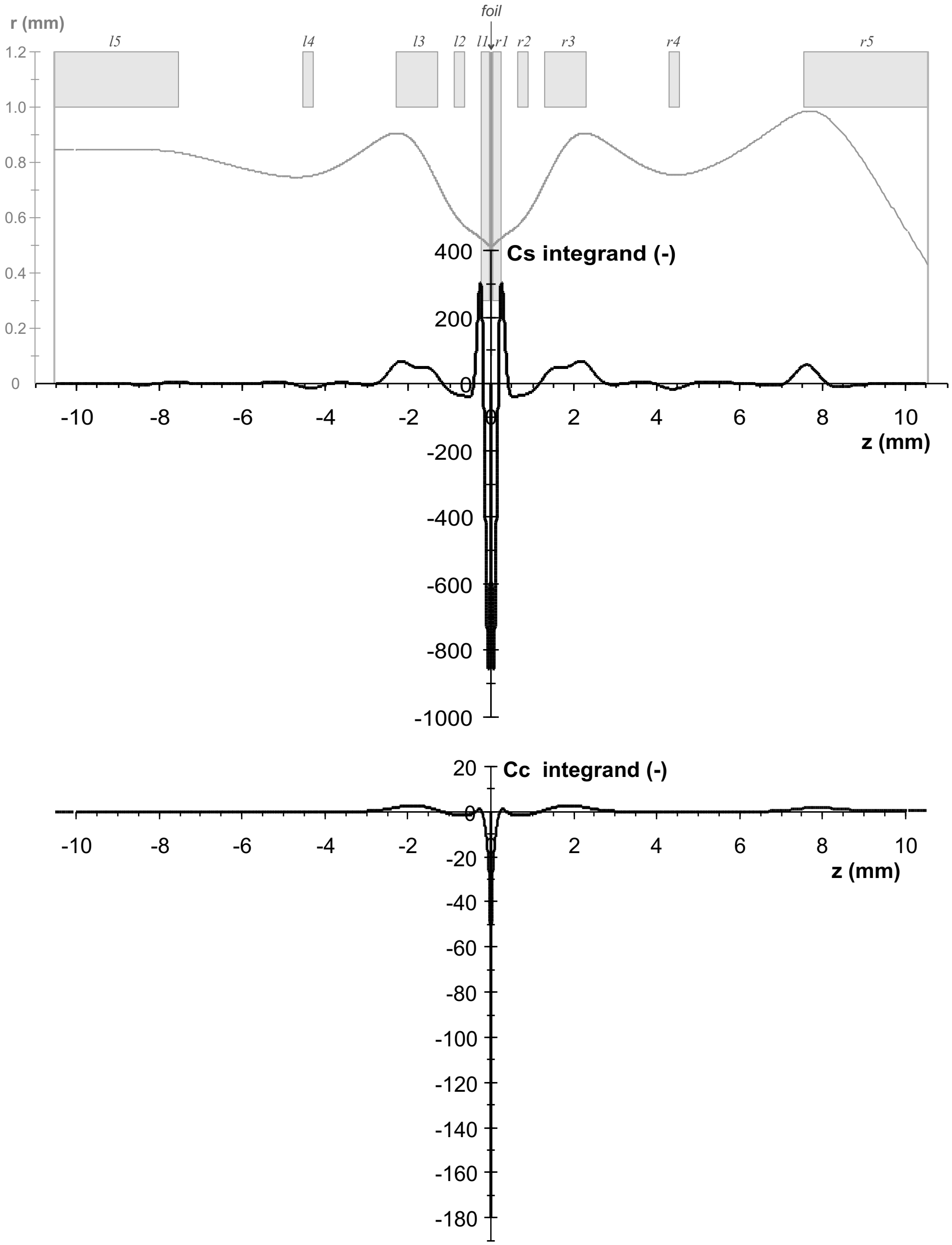

Figure 8.3: *Top: C_s integrand (see formula 7.34) as function of z. Shown in grey: the column design and the paraxial ray starting from the object position. Bottom: C_c integrand (see formula 7.35) as function of z. The potentials on the electrodes are given in table 8.2.*

Table 8.4: *Electrode potentials and calculation results for an optimum setting based on ray tracing calculations.*

electrode no.	potential (V)
*l*5	5000.1
*l*4	8720.1
*l*3	785.1
*l*2	3280.1
*l*1	330.1
foil	0.1
*r*1	330.1
*r*2	3280.1
*r*3	785.1
*r*4	9000.1
*r*5	1000.1

optical property	aberration integrals	ray tracing
Z_o	-257 mm	-310 mm
Z_i	12.2 mm	12.2 mm
a_1	-0.274 mm^{-1}	-0.271 mm^{-1}
M	-0.0311	-0.0257
C_{s3}	-27 mm	-0.34 mm
C_{c1}	-0.29 mm	-0.07 mm
C_{s5}		$2.1 \cdot 10^3$ mm
C_{c2}		$2.0 \cdot 10^2$ mm

The effect will be the worst for the rays that start under the largest angle. For this calculation, the half opening angle of the rays at the source was 0.25 mrad, which corresponds to a beam radius of 0.05 mm and a half opening angle at the image of 21.6 mrad. The slowest particle in this calculation had a kinetic energy at the foil of only 0.016 eV, this ray still passed the foil. Hence it can be concluded that the effect on the transmission is negligible.

Another point of attention is the beams opening angle at the foil. Because the beam has a finite brightness, it must have some angular spread, otherwise it could not contain any current. Using the formula for the reduced brightness (equation 4.11) the opening angle at the foil can be determined. For a reduced brightness of $1 \cdot 10^8$ Asr^{-1}m^{-2}V^{-1}, a current of 300 pA, a beam radius of 0.05 mm and a voltage of 0.1 V, the half opening angle becomes $3.5 \cdot 10^{-5}$ rad. The angle at the foil caused by the aberrations as discussed above is orders of magnitude higher; for a ray having 0.1 eV kinetic energy at the foil it is of the order of 0.1 rad. Hence this small angle forms no point of concern.

For the settings in table 8.2 and 8.4, the systems response to changes of the electrode potentials has been determined. The results for each electrode are summarized below. In table 8.5, the quantitative changes resulting from an increase of the potentials on the respective electrodes with 1 V are listed, for the settings in table 8.2.

- ***l4* and *r4*** are used to set the object and image position respectively. Increasing the voltage leads to a smaller object or image distance. Changing the potential of *l*4 has negligible effect on the aberrations, which is due to the demagnification from source to image. Increasing the potential on *r*4 increases the chromatic aberration correction. For the setting in table 8.2 it increases the spherical aberration correction, for the setting in table 8.4 the effect has reversed and it slightly decreases the spherical aberration correction.
- ***l3* and *r3*** can be used to adjust the spherical aberration correction. Increasing *l*3 and *r*3 leads to an increase of the spherical aberration correction and a slight increase

Table 8.5: *Changes of the optical properties due to an increase of the voltage on the respective electrodes with 1 V (calculated using aberration integrals).*

electrode no.	potential (V)	change due to voltage increase of 1 V			
		ΔC_s (mm)	ΔC_c (mm)	ΔZ_o (mm)	ΔZ_i (mm)
$l4$	8900.1	$+3.5 \cdot 10^{-4}$	$+8.2 \cdot 10^{-5}$	+3.2	0
$r4$	9000.1	$-6.0 \cdot 10^{-3}$	$-4.9 \cdot 10^{-4}$	0	$-1.0 \cdot 10^{-3}$
$l3$ & $r3$	770.1	-0.15	$-1.8 \cdot 10^{-3}$	-18	$+3.1 \cdot 10^{-3}$
$l2$ & $r2$	2950.1	-0.039	$-1.3 \cdot 10^{-3}$	+1.5	$-2.8 \cdot 10^{-4}$
$l1$ & $r1$	340.1	+0.95	+0.022	-46	$+7.8 \cdot 10^{-3}$

of the chromatic aberration correction. The systems' first order focal strength slightly decreases when these potentials are increased.

- ***l2* and *r2*** affect both the spherical and chromatic aberration. Increasing $l2$ and $r2$ leads to an increase of the spherical and a decrease of the chromatic aberration correction. The systems' first order focal strength slightly increases when these potentials are increased.

- ***l1* and *r1*** also affect both the spherical and chromatic aberration. Increasing the potential on these electrodes leads to a decrease of both the spherical and the chromatic aberration correction. The effect on the spherical aberration is much stronger than for the chromatic aberration. It is also stronger than the effect of a proportional change of the potential of one of the other electrodes. The systems' first order focal strength decreases when these potentials are increased.

These results lead to the following practical guidelines for using the system. As observed above, changing the potential on $l1$ and $r1$ has a large impact on the optical properties. It is expected that only small adjustments will be required. Then it is best to put these electrodes on a fixed and stable potential and use the other electrodes for the small adjustments. To increase the spherical aberration correction, the voltage on electrodes $l3$ and $r3$ is increased. Additionally the voltage on electrodes $l2$ and $r2$ must be decreased to keep the chromatic aberration constant. Due to these actions, the object and image distance have increased (note that Z_o is always negative, hence the object distance increases when Z_o decreases). They are reset to their old values by increasing the voltages on $l4$ and $r4$. To increase the chromatic aberration correction, the voltage on electrodes $l2$ and $r2$ is increased and simultaneously the voltage on electrodes $l3$ and $r3$ is slightly decreased, such that the spherical aberration remains constant. Now the object and image distance have decreased, thus the voltages on $l4$ and $r4$ must be decreased. The last step in both procedures of resetting the object and image distance has a small effect on the spherical and chromatic aberration, so the procedure may have to be repeated a few times to iteratively obtain the desired result. In order to decrease the spherical or chromatic aberration correction, the same procedures can be followed with the opposite actions.

The demagnification from source to image is related to the ratio of the object to the image distance. The image is kept at a fixed position, to avoid that the sample has to be moved. In this calculation, it is assumed that the source is positioned at a fixed position Z_o. However with a simple alteration, some flexibility can be introduced here. Between the source and electrode $l5$ two lenses with a cross over in between can be placed. This has the advantage that the object distance can be changed without having to move the source and additionally the column length may be decreased. By decreasing or increasing the object distance, the magnification, and thus the geometrical spot size, may respectively be increased or decreased. Because this system is always demagnifying, the aberrations of the two additional lenses will only have a very small effect in the probe, which can easily be corrected. When different spot sizes are to be used, it is convenient to set the spherical and chromatic aberration correction to the values that are best for the smallest spotsize. When the system is switched to a larger spotsize, the correction will not be optimal anymore, but the effect is very small and less important for larger spotsizes. Thus the system can be set to different spotsizes without having to adjust the aberration correction.

The system responses to voltage changes listed in table 8.5 also give an indication of the stability requirements to the voltage supplies of the respective electrodes. An analysis of all effects has revealed that the most critical is the change of the image position due to instabilities in the potential on electrode $r4$. With a proper design, a relative stability of the voltage supplies of 10^{-6} can be obtained. For electrode $r4$, this causes a shift of the image position of 9 nm. Assuming a half opening angle of about 22 mrad, this results in an image blur of 0.2 nm.

8.5 5^{th} order spherical aberration

In uncorrected systems, the 5^{th} order spherical aberration usually does not have to be taken into consideration. Due to the 3^{rd} order spherical aberration, the opening angle may not become too large and hence the 5^{th} order contribution is still negligible. Once the 3^{rd} order spherical aberration has been corrected, the opening angle may be increased, allowing more current in the spot and decreasing the diffraction contribution to the spotsize. However, now the 5^{th} order spherical aberration sets the upper limit for the opening angle.

The effect of the positive 5^{th} order spherical aberration can be reduced by applying some over-correction of the 3^{rd} order. This is similar to the procedure used in systems with positive 3^{rd} order spherical aberration where some defocus is applied to reduce the spherical aberration spotsize. Just like a positive 3^{rd} order spherical aberration can be reduced with a negative 1^{st} order (the defocus), a positive 5^{th} order spherical aberration can be reduced with a negative 3^{rd} order. The required C_{s3} to get the best correction with a given C_{s5} and the resulting spherical aberration disc can be derived in approximation as follows. The intercept with the optical axis for a spherical aberrated ray as function of the angle of incidence is

$$z_i(\alpha_{\mathrm{ray}}) = z_0 - C_{s3}\alpha_{\mathrm{ray}}^2 - C_{s5}\alpha_{\mathrm{ray}}^4 \tag{8.2}$$

where z_0 is the intercept in the paraxial approximation, α_{ray} designates the angle of incidence of the specific ray (the symbol α is reserved to indicate the half opening angle). Near the field free image position, the height of the ray as function of its

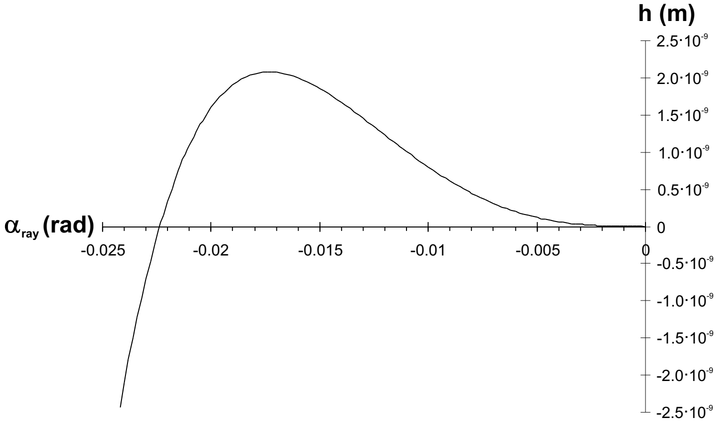

Figure 8.4: *Height of a spherical aberrated ray in the vicinity of the image plane, plotted as function of its angle of incidence for zero defocus, C_{s3} = -0.001 m and C_{s5} = 2 m.*

z-position and its angle of incidence is

$$h(z,\alpha_{\mathrm{ray}}) = \alpha_{\mathrm{ray}}(z - z_i(\alpha_{\mathrm{ray}})) = (z - z_0)\alpha_{\mathrm{ray}} + C_{s3}\alpha_{\mathrm{ray}}^3 + C_{s5}\alpha_{\mathrm{ray}}^5. \tag{8.3}$$

In figure 8.4 the height of the ray versus its angle of incidence is plotted for zero defocus ($z = z_o$), a positive C_{s5} and a negative C_{s3}.

Additionally to a negative third order spherical aberration, some defocus may even further reduce the spherical aberration disc size. However a defocus will also affect the other contributions to the probe size. For simplicity, the situation with zero defocus is evaluated here. The graph in figure 8.4 shows that the height reaches a maximum at a certain α_{ray}. This point will be denoted by (α_1,h_{max}). The value of α_1 is found from:

$$\frac{\partial h(z,\alpha_{\mathrm{ray}})}{\partial \alpha_{\mathrm{ray}}} = 0 \text{ and } \alpha_1 < 0 : \alpha_1 = -\sqrt{-\frac{3C_{s3}}{5C_{s5}}}. \tag{8.4}$$

Optimal use of the negative third order spherical aberration is made, if at the angle α that corresponds to the half opening angle, the height is $-h_{max}$. This can be formulated as:

$$C_{s3}\alpha^3 + C_{s5}\alpha^5 = C_{s3}\alpha_1^3 + C_{s5}\alpha_1^5. \tag{8.5}$$

This results in the following relationship between C_{s3}, C_{s5} and α

$$C_{s3} = -1.15\ C_{s5}\ \alpha^2. \tag{8.6}$$

The value of C_{s5} can be obtained in approximation from ray-tracing calculations. The best setting for the third order spherical aberration correction depends on the desired opening angle. When the system is set to the optimal C_{s3}, the spherical aberration disc size containing all the current is found by substituting equation 8.6 in equation 8.3:

$$d_s = 0.30\ C_{s5}\ \alpha^5. \tag{8.7}$$

8.6 Probe size

When the system is corrected for third order spherical and first order chromatic aberration, the remaining contributions to the probe size are the "current-brightness" disc, the diffraction disc, the fifth order spherical aberration disc and the second order chromatic aberration disc. The current-brightness disc results from the fact that a probe with a finite brightness must have a non-zero size in order to contain a non-zero current. These four contributions and the resulting total probe size will be determined following the method outlined by Barth [5]. The Full Width 50 (FW50) disc sizes will be used, that is the disc size that contains 50% of the current.

The FW50 current-brightness disc size is equal to:

$$d_{I50} = \frac{2}{\pi\alpha}\sqrt{\frac{I}{B_r V}}, \tag{8.8}$$

where B_r is the reduced Brightness defined in terms of the diameter containing half of the current I for a uniform angular distribution. For an apertured system in which only a small fraction of the current emitted by the source is passed into the probe forming system, it may be assumed that the angular distribution is uniform.

According to Barth [5] the FW50 diffraction disc is:

$$d_{D50} = 0.54\ \frac{\lambda}{\alpha}, \tag{8.9}$$

where λ is the electron wavelength:

$$\lambda = \frac{1.226}{\sqrt{E_k}} \text{ with } E_k \text{ in eV and } \lambda \text{ in nm.} \tag{8.10}$$

Formula 8.7 gives the fifth order spherical aberration disc containing 100% of the current. The calculation of the FW50 disc is straightforward. For a uniform angular distribution of the current, the angle containing 50% of the current is $\sqrt{2}$ times smaller than the half opening angle:

$$\alpha_{FW50} = \frac{1}{2}\sqrt{2}\ \alpha. \tag{8.11}$$

the fifth order spherical aberration disc is proportional to the fifth power of α, hence the fifth order spherical aberration disc containing 50% of the current is

$$d_{s50} = 0.053\ C_{s5}\ \alpha^5. \tag{8.12}$$

The second order chromatic aberration disc containing 100% of the current is:

$$d_c = 2\ C_{c2}\ \left(\frac{1}{2}\epsilon_{100}\right)^2\ \alpha \tag{8.13}$$

where ϵ_{100} is the FW100 energy spread divided by the central beam energy. The factor 1/2 in the term with ϵ_{100} arises from the fact that a positive and a negative deviation from the central beam energy both result in the same spatial deviation, hence they overlap. In order to determine the FW50 spot, both the effects of the angular and the energy distribution should be taken into account. For this system, it will be shown (see figure 8.5) that the second order chromatic aberration only has a very small effect on the total probe size, thus a very accurate calculation is not required. By just substituting the FW100 value for the energy spread by the FW50 value, a reasonable upper limit approximation is obtained:

$$d_{c50} \approx \frac{1}{2}\; C_{c2}\; \epsilon_{50}^2\; \alpha \tag{8.14}$$

where ϵ_{50} is the FW50 energy spread divided by the central beam energy. Note that it is common to use the FW100 value for the half opening angle in equations, because this value can easily be determined when the beam limiting aperture is known. However for the energy spread, use of the FW100 value is not practical because the energy distribution may have very elongated tails containing very little current. It is better to use the FW50 value. Alternatively also the full width half maximum is used quite frequently, but as is explained by Barth and Nijkerk [6], this may be a misleading measure and it is even not well defined in the case of aberrations.

Barth [5] has presented a suitable method to add these different contributions. This method consists of a root power sum that can be formulated as follows:

$$d_{FW50} = \left\{ \left[\left(d_{s50}^4 + d_{D50}^4 \right)^{\frac{1}{4}\cdot 1.3} + d_{I50}^{1.3} \right]^{\frac{1}{1.3}\cdot 2} + d_{c50}^2 \right\}^{1/2} \tag{8.15}$$

where d_{FW50} is the total probe size containing 50% of the current. In figure 8.5 the different contributions and the total probe size are plotted as function of the half opening angle. For C_{s5} and C_{c2} the values obtained from the ray tracing calculation are used: $C_{s5} = 2$ m and $C_{c2} = 0.2$ m. A FW50 energy spread of 0.4 eV is assumed. This is lower than the typical energy spread of a Schottky emitter of 0.6 eV, but should easily be obtained with the energy filtering effect of the foil. The typical reduced brightness of a Schottky emitter has been taken: $B_r = 1 \cdot 10^8$ Asr^{-1}m^{-2}V^{-1} and the current was set to 100 pA. It can be seen that the minimum probe size is 1.6 nm at a half opening angle of 23 mrad. For these settings, the minimum probe size is dominated by the fifth order spherical aberration, diffraction and the current-brightness contribution.

The smallest possible probe size is obtained at low current, as the current-brightness contribution vanishes (the other contributions are unaffected by the current). In the limit of zero current, the minimum probe size is 1.0 nm, at a half opening angle of 22 mrad. At low currents, the probe size depends only on the diffraction and the 5^{th} order spherical aberration contribution (assuming that the chromatic aberration is negligible):

$$d_{FW50} \approx \left[d_{s50}^4 + d_{D50}^4 \right]^{1/4} = \left[(0.053\; C_{s5})^4\; \alpha^{20} + (0.54\; \lambda)^4\; \alpha^{-4} \right]^{1/4}. \tag{8.16}$$

Now a simple analytical relation between the minimum probe size and the electron wavelength can be obtained. The probe size reaches its minimum when:

$$\frac{\partial d_{FW50}}{\partial \alpha} = 0. \tag{8.17}$$

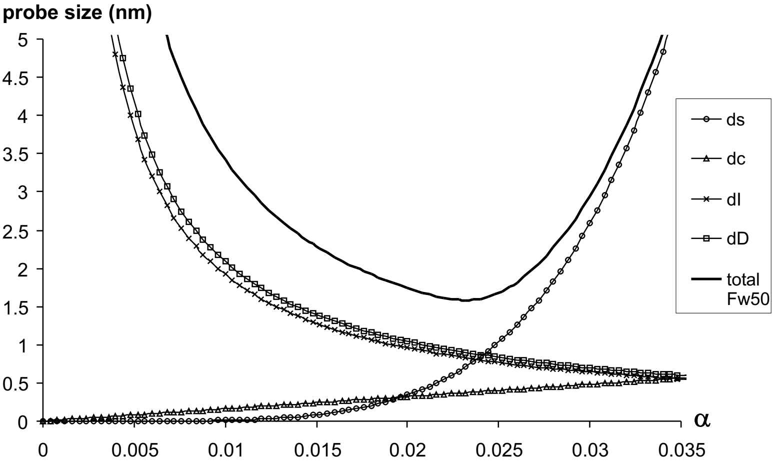

Figure 8.5: *Contributions to the FW50 probe size. ds: 5^{th} order spherical aberration disc for C_{s5} = -2 m; dc: 2^{nd} order chromatic aberration disc for C_{c2} = 0.2 m and $\epsilon_{50} = 4 \cdot 10^{-4}$; dI: current-brightness disc for $B_r = 1 \cdot 10^8$ $Asr^{-1}m^{-2}V^{-1}$ and I = 100 pA; dD: diffraction disc for λ = 0.039 nm. The thick line is the total FW50 spotsize as calculated with the root power sum algorithm according to Barth [5].*

This requirement returns the optimum α:

$$\alpha = 1.38 \left(\frac{\lambda}{C_{s5}}\right)^{\frac{1}{6}} . \tag{8.18}$$

Substitution of this α in equation 8.16 delivers the minimum probe size:

$$d_{FW50,min} \approx 0.41 \left(C_{s5}\lambda^5\right)^{\frac{1}{6}} . \tag{8.19}$$

For an energy of 1 keV, λ = 0.039 nm. With C_{s5} = 2 m, the resulting minimum probe size is 0.97 nm. The small difference with the value of 1.0 nm mentioned above is due to the contribution of the second order chromatic aberration.

It must be noted that in the calculations above, the loss of current in the foil has not yet been taken into account. This loss will of course reduce the current in the probe proportionally. If a transmission through the foil of 10% is assumed, this system can form a probe of 1.6 nm at 1 kV, containing a current of 10 pA. In figure 8.6 the probesize is plotted versus the probe current divided by the transmission ratio, which is equal to the current incident on the foil. Note that this transmission ratio includes the loss due to the energy filtering. In these calculations, it is assumed that the energy filter has reduced the energy spread from 0.6 eV to 0.4 eV. Then a maximum transmission in the absence of scattering of about 0.7 may be expected.

The major uncertainty in the calculation of the probe size is that C_{s5} could not yet be calculated very accurately. The effect on the calculated probe size is however not

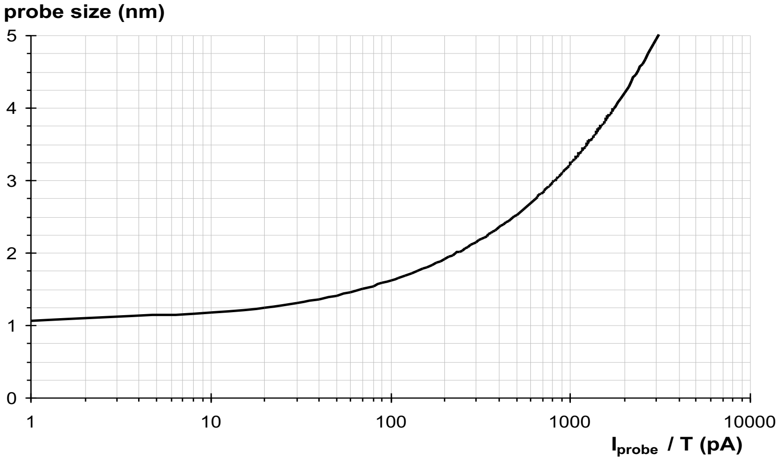

Figure 8.6: *Probesize versus the probe current divided by the transmission ratio of current through the foil. The latter is equal to the current incident on the foil. For every current, the half opening angle delivering the smallest probe size is used, the angles range from 22 to 26 mrad. The other parameters are identical to the ones in figure 8.5.*

very dramatic. For a value of C_{s5} two times larger, the minimum probe size increases from 1.6 nm to 1.8 nm, for a value two times lower it decreases to 1.4 nm.

A comparison of these results with existing systems is desired to determine whether it is useful to pursue the low-voltage foil corrector. A comparison between two systems can only be meaningful when they have identical acceleration voltage and working distance. A recent example of a comparable system is a multipole corrector built into a JEOL SEM for inspection of large scale integrated circuits that has been presented by Honda and Takashima [22]. This system has a working distance of 4 mm. At 1 kV acceleration voltage and 30 pA probe current, an experimentally determined resolution of 2.5 nm was obtained. Unfortunately, the FW50 probe size for this system is unknown. It is assumed that in a rough approximation, its value must be about the same as the resolution. With the system presented in this chapter a lower probe size can be obtained, however at a probe current that is not known exactly because it depends on the transmission through the foil. Alternatively, the probe size can be increased to approximately 2.5 nm by increasing the current-brightness contribution and then a statement can be done about the transmission that is required to obtain a probe current of 30 pA. For an incident current at the foil of 300 pA, the probe size becomes 2.2 nm. Hence a transmission through the foil of 10% is required to obtain a 30 pA probe current. Another recent example, for which the FW50 probe size is explicitly calculated, is a low-voltage SEM with an electrostatic multipole corrector by Maas, Mentink and Henstra [36]. The authors have calculated the aberrations and the probe size for a FEI XL30SFEG SEM equipped with an electrostatic multipole corrector invented by Henstra [20]. At a working distance of 5 mm and a beam energy of 1 keV, the best resolution in the zero current limit is obtained for a half opening angle of 21 mrad; the FW50 probe size is 1.14 nm. With the system presented in this chapter a similar probe size can be obtained in the zero current limit, however with a simpler type of corrector.

8.7 Conclusion

It has been demonstrated that with the low-voltage foil corrector a low-voltage Scanning Electron Microscope can be designed that is corrected for the spherical and chromatic aberration simultaneously. A system has been proposed with which a 1.6 nm probe at 1 kV can be formed. The current in this probe depends on the transmission of electrons through the foil. When a transmission of 10% is assumed, the probe current will be 10 pA. The probe size can be decreased to 1.0 nm, at the expense of current.

From comparison with an existing state-of-the-art system, it can be concluded that the low-voltage foil corrector becomes competitive when a transmission through the foil of 10% or better is obtained. Based on the calculations of the transmission in section 2.5 with experimentally obtained values for the mean free path, this is feasible (see figures 2.5 and 2.9). Hence further research on the low-voltage foil corrector is justified.

The system properties can be tuned by changing the potentials on the electrodes. For the aberration correction, only two or three different potentials are involved. Hence the system is relatively easy to control.

The accuracy of the calculations was limited by the maximum number of mesh points that could be handled by the finite element calculation software that was available at the moment. This does not affect the conclusion that the system presented here is suitable to correct the spherical and chromatic aberration simultaneously. However a better accuracy could help to find more easily the settings that give the optimal correction. The software that can handle a larger number of mesh points is expected to be available in the very near future.

References

[1] H. Adachi. Emission characteristics of metal-insulator-metal tunnel cathodes. *Journal of Vacuum Science and Technology B*, 14:2093, 1996.

[2] V.V. Aristov, V.V. Kazmiruk, V.A. Kudryashov, V.I. Levashov, S.I. Red'kin, C.W. Hagen, and P. Kruit. Microfabrication of ultrathin free-standing platinum foils. *Surface Science*, 402-404:337, 1998.

[3] G.P.E.M. van Bakel, E.G. Borgonjen, C.W. Hagen, and P. Kruit. Calculation of the electron-optical characteristics of electron beams transmitted into vacuum from a sharp tip-thin foil junction. *Journal of Applied Physics*, 83:4279, 1998.

[4] J.E. Barth. *Electrostatic Correction of the Spherical Aberration of Electron Lenses.* PhD thesis, The University of Arizona, 1967.

[5] J.E. Barth and P. Kruit. Addition of different contributions to the charged particle probe size. *Optik*, 101:101, 1996.

[6] J.E. Barth and M.D. Nykerk. Dependence of the chromatic aberration spot size on the form of the energy distribution of the charged particles. *Nuclear Instruments and Methods in Physics Research A*, 427:86, 1999.

[7] E. Bauer. The resolution of the low energy electron reflection microscope. *Ultramicroscopy*, 17:51, 1985.

[8] S. Belaidi, P. Girard, and G. Leveque. Electrostatic forces acting on the tip in atomic force microscopy: Modelization and comparison with analytic expressions. *Journal of Applied Physics*, 81:1023, 1997.

[9] J. Chmelik and J.E. Barth. An interpolation method for ray tracing in electrostatic fields calculated by the finite element method. *SPIE Charged-Particle Optics*, 2014:133, 1993.

[10] R. Danev and K. Nagayama. Transmission electron microscopy with zernike phase plate. *Ultramicroscopy*, 88:243, 2001.

[11] K. Danov, R. Danev, and K. Nagayama. Reconstruction of the electric charge density in thin films from the contrast transfer function measurements. *Ultramicroscopy*, 90:85, 2002.

[12] N. Dellby, O.L. Krivanek, P.D. Nellist, P.E. Batson, and A.R. Lupini. Progress in aberration-corrected scanning transmission electron microscopy. *J. Electron Microsc.*, 50:177, 2001.

[13] M.J. Fransen. *Towards high-brightness, monochromatic electron sources.* PhD thesis, Delft University of Technology, 1999.

[14] R. García, M. Calleja, and H. Rohrer. Patterning of silicon surfaces with noncontact atomic force microscopy: Field-induced formation of nanometer-size water bridges. *Journal of Applied Physics*, 86:1898, 1999.

[15] T. Hanai, H. Yoshida, and M. Hibino. Characteristics and effectiveness of a foil lens for correction of spherical aberration in scanning transmission electron microscopy. *J. Electron Microsc.*, 47:185, 1998.

[16] P.W. Hawkes and E. Kasper. *Principles of Electron Optics vol. 1.* Academic Press, London, UK, 1989.

[17] P.W. Hawkes and E. Kasper. *Principles of Electron Optics vol. 1, chapter 4.* Academic Press, London, UK, 1989.

[18] P.W. Hawkes and E. Kasper. *Principles of Electron Optics vol. 2.* Academic Press, London, UK, 1996.

[19] M. Heiblum. Tunneling hot electron transfer amplifiers (THETA): amplifiers operating up to the infrared. *Solid State Electronics*, 24:343, 1981.

[20] A. Henstra and M.P.C.M. Krijn. Electrostatic device for correcting chromatic aberration in a particle-optical apparatus. Patent Application, Int. Publication No. WO 99/27558, Int. Application No. PCT/IB98/01607, June 1999.

[21] H. Hoch, E. Kasper, and D. Kern. Der Öffnungsfehler 3. Ordnung und der axiale Farbfehler von rotationssymmetrischen Elektronenlinsen mit gekrümmter geladener transparanter Folie. *Optik*, 46:463, 1976.

[22] K. Honda and S. Takashima. Chromatic and Spherical Aberration correction in the LSI Inspection Scanning Electron Microscope. *JEOL News (www.jeoleuro.com/news/news38/jnews38l_pdf_low/p36.pdf)*, 38:36, 2003.

[23] Waterloo Maple Inc. *Maple V Release 5.1*, 1998.

[24] A. Jablonski and C.J. Powell. Relationships between electron inelastic mean free paths, effective attenuation lengths, and mean escape depths. *J. Electron Spectrosc. Relat. Phenom.*, 100:137, 1999.

[25] A. Jablonski and C.J. Powell. The electron attenuation length revisited. *Surface Science Reports*, 47:33, 2002.

[26] A. Jablonski and S. Tougaard. Comparison of the attenuation lengths and the inelastic mean free path for photoelectrons in silver. *Journal of Vacuum Science and Technology A*, 8:106, 1990.

[27] X. Jiang. Combined calculation of lens aberrations, space charge aberrations, and statistical Coulomb effects in charged particle optical columns. *Journal of Vacuum Science and Technology B*, 14:3747, 1996.

[28] X. Jiang. *Coulomb interactions in charged particle optical columns.* PhD thesis, Delft University of Technology, 1996.

[29] H. Kanter. Slow-Electron Mean Free Paths in Aluminum, Silver, and Gold. *Physical Review B*, 1:522, 1970.

[30] M. Knoll and E. Ruska. Das Elektronenmikroskop. *Zeitschrift für Physik*, 78:318, 1932.

[31] L.D. Landau and E.M. Lifshitz. *Theory of Elasticity (translated from Russian, 2nd edition).* Pergamon Press, Oxford, UK, 1970.

[32] S. Lazar, G.A. Botton, M.-Y. Wu, F.D. Tichelaar, and H.W. Zandbergen. Materials science applications of HREELS in near edge structure analysis and low-energy loss spectroscopy. *Ultramicroscopy*, 96:535, 2003.

[33] C. Lebreton and Z.Z. Wang. Nanofabrication on gold surface with scanning tunneling microscopy. *Microelectronic Engineering*, 30:391, 1996.

[34] B. Lencová and G. Wisselink. *Electron Optical Design Program Package Elens 3.7*, 2002.

[35] B. Lencová and G. Wisselink. *Electron Optical Design Program Package Trasys 3.7*, 2002.

[36] D. Maas, S. Mentink, and S. Henstra. Electrostatic Aberration Correction in Low-Voltage SEM. *Microscopy and Microanalysis*, 9:24, 2003.

[37] H.J. Mamin, H.P. Guethner, and D. Rugar. Atomic Emission from a Gold Scanning-Tunneling-Microscope tip. *Physical Review Letters*, 65:2418, 1990.

[38] S. Maruse, S.Hiratake, and M. Ichihashi. Korrektur vom Öffnungsfehler der Elektronenlinse. *Japan. J. Appl. Phys.*, 9:1549, 1970.

[39] G.K.L. Marx, P.O. Jubert, and R. Allenspach. Probing depth of threshold photoemissionelectron microscopy. *Applied Physics Letters*, 83:2925, 2003.

[40] C.A. Mead. Operation of Tunnel-Emission Devices. *Journal of Applied Physics*, 32:646, 1961.

[41] S.C. Meepagala and M.C. Baykul. Ballistic-electron emission into vacuum from a scanning-tunneling-microscope tip through free-standing gold films. *Physical Review B*, 50:13786, 1994.

[42] S.A.M. Mentink, T. Steffen, P.C. Tiemeijer, and M.P.C. Krijn. Simplified aberration corrector for low-voltage SEM. In C.J. Kiely, editor, *Electron Microscopy and Analysis 1999*, page 83. Institute of Physics Electron Microscopy and Analysis Group Conference, 1999.

[43] G. Mesa, J.J. Sáenz, and R. García. Current characteristics in near field emission scanning tunneling microscopes. *Journal of Vacuum Science and Technology B*, 14:2403, 1996.

[44] D.A. Muller, T. Sorsch, S. Moccio, F.H. Baumann, K. Evans-Lutterodt, and G. Timp. The electronic structure at the atomic scale of ultrathin gate oxides. *Nature*, 399:758, 1999.

[45] E. Munro and N.D. Wittels. Calculation of the optical properties of electron lenses with electron-transparent foils. *Optik*, 47:25, 1977.

[46] A. Di Paola, F. Di Quarto, and C. Sunseri. Anodic oxide films on tungsten-I. the influence of anodizing parameters on charging curves and film composition. *Corrosion Science*, 20:1067, 1980.

[47] C.J. Powell. The quest for universal curves to describe the surface sensitivity of electron spectroscopies. *J. Electron Spectrosc. Relat. Phenom.*, 47:197, 1988.

[48] F. Di Quarto, A. Di Paola, S. Piazza, and C. Sunseri. Influence of the thermal treatment on the photoelectrochemical behaviour of WO_3 photoanodes electrochemically grown. *Solar Energy Materials*, 11:419, 1985.

[49] J.J. Quinn. Range of Excited Electrons in Metals. *Physical Review*, 126:1453, 1962.

[50] G.J. de Raad, P.M. Koenraad, and J.H. Wolter. Use of the Schiller decapitation process for the manufacture of high quality tungsten scanning tunneling microscopy tips. *Journal of Vacuum Science and Technology B*, 17:1946, 1999.

[51] E. Ruska and M. Knoll. Die magnetische Sammelspule für schnelle Elektronenstrahlen. *Zeitschrift für techn. Physik*, 12:389–400 and 448, 1931.

[52] O. Scherzer. Über einige Fehler von Elektronenlinsen. *Zeitschrift für Physik*, 101:593, 1936.

[53] O. Scherzer. Sphärische und chromatische Korrektur von Elektronen-Linsen. *Optik*, 2:114, 1947.

[54] C. Schiller, A.A. Koomans, T.L. van Rooy, C. Schönenberger, and H.B. Elswijk. Decapitation of tungsten field emitter tips during sputter sharpening. *Surface Science Letters*, 339:L925, 1995.

[55] M.P. Seah and W.A. Dench. Quantitative Electron Spectroscopy of Surfaces: A Standard Data Base for Electron Inelastic Mean Free Paths in Solids. *Surface and Interface Analysis*, 1:2, 1979.

[56] M. Suzuki, T. Kusunoki, H. Shinada, and T. Yaguchi. Reducing electron energy dispersion of nonformed metal-insulator-metal electron emitters using the near-threshold drive method. *Journal of Vacuum Science and Technology B*, 13:2201, 1995.

[57] T. Tomita, H. Utsunomiya, T. Sakura, Y. Kamakura, and K. Taniguchi. A New Soft Breakdown Model for Thin Thermal SiO_2 Films Under Constant Current Stress. *IEEE Transactions on Electron Devices*, 46:159, 1999.

[58] D. Typke. Der Öfnungsfehler von rotationssymmetrischen Elektronenlinsen mit Raumladung. *Optik*, 28:488, 1968.

[59] D. Typke. Sphärische und chromatische Korrektur von Elektronenlinsen mit Hilfe von Influenzladungen, I und II. *Optik*, 44:509, 1976.

[60] K. Urban, B. Kabius, M. Haider, and H. Rose. A way to higher resolution: spherical-aberration correction in a 200 kV transmission electron microscope. *J. Electron Microsc.*, 48:821, 1999.

[61] A.H.V. van Veen, C.W. Hagen, and P. Kruit. Reduced brightness of the ZrO/W Schottky electron emitter. *Journal of Vacuum Science and Technology B*, 19:2038, 2001.

[62] U. Weierstall and J.C.H. Spence. Atomic species identification in STM using an imaging atom-probe technique. *Surface Science*, 398:267, 1998.

[63] C. Weißbäcker and H. Rose. Electrostatic correction of the chromatic and of the spherical aberration of charged-particle lenses (part I). *J. Electron Microsc.*, 50:383, 2001.

[64] C. Weißbäcker and H. Rose. Electrostatic correction of the chromatic and of the spherical aberration of charged-particle lenses (part II). *J. Electron Microsc.*, 51:45, 2002.

[65] P.A. Wolff. Theory of Secondary Electron Cascade in Metals. *Physical Review*, 95:56, 1954.

[66] K. Yokoo, S. Sato, G. Koshita, I. Amano, J. Murota, and S. Ono. Energy distribution of tunneling emission from Si-gate metal-oxide-semiconductor cathode. *Journal of Vacuum Science and Technology B*, 12:801, 1994.

[67] J. Zach and M. Haider. Aberration correction in a low voltage SEM by a multipole corrector. *Nuclear Instruments and Methods in Physics Research A*, 363:316, 1995.

Summary and Conclusions

This thesis has discussed two electron microscopy applications that make use of ultrathin foils: the tunnel junction emitter and the low-energy foil corrector. Both applications have in common that the electron beam is sent through the thin foil at low energy. Part of the electrons will scatter in the foil, thus causing a reduction of the transmitted current. An important requirement for both applications is that still a substantial part of the electrons is transmitted without scattering. Traditionally, such experiments were carried out at high voltage because at lower voltage, the inelastic mean free path of the electrons decreases and thus the loss due to scattering increases. However at very low energy the inelastic mean free path increases for decreasing energy. For most metals the workfunction is about 4 - 5 eV, meaning that the lowest energy the electrons may have to pass the foil is about 4 - 5 eV above the Fermi level. The dominant scattering mechanism at this energy is electron - electron scattering. For decreasing energy, the possibilities of the incoming electron to interact with the conduction electrons decreases and hence the inelastic mean free path increases. Measurements for a number of metals indicate a mean free path of about 5 nm at an energy of about 5 eV above the Fermi level. Free-standing foils of only 5 nm thickness can be fabricated nowadays. A fabrication process for samples that contain such foils is reported in this thesis. These samples have a search pattern that enables finding the area with the thin foils in a Scanning Tunnelling Microscope.

For a low energy free electron beam passing a foil, quantum mechanical reflections must be taken into account. On entering the foil, the electrons kinetic energy is increased and thus the wavelength is decreased. At low energy this is a significant effect. Due to the wavelength mismatch between foil and vacuum, quantum mechanical reflection at the foils surfaces can occur. Calculations show that the transmission oscillates, as function of both the energy and the foil thickness. A calculation for a 5.15 nm foil with a mean free path of 5 nm shows that due to the combined effects of scattering and quantum mechanical reflections, a transmission of 10 % is expected. Though this may seem low, such a transmission is already sufficient to make the low-energy foil corrector an attractive alternative for existing correctors.

The above reported value of 5 nm for the inelastic mean free path for metals must be regarded as a rough guide. Because of the limited amount of data and the experimental techniques used, it is premature to draw definite conclusions from these measurements. Recent experimental work indicates an inelastic mean free path for silver of around 16 nm. With a 5 nm thick foil having this mean free path, the calculations show that a transmission of about 50% can be obtained. Even larger mean free paths may be found for materials that have a low density of conduction electrons because that will reduce the electron - electron interactions. In this respect, semiconductors could be an interesting alternative for future work. However the electronic structure of semiconductors is more complicated than that of metals and therefore a re-evaluation of the quantum mechanical reflections will be required for these materials. After electron - electron interaction, the next most important scattering mechanism is electron - phonon interaction, giving rise to a mean free path of 30 - 40 nm.

The tunnel junction emitter is a novel high-brightness monochromatic electron emitter that has an ultra-thin conducting foil in tunnelling distance from a sharp tip. A positive potential of typically a few volt is applied to the foil with respect to the tip. Electrons will tunnel from tip to foil and part of these electrons will travel through the foil without scattering. The unscattered electrons will be emitted into the vacuum, provided that their forward energy is sufficient to overcome the foils workfunction. As such, the emitter contains an intrinsic high pass energy filter. By lowering the voltage between tip and foil towards the emission threshold, a narrower energy spread at the expense of emission current can be obtained. Because the electrons originate from an atomic size tunnelling area, a high brightness can be obtained as well.

A pilot experiment, using a Scanning Tunnelling Microscope in ultra high vacuum to position a sharp tip in front of a free-standing foil, has verified the principle of operation of the emitter. The experiments also showed instabilities in the tunnelling contact when the voltage was raised to the threshold for emission. These instabilities are probably due to the fact that the thin free-standing foil is easily attracted towards the tip by the electrostatic force when the voltage between tip and foil is increased to 5 V. Alternatively, a simple method has been presented for the fabrication of tunnel junction emitters as a solid state device. In these devices, a thin oxide layer is used as the gap between tip and foil. This avoids the problem of foil bending and such devices are more convenient for practical use as well. Measurements of the emission current versus the voltage on these devices show the emission threshold behaviour that is typical for tunnel junction emitters. However, the lifetime of these devices was very limited which is probably due to a degradation of the oxide layer during operation. No efforts have yet been made to optimize the oxide layer. Because of the stability problems, the reduced brightness and energy spread could not yet be determined experimentally.

A conventional foil corrector is a spherical aberration corrector consisting of a thin foil sandwiched between two apertures. An attractive feature of this corrector is the simplicity of its design and operation. The electron beam is transmitted through the foil at high energy, to ensure a sufficient transmission of current. An undesired side effect of the high voltage operation is that mobile adsorbates on the foils surface are cracked by the electron beam and thus a carbon contamination layer is created. This problem is eliminated in the low-energy foil corrector; in this corrector the electrons are retarded to almost zero energy at the foil. Additionally, the low-energy foil corrector can correct both the spherical and the chromatic aberration simultaneously and serves as an energy filter as well.

The electron optical properties have been calculated with ray tracing and by using aberration integrals. The results from both methods are consistent. The integrals for the spherical and chromatic aberration have been newly obtained. With these integrals, not only the aberration coefficients, but also the slope aberrations can be calculated. The latter is desired for a characterization of the corrector independent of the probe forming system. For a correct description of the spherical aberration of the low-energy foil corrector, these integrals must contain the fourth derivative of the axial potential. A commonly applied simplification to obtain an expression without the fourth derivative is not allowed here.

A design for a low-voltage Scanning Electron Microscope with a low-energy foil corrector has been presented. The specific advantages of using the corrector for this type of microscope are its low voltage operation and that correction of the chromatic aberration becomes more important for decreasing probe voltage. With this aberration corrected microscope, a 1.6 nm probe at 1 kV can be formed. The current in this probe depends on the transmission of electrons through the foil. Based on the calculation mentioned above, a transmission of 10% should not be too difficult to obtain. At this transmission ratio, the probe current will be 10 pA. The probe size can be decreased to 1.0 nm, at the expense of current. From comparison with an existing state-of-the-art system, it can be concluded that the low-energy foil corrector becomes competitive for a transmission through the foil of 10% or better.

Samenvatting en Conclusies

Dit proefschrift heeft twee elektronen microscopie toepassingen besproken, die gebruik maken van ultra dunne folies: de tunnel junctie emitter en de lage-energie folie corrector. Beide toepassingen hebben gemeen dat de elektronen bundel op lage energie door het dunne folie gestuurd wordt. Een deel van de elektronen zal in het folie verstrooien, hetgeen een reductie van de doorgelaten stroom tot gevolg heeft. Een belangrijke vereiste voor beide applicaties is dat nog een substantieel deel van de elektronen doorgelaten wordt zonder verstrooiing. Traditioneel werden zulke experimenten op hoge spanning uitgevoerd omdat voor lagere spanning de inelastische gemiddelde vrije weglengte van de elektronen afneemt en dus het stroom verlies als gevolg van de verstrooiing toeneemt. Echter, op zeer lage energie neemt de inelastische gemiddelde vrije weglengte juist toe voor afnemende energie. Voor de meeste metalen is de werkfunctie ongeveer 4 - 5 eV, hetgeen betekent dat de laagste energie die de elektronen nog mogen hebben om het folie te kunnen passeren ongeveer 4 - 5 eV boven het Fermi niveau is. Het dominante verstrooi mechanisme bij deze energie is elektron - elektron verstrooiing. Voor afnemende energie nemen de mogelijkheden voor het inkomende elektron voor interactie met de geleidings elektronen af en dus neemt de inelastische gemiddelde vrije weglengte toe. Metingen voor een aantal metalen geven een gemiddelde vrije weglengte aan van ongeveer 5 nm bij een energie van ongeveer 5 eV boven het Fermi niveau. Vrijstaande folies van slechts 5 nm dik kunnen tegenwoordig gefabriceerd worden. Een fabricage proces voor preparaten die zulke dunne folies bevatten wordt in dit proefschrift beschreven. Deze preparaten hebben een zoek-patroon dat het mogelijk maakt om het deel van het preparaat dat de dunne folies bevat te kunnen vinden in een Scanning Tunnelling Microscoop.

Voor een lage energie bundel die een dun folie passeert moet met quantum mechanische reflecties rekening worden gehouden. Bij het binnengaan van het folie neemt de kinetische energie van de elektronen toe en dus neemt de golflengte af. Bij lage energie is dit een significant effect. Vanwege de discrepantie tussen de golflengte in het folie en in het vacuum kunnen quantum mechanische reflecties aan de folie oppervlakken plaatsvinden. Berekeningen laten zien dat de transmissie oscilleert, zowel als functie van de energie als de folie dikte. Een berekening voor een 5.15 nm foil met een gemiddelde vrije weglengte van 5 nm toont dat als gevolg van de gecombineerde effecten van verstrooiing en quantum mechanische reflecties, een transmissie van 10 % verwacht wordt. Weliswaar mag dit als laag overkomen, een dergelijke transmissie is al voldoende om van de lage-energie folie corrector een aantrekkelijk alternatief voor bestaande correctoren te maken.

De boven gerapporteerde waarde van 5 nm voor de inelastische gemiddelde vrije weglengte voor metalen moet als een ruwe indicatie beschouwd worden. Vanwege de beperkte hoeveelheid data en de experimentele technieken die gebruikt zijn is het prematuur om definitieve conclusies uit deze metingen te trekken. Recent experimenteel werk heeft een inelastische gemiddelde vrije weglengte voor zilver van ongeveer 16 nm laten zien. De berekeningen laten zien dat met een 5 nm dik folie met deze gemiddelde vrije weglengte een transmissie van ongeveer 50% behaald kan worden. Nog grotere gemiddelde vrije weglengtes zouden gevonden kunnen worden voor materialen die een lage dichtheid aan geleidings elektronen hebben, omdat dat de elektron - elektron interacties zal reduceren. In dit verband zouden halfgeleiders een interessant alternatief voor toekomstig werk kunnen zijn. Echter, de elektronische structuur van halfgeleiders is gecompliceerder dan die van metalen en daarom zal een herevaluatie van de quantum mechanische reflecties vereist zijn voor deze materialen. Na de elektron - elektron interactie is elektron - phonon interactie het belangrijkste verstrooi mechanisme, hetgeen aanleiding geeft tot een gemiddelde vrije weglengte van 30 - 40 nm.

De tunnel junctie emitter is een nieuwe hoge helderheid monochromatische elektronen emitter, die een ultra dun geleidend folie in tunnel-afstand van een scherpe tip heeft. Het folie wordt gezet op een positieve potentiaal met een typische waarde van een paar volt ten opzichte van de tip. Elektronen zullen tunnelen van tip naar folie en een deel van deze elektronen zal door het folie reizen zonder verstrooiing. De niet verstrooide elektronen zullen het vacuum in geëmiteerd worden, mits hun voorwaartse energie voldoende is om over de werkfunctie van het folie te komen. Dit betekent dat de emitter een intrinsiek hoog doorlaat energie filter heeft. Door de spanning tussen tip en folie te laten afnemen richting de drempelwaarde voor emissie kan een kleinere energie spreiding bereikt worden, ten koste van emissie stroom. Omdat de elektronen uit een tunnel-oppervlak van atomaire afmetingen komen, kan ook een hoge helderheid behaald worden.

Een proef experiment is uitgevoerd, waarbij een Scanning Tunnelling Microscoop in ultra hoog vacuum is gebruikt om de scherpe tip voor het dunne folie te positioneren. Middels dit experiment is de principe werking van de emitter geverifieerd. De experimenten lieten ook instabiliteiten in het tunnel-contact zien als de spanning verhoogd werd tot de drempelwaarde voor emissie. Deze instabiliteiten zijn waarschijnlijk het gevolg van het feit dat het dunne vrijstaande folie makkelijk naar de tip toe getrokken wordt door de electrostatische kracht als de spanning tussen tip en folie wordt verhoogd tot 5 V. Als alternatief is een simpele methode gepresenteerd voor de fabricage van tunnel junctie emitters als een vaste stof device. Hierin dient een dunne oxide laag als de tunnel-gap tussen tip en folie. Daarmee wordt het probleem van folie buiging vermeden en zulke devices zijn eveneens meer geschikt voor praktisch gebruik. Metingen aan deze devices van de emissie stroom tegen de spanning laten het drempelwaarde gedrag zien dat typerend is voor tunnel junctie emitters. Echter, de levensduur van deze devices was erg beperkt, hetgeen waarschijnlijk het gevolg is van een degradatie van de oxide laag tijdens gebruik. Er zijn nog geen inspanningen gedaan om de oxide laag te optimaliseren. Vanwege de stabiliteitsproblemen konden de gereduceerde helderheid en energie spreiding nog niet experimenteel bepaald worden.

Een conventionele folie corrector is een sferische aberratie corrector bestaande uit een dun folie geplaatst tussen twee diafragmas. Een aantrekkelijke eigenschap van deze corrector is de eenvoud in ontwerp en in werking. De elektronen bundel wordt op hoge spanning door het folie gestuurd, om voldoende transmissie van stroom te bewerkstelligen. Een ongewenst neveneffect van de hoge spanning is dat mobiele adsorbaten op het folie oppervlak gekraakt worden door de elektronen bundel en zodoende wordt een koolstof contaminatie laag gecreëerd. Dit probleem is geëlimineerd in de lage-energie folie corrector; in deze corrector worden de elektronen vertraagd tot bijna nul energie bij het folie. Bovendien kan de lage-energie folie corrector gelijktijdig zowel de sferische als de chromatische aberratie corrigeren en eveneens kan het dienen als energie filter.

De elektronen optische eigenschappen zijn uitgerekend met 'ray tracing' en middels gebruikmaking van aberratie integralen. De resultaten van beide methoden zijn onderling consistent. De integralen voor de sferische en chromatische aberratie zijn opnieuw afgeleid. Met deze integralen kunnen niet alleen de aberratie coefficienten maar ook de helling aberraties uitgerekend worden. Dat laatste is gewenst voor een karakterisering van de corrector onafhankelijk van het probe vormende systeem. Voor een juiste beschrijving van de sferische aberratie van de lage-energie folie corrector moeten deze integralen de vierde afgeleide van de axiale potentiaal bevatten. Een veel gebruikte simplificatie om een expressie zonder de vierde afgeleide te verkrijgen is hier niet toegestaan.

Een ontwerp voor een laagspanning Scanning Elektronen Microscoop met een lage-energie folie corrector is gepresenteerd. De specifieke voordelen van het gebruik van de corrector voor dit type microscoop zijn de werking op laagspanning en het feit dat correctie van de chromatische aberratie belangrijker wordt voor afnemende probe spanning. Met deze aberratie gecorrigeerde microscoop kan een 1.6 nm probe op 1 kV gevormd worden. De stroom in deze probe hangt af van de transmissie van elektronen door het folie. Gebaseerd op de boven vermelde berekening zou een transmissie van 10% niet al te moeilijk te bereiken moeten zijn. Bij deze transmissie ratio zal de stroom in de probe 10 pA zijn. De probe afmeting kan verkleind worden tot 1.0 nm ten koste van de stroom. Uit een vergelijking met een bestaand state-of-the-art systeem kan geconcludeerd worden dat de lage-energie folie corrector concurrerend wordt bij een transmissie door het folie van 10% of meer.

Dankwoord

Toen ik aan dit project begon zag ik het mogen doen van een promotie onderzoek als een voorrecht dat ik met beide handen heb aangegrepen. Nu terugkijkend denk ik daar nog precies zo over. Onderzoek doen is gewoon leuk en de kans krijgen om een gewaagd en diepgaand promotie onderzoek te doen is iets unieks. In de eerste plaats wil ik daarom mijn promotor Pieter Kruit en mijn mentor Kees Hagen bedanken dat ze me deze mogelijkheid geboden hebben. De uitkomst van dit project is lange tijd ongewis gebleven, maar al die tijd heb ik van jullie het vertrouwen in een goede afronding ervaren. Kees heeft me gedurende het hele project met raad en daad terzijde gestaan. Pieter heeft me geregeld nieuwe ideeën en gezichtspunten en een goede dosis enthousiasme verschaft.

In het begin van dit project heb ik veel gehad aan de hulp van Ivan Stepanov. Hij heeft speciaal voor dit project een submicronfabricage proces ontwikkeld om preparaten met dunne folies te maken. Tevens wil ik DIMES bedanken voor de faciliteiten en de expertise die ze hierbij beschikbaar hebben gesteld. Bij de experimenten die ik gedaan heb kwamen zaken kijken variërend van vacuum techniek tot data acquisitie. Voor het aanpakken van de diverse technische problemen heb ik dankbaar en veelvuldig gebruik gemaakt van de hulp van Jan, Erik, Jacques en Rajes. Zonder jullie hulp zouden de femto-ampere-stroompjes door het ultra hoog vacuum nooit in dit proefschrift terecht gekomen zijn. En voor de niet technische vragen en problemen van de meest uiteenlopende aard kon ik altijd een beroep doen op Elly.

Merlijn en Marco hebben hun afstudeerwerk op dit project uitgevoerd. Jullie hebben allebei laten zien praktisch ingesteld te zijn en van aanpakken te weten en jullie zullen in dit proefschrift stukken van je eigen werk herkennen. Ook Alexander en Simon hebben een deel van hun afstuderen op dit project uitgevoerd en daarbij een paar concrete problemen uitgezocht.

Vooral bij de ontwikkeling van de 'low-energy foil corrector' heb ik vele discussies met Jim gevoerd over optiek en aberraties. Handig was ook dat ik jou hier de laatste maanden in de weekenden nog geregeld tegenkwam en met je van gedachten kon wisselen. Voor het afleiden van de juiste aberratie integralen ben ik te rade gegaan bij Michal Lenc, zonder zijn hulp was dit voor ons een onmogelijke klus geweest. Van Bohumila Lencova heb ik nuttige adviezen gekregen over het doen van numerieke berekeningen, zodat ik vol vertrouwen over deze reken-resultaten kan zijn.

Collega's, zeker zo belangrijk als de inhoudelijke zaken waren de goede sfeer en de prettige samenwerking. Ik heb me de afgelopen jaren prima vermaakt, daarvoor allemaal: bedankt !

About the author

Rogier van Aken was born in Amsterdam on the 17^{th} of March 1971. From 1983 to 1989 he attended grammar school "Het Waterlant College" in Amsterdam. In 1989 he started the study of applied physics at the Delft University of Technology. He finished his study in 1996 with a graduation thesis on silicon crystal growth and Atomic Force Microscopy. In 1997 he started his PhD work at the Delft University of Technology in the Charged Particle Optics group of professor Kruit. Since June 2004, the author works for Thales Naval Netherlands on the development of radar systems.